View metadata, citation and similar papers at core.ac.uk

brought to you by CORE

provided by Columbia University Academic Commons

Kaon to Two Pions decays from Lattice QCD: $\Delta I = 1/2$ rule and CP violation

Qi Liu

Submitted in partial fulfillment of the

requirements for the degree

of Doctor of Philosophy

in the Graduate School of Arts and Sciences

COLUMBIA UNIVERSITY

2012

©2012

Qi Liu

All Rights Reserved

Abstract

Kaon to Two Pions decays from Lattice QCD: $\Delta I = 1/2$ rule and CP violation

Qi Liu

We report a direct lattice calculation of the K to $\pi\pi$ decay matrix elements for both the $\Delta I = 1/2$ and $3/2$ amplitudes A_0 and A_2 on a 2+1 flavor, domain wall fermion, $16^3 \times 32 \times 16$ lattice ensemble and a $24^3 \times 64 \times 16$ lattice ensemble. This is a complete calculation in which all contractions for the required ten, four-quark operators are evaluated, including the disconnected graphs in which no quark line connects the initial kaon and final two-pion states. These lattice operators are non-perturbatively renormalized using the Rome-Southampton method and the quadratic divergences are studied and removed. This is an important but notoriously difficult calculation, requiring high statistics on a large volume. In this work we take a major step towards the computation of the physical $K \to \pi\pi$ amplitudes by performing a complete calculation at unphysical kinematics with pions of mass 422 MeV and 329 MeV at rest in the kaon rest frame. With this simplification we are able to resolve $\mathrm{Re}(A_0)$ from zero for the first time, with a 25% statistical error on the 16^3 lattice and 15% on the 24^3 lattice. The complex amplitude A_2 is calculated with small statistical errors. We obtain the $\Delta I = 1/2$ rule with an enhancement factor of 9.1(21) and 12.0(17) on these two ensembles. From the detailed analysis of the results we gain a deeper understanding of the origin of the $\Delta I = 1/2$ rule. We also calculate the complex amplitude A_0, a calculation central to understanding and testing the

standard model of CP violation in the kaon system. The final result for the measure of direct CP violation, ϵ', calculated at unphysical kinematics has an order of 100% statistical error, so this only serves as an order of magnitude check.

Contents

List of Tables

List of Figures

ACKNOWLEDGMENTS

I would like to thank my advisor Prof. Norman Christ very much for his guidance, suggestions, encouragements, and help during my research at Columbia University. I really enjoyed the weekly discussions, and learned a lot.

I am grateful to Prof. Robert Mawhinney for insight discussions, help on the machines and other suggestions. I would also like to thank Prof. Chris Sachrajda, Armarjit Soni, Taku Izubuchi for instructions, help on all kinds of problems. I greatly appreciate Elaine Goode's help and her diligent work on checking some of the calculations I performed.

I enjoyed working and benefited a lot from all my colleagues: Tom Blum, Peter Boyle, Chris Dawson, Chulwoo Jung, Chris Kelly, Changhoan Kim, Zhongjie Lin, Hantao Yin, Jianglei Yu. I would like to thank all of them for the discussions and help.

Chapter 1

Introduction

Since the discovery of Parity (P) non-conservation in weak decays in 1956 by Lee and Yang [2], the perfect solution to the $\theta - \tau$ puzzle, followed by the experimental confirmation in β decay by Wu *et al* [3], there have been lots of efforts to search for discrete symmetry violations. In 1964, Charge-Parity (CP) violation was observed in neutral kaon decays where the long lived kaon decays to the CP even state with two pions at a branching ratio of order 10^{-3} [4], where the dominant decay mode is the CP odd three-pion state. The majority of this CP violation effect comes from the $K^0 - \overline{K}^0$ mixing, but the CP violation arising solely from decay was also observed [5]. Later, CP violation is observed in many B meson decay channels with a much larger effect (for example, see reference [6]). As symmetries are the foundation stone of physical theories, the discovery of these discrete symmetry violations is extremely interesting to us.

Theoretically, our current understanding is that all these discrete symmetry violations arise from the weak interaction, which violates parity and charge conjugation

symmetry in the strongest possible way, and CP in a relatively milder way. We always assume that CPT is a good symmetry, since any Lorenz invariant local field theory satisfies CPT symmetry. Therefore, CP violation naturally indicates Time (T) reversal symmetry violation. All these discrete symmetry-breaking effects are only observed in the weak interaction. They are perfect symmetries for the strong interaction and Electro-Magnetism (EM). The full theory that includes EM, Weak and Strong interactions but not gravity is called Standard Model(SM), which is a gauge theory of U(1)×SU(2)×SU(3) with three generations of fermions. The U(1)×SU(2) local gauge symmetry is spontaneous broken to U(1) symmetry by the Higgs mechanism, giving rise to the Quantum Electrodynamics (QED) of U(1) symmetry and massive weak interaction exchange bosons.

We believe that we have fully understood EM interaction with the theory of QED, partly because of its simplicity (a single parameter of the coupling strength 1/137), and the high precision agreement with experiments. For example, the electron g factor was measured to agree with theory within 10 significant digits.

On the other hand, Quantum Chromodynamics (QCD) for the strong interaction is more difficult to be precisely checked because the strong coupling α_s is of at order 1 at low energy scale. It cannot be solved analytically with perturbation series as in QED. In fact, there are still no analytical solutions to any low energy QCD problems. In year 2000, an analytical proof for the quark confinement in QCD was listed as one of the seven millennium-prize problems, and it is still not solved. Because SU(3) is a non-abelian group, gluons interact with each other and it makes the strong interaction much more complicated and interesting. The vacuum polarization effect actually enhances the field at large distance, which is believed to be one source of the quark

confinement effect. However, a full understanding of it requires a non-perturbative treatment.

Lattice regularization is the only currently known non-perturbative approach to solve QCD problems. In the past few decades, Lattice QCD algorithms have improved significantly and the computing power also becomes many orders of magnitude greater. With lattice QCD techniques, we can clearly demonstrate the quark confining linear potential, the meson and baryon spectrum, the decay constants, and the nuclear form factors. All of these calculations so far agree with experiments, which are clear demonstration of the powerful of lattice technique and the correctness of the theory for strong interaction.

The least understood part of the standard model is the weak interaction. Firstly, the Higgs particle that gives mass to all other particles has not yet been confirmed to be observed. Secondly, it is a much more complex theory in the sense of number of parameters. Except for the coupling constants of QED and QCD, and the possibly zero valued QCD vacuum angle, all other 16 parameters out of 19 are essentially related to the weak interaction. It has built-in parity violation: the left-handed fermion fields belong to the fundamental representation of SU(2), and the right-handed fermion fields belong to the singlet representation. It also has built-in charge-parity violation from a single complex phase in the Yukawa couplings, which is incorporated in the CKM matrix, known as the Kobayashi-Maskawa (KM) mechanism. This theory of weak interaction with explicit P and CP violation has successfully explained all currently observed experiments that can be theoretically calculated. However, because of its complexity and the interesting special (unnatural) features, people have been very actively searching for discrepancies, mainly concentrated on checking the

consistency of CKM matrix elements, especially on the complex CP violation phase. Any discrepancy for CP violation from the SM, if observed, asks for new physics and it could be very exciting. Besides, the CP violation in the SM is far too small to explain the currently observed matter-antimatter imbalance in the universe. So we may expect some new sources of CP violation.

The difficulty in checking the weak interaction theory arises from the non-pertubative feature of QCD. The Weak interaction itself is weak, so we can easily deal with it using perturbation theory. However, for the non-leptonic decay process, such as kaon to two-pion decay, the interplay with the strong interaction can have a dramatic effect on the results. Therefore, we have to deal with the low energy QCD problem. The asymptotic freedom of QCD allows a perturbative treatment for the short distance effects. The common strategy to solve the non-leptonic decay problem is to split the energy scale to low ($< \mu$) and high ($> \mu$), and deal with the high-energy part using perturbation theory. Ultimately, the low-energy part of the weak matrix elements becomes a pure QCD problem, and is solved using lattice QCD techniques.

In this work, we work on the kaon to two-pion decay. First, we want to check whether the observed CP violation, where 40 years experimental work produced the result $\mathrm{Re}(\epsilon'/\epsilon)$=1.65(26) $\times 10^{-3}$ [7], can be quantitatively explained by the KM mechanism. Second, we want to understand the factor of 22.5 enhancement of the $I = 0, K \to \pi\pi$ decay amplitude A_0 relative to the $I = 2$ amplitude A_2, the so-called $\Delta I = 1/2$ rule. Starting from the full SM theory, integrating out the heavy degrees of freedom by operator product expansion, we are left with an effective Hamiltonian, where the Wilson coefficients (short distance physics) are calculated using perturbation theory, and the weak matrix element (long distance, low energy physics) are

calculated with lattice QCD techniques.

Using lattice QCD techniques to calculate the weak matrix elements has been studied for 30 years. However, the first trials using Wilson fermions or staggered fermions have the problem of strong chiral symmetry breaking or flavor breaking, and therefore inducing complicated operator mixings, so it failed [8]. The introduction of Domain Wall Fermion (DWF) provides a good control over the chiral symmetry violation. The first quenched DWF chiral perturbation theory based calculation showed promising results [9], but a later more careful 2+1 flavors dynamic DWF simulation showed that there is a huge ($\sim 100\%$) systematic error using chiral perturbation theory at the scale of kaon mass to relate the $K \to \pi\pi$ to $K \to \pi$ calculation [10](However, there are on going efforts using chiral perturbation theory [11]).

We have came out a direct, complete first principle calculation in this work. This is an unusually difficult calculation because of the presence of disconnected graphs. However, with increasing computing power and the development of improved algorithms, calculations with disconnected graphs are now no longer out of reach. In fact, our recent successful calculation of the masses and mixing of the η' and η mesons [12] was carried out in part to develop and test the methods needed for the calculation presented here. In this work, we present a first direct calculation of the complete $K^0 \to \pi\pi$ decay amplitude. At this stage, we work with the simplified kinematics of a threshold decay in which the kaon is at rest and decays into two pions each with zero momentum and with mass one-half that of the kaon. The calculation with this choice of kinematics still contains the main difficulties we need to overcome in order to be able to compute the physical $K \to \pi\pi$ decay amplitudes; i.e. the presence of disconnected diagrams coupled with the need to subtract ultraviolet

power divergences. However, as explained below, with the pions at rest we are able to generate sufficient statistics to explore how to handle these difficulties. We stress that at this simplified choice of kinematics, we compute the $K \to \pi\pi$ amplitudes directly and completely.

The isospin zero $\pi - \pi$ final state implies the presence of disconnected graphs in correlation functions and makes the calculation very difficult. For these graphs, the noise does not decrease with increasing time separation between the source and sink, while the signal does. Therefore, substantial statistics are needed to obtain a clear signal. This difficulty is compounded by the presence of diagrams that diverge as $1/a^2$ as the continuum limit is approached (a is the lattice spacing). While these divergent amplitudes must vanish for a physical, on-shell decay they substantially degrade the signal to noise ratio even for an energy-conserving calculation such as this one. Studying the properties of the $1/a^2$ terms and learning how to successfully subtract them is one of the important objectives of this calculation. The chiral symmetry needed to control operator mixing is provided by our use of domain wall fermions.

Recognizing the difficulty of this problem, we choose to perform this first calculation on a lattice which is relatively small ($16^3 \times 32 \times 16$ and $24^3 \times 64 \times 16$) compared to those used in other recent work and to use somewhat heavy pion masses (422 MeV and 329 MeV) so we can more easily collect large statistics. We concentrate on exploring and reducing the statistical uncertainty since the primary goal of this work is to extract a clear signal for these amplitudes. Therefore, the quoted errors on our results are statistical only.

We further used two major techniques to reduce the computation demand. First,

the EigCG algorithm was used to speed up the calculation (see section 3.4), and it turns out to speed up the light quark mass calculation by a factor of 5.5 for the $24^3 \times 64 \times 16$ lattice. Second, we used time-separated $\pi - \pi$ sources to suppress the vacuum noise, and in effect, it effectively increases the statistics by a factor of 4.

The main objective of this work is to calculate the $\Delta I = 1/2$ decay amplitude A_0. A calculation of the $\Delta I = 3/2$ part is included here for comparison and completeness. A much more physical calculation of this $\Delta I = 3/2$ amplitude alone can be found in [13]. In the case of the $I = 2$ final state no disconnected diagrams appear, there are no divergent eye diagrams and isospin conservation requires that four valence quark propagators must join the kaon and weak operator with the operators creating the two final-state pions. This allows physical kinematics with non-zero final momentum to be achieved by imposing anti-periodic boundary conditions on one species of valence quark [14, 15]. As a result, the calculation of A_2 reported in Ref. [13] is performed at almost physical kinematics on a lattice of spatial size 4.5 fm and determines complex A_2 with controlled errors of $O(10\%)$. The present work is intended as the first step toward an equally physical but much more challenging calculation of A_0.

While we do not employ physical kinematics, the final results for the complex amplitudes A_0 and A_2 presented in this work are otherwise physical. In particular, we use Rome-Southampton methods [16] to change the normalization of our bare lattice four-quark operators to that of the RI/MOM scheme. A second conversion to the $\overline{\text{MS}}$ scheme is then performed using the recent results of Ref. [17]. Finally these $\overline{\text{MS}}$-normalized matrix elements are combined with the appropriate Wilson coefficients [18], determined in this same scheme, to obtain our results for A_0 and A_2. Because of our unphysical, threshold kinematics and focus on controlling the statisti-

cal errors associated with the disconnected diagrams, we do not estimate the size of possible systematic errors. Similarly we do not include the systematic or statistical errors associated with the Rome-Southampton renormalization factors, both of which could be made substantially smaller than our statistical errors when required.

Based on the above discussions, we explain the details and organize this work as follows: in Chapter 2 we review the standard model and the phenomenology of the neutral kaon decays; the basic lattice QCD techniques such as algorithms and data analysis are discussed in Chapter 3; Chapter 4 summarizes all the building blocks of a lattice QCD calculation of the decay amplitudes; Chapter 5 and 6 give results from a $16^3 \times 32$ lattice ensemble and a $24^3 \times 64$ lattice ensemble; finally, Chapter 7 summarizes and discusses all results and future perspectives.

Chapter 2

Kaon Decay in the Standard Model

In this chapter, we first review the structure of the Standard Model(SM), and show how parity and charge-parity violation are built into the weak interaction theory. Then the phenomenology of the $\Delta I = 1/2$ rule and measures of CP violation for both direct CP violation and indirect CP violation are explained. The relationship of these measures to the isospin decay amplitudes A_2 and A_0 is shown. After that, we determine the value for $\mathrm{Re}(A_2)$ and $\mathrm{Re}(A_0)$ from experiments, and describe our conventions. At the end, we integrate out the heavy degrees of freedom by operator product expansion, and arrive at an effective field theory with u, d, s dynamic quark degrees of freedom, the matrix elements of which can be calculated with lattice QCD.

2.1 The Standard Model

The Standard Model(SM) describes all the interactions except gravity. The full Lagrangian is

$$L_{\rm SM} = L_{\rm G} + L_{\rm FG} + L_{\rm HF} + L_{\rm HG}, \tag{2.1}$$

where $L_{\rm G}$ is the Lagrangian of the $SU(3)_C \times SU(2)_L \times U(1)_Y$ gauge field; $L_{\rm FG}$ is the Fermion-Gauge field interaction term; $L_{\rm HF}$ is the Higgs-Fermion coupling term; and $L_{\rm HG}$ is the Higgs-Gauge interaction term.

The Gauge Field Lagrangian $L_{\rm G}$ expressed in terms of the color field strength $G^a_{\mu\nu}$, Electro-Weak(EW) field strength $W^i_{\mu\nu}$ and $B_{\mu\nu}$ is

$$L_{\rm G} = -\frac{1}{4} G^a_{\mu\nu} G^{\mu\nu a} - \frac{1}{4} W^i_{\mu\nu} W^{\mu\nu i} - \frac{1}{4} B_{\mu\nu} B^{\mu\nu}, \tag{2.2}$$

where index a runs from 1 to 8, and i runs from 1 to 3, which are the number of generators for $SU(3)$ and $SU(2)$ group respectively.

The fermion field Lagrangian including the interaction term with the gauge field (in terms of the covariant derivative) is

$$\begin{aligned} L_{\rm FG} &= \overline{\psi}_A i\gamma^\mu D_\mu \psi_A & (2.3)\\ &= \overline{\psi}_A i\gamma^\mu \{\partial_\mu + i g_3 G^a_\mu \frac{\overline{\lambda}^a}{2} + i g_2 W^i_\mu \frac{\overline{\sigma}^i}{2} + i g_1 B_\mu \frac{\overline{y}}{2}\} \psi_A, & (2.4) \end{aligned}$$

where the fermion field includes 3 generations (index A), and the left-handed components comes in $SU(2)$ doublets while the right-handed components are in $SU(2)$ singlet representation (*explicit built-in Parity violation*) :

$$\psi_A = \{(\nu_{eL}, e_L), e_R, (u_L, d_L), u_R, d_R\}^T_A, \quad A = 1, 2, 3. \tag{2.5}$$

We suppress the color index for the quark fields for simplicity. Notice that in $L_{\rm HG}$, the weak interaction term W_μ changes flavor. The matrices of generators expressed in terms of $SU(3)$ generators λ^a and $SU(2)$ generators σ^i are

$$\overline{\lambda}^a = \mathrm{diag}\{0,0,0,\lambda^a\otimes I^2,\lambda^a,\lambda^a\}, \tag{2.6}$$

$$\overline{\sigma}^i = \mathrm{diag}\{\sigma^i,0,\sigma^i,0,0\}, \tag{2.7}$$

$$\overline{y} = \mathrm{diag}\{-1,-1,-2,1/3,1/3,4/3,-2/3\}. \tag{2.8}$$

y is the hypercharge and relates to particle charge through the relationship $Y = 2(Q - T_3)$ with T_3 be the 3rd component of the $SU(2)_L$ weak isospin.

The Higgs-Gauge interaction term is (Φ is a complex $SU(2)$ doublet)

$$L_{\rm HG} = D^\mu\Phi^\dagger D_\mu\Phi + \mu^2\Phi^\dagger\Phi - \lambda(\Phi^\dagger\Phi)^2. \tag{2.9}$$

It is a ϕ^4 theory with a negative mass term, so it undergoes spontaneous symmetry breaking. Choosing a fixed gauge, $\Phi(x)$ can be expressed as $(0,(v+\eta(x))/\sqrt{2})^T$, and we have a single massive Higgs Field:

$$V(\Phi) = V(\eta) = v^2\eta^2 + \lambda v\eta^3 + \frac{1}{4}\lambda\eta^4. \tag{2.10}$$

The other three degrees of freedom are eaten by the Gauge field, so the $W^\pm$ and Z^0 gain mass. The gauge symmetry $SU(2)_L\times U(1)$ spontaneously breaks to $U(1)_{\rm EM}$, with a single massless photon field.

Yukawa type interaction is introduced for the Higgs-Fermion interaction:

$$L_{\rm HF} = -f^{(u)}_{AB}\overline{q}_{LA}\widetilde{\Phi}u_{RB} - f^{(d)}_{AB}\overline{q}_{LA}\Phi d_{RB} - f^{(l)}_{AB}\bar{l}_{LA}\Phi_{RB}. \tag{2.11}$$

Under the spontaneous symmetry breaking of the Higgs field, the fermion fields gain mass (Higgs mechanism, notice that there is no neutrino term, so in the current SM,

neutrinos are massless) and their couplings to the Higgs field are proportional to their mass.

With the Higgs mechanism, removing the meaningless phase factors, and keeping the mass matrix diagonal (change from gauge basis states to mass basis states), the electro-weak interaction term in $L_{\rm FG}$ can be expressed as

$$L_{\rm EW}^{\rm int} = L_{\rm CC} + L_{\rm NC}, \tag{2.12}$$

where the charged current interactions and neutral current interactions are

$$L_{\rm CC} = \frac{g_2}{2\sqrt{2}}(J_\mu^+ W^{+\mu} + J_\mu^- W^{-\mu}), \tag{2.13}$$

$$L_{\rm NC} = -eJ_\mu^{em} A^\mu + \frac{g_2}{2\cos(\theta_W)} J_\mu^0 Z^\mu, \tag{2.14}$$

and the charged current, neutral electromagnetic and weak currents are given by

$$J_\mu^+ = \{(\overline{u}d') + (\overline{\nu}_e e) + ...(\text{othergeneration})\}_{\rm V-A}, \tag{2.15}$$

$$J_\mu^{em} = \sum_f Q_f \overline{f}\gamma_\mu f, \tag{2.16}$$

$$J_\mu^0 = \sum_f \overline{f}\gamma_\mu (T_3^f - 2Q_f \sin^2\theta_W - T_3^f\gamma_5) f. \tag{2.17}$$

Notice that in this expression the charged weak currents now include d' (weak eigenstates) instead of d (mass eigenstates). The rotation matrix from d to d' is called Cabibbo-Kobayashi-Maskawa (CKM) matrix V_{CKM},

$$\begin{pmatrix} d' \\ s' \\ b' \end{pmatrix} = \begin{pmatrix} V_{ud} & V_{us} & V_{ub} \\ V_{cd} & V_{cs} & V_{cb} \\ V_{td} & V_{ts} & V_{tb} \end{pmatrix} \begin{pmatrix} d \\ s \\ b \end{pmatrix}. \tag{2.18}$$

Therefore, the weak interaction allows a change of generations. The CKM matrix is parameterized by four parameters, three rotation angles plus a complex phase. *In the*

SM, all CP violation effects come from this single complex phase. This is a strong constraint on the SM since there are many observed CP violation channels and we can determine the complex phase in different ways. If there were only two generations of fermions, no complex phase would exist and there would be no CP violation in SM. The numerical values for the CKM matrix elements that we need to use are summarized in Table. 1 based on the 2010 PDG book [7].

2.2 Phenomenology of Neutral Kaon Decays and CP Violation

To study the neutral kaon decay, we have to start from $K^0 - \overline{K}^0$ mixing because they are not weak eigenstates. They mix through the box diagram in SM as shown in Fig. 1. Based on the quantum number of the neutral kaons, the K^0 state can be written as the combination $K^0 = \overline{s}\gamma_5 d$ which CP changes to its antiparticle $\overline{K}^0 = \overline{d}\gamma_5 s$. We choose phase conventions so that:

$$CP\left|K^0\right\rangle = -\left|\overline{K}^0\right\rangle, \quad CP\left|\overline{K}^0\right\rangle = -\left|K^0\right\rangle. \tag{2.19}$$

With mixing, the time evolution of the $K^0 - \overline{K}^0$ system is described by

$$i\frac{d}{dt}\left|\psi(t)\right\rangle = \hat{H}\left|\psi(t)\right\rangle, \qquad \psi(t) = \begin{pmatrix} a(t) \\ b(t) \end{pmatrix} = a(t)\left|K^0\right\rangle + b(t)\left|\overline{K}^0\right\rangle, \tag{2.20}$$

where the effective Hamiltonian matrix $\hat{H} = \left\langle K_i^0 | H_{eff} | K_j^0 \right\rangle$ can be written as

$$\hat{H} = \hat{M} - i\frac{\hat{\Gamma}}{2} = \begin{pmatrix} M - i\frac{\Gamma}{2} & M_{12} - i\frac{\Gamma_{12}}{2} \\ M_{12}^* - i\frac{\Gamma_{12}^*}{2} & M - i\frac{\Gamma}{2} \end{pmatrix}. \tag{2.21}$$

The diagonal elements are required to be equal by CPT invariance, and the matrix $\hat{M}$ and $\hat{\Gamma}$ are hermitian (For more details, see chapter 12 of [19]).

If CP symmetry was preserved, then

$$\left\langle K^0|H_{eff}|\overline{K}^0\right\rangle = \left\langle K^0|(CP)^{-1}CPH_{eff}(CP)^{-1}CP|\overline{K}^0\right\rangle = \left\langle \overline{K}^0|H_{eff}|K^0\right\rangle. \quad (2.22)$$

This would imply that M_{12} and Γ_{12} are real and the mass eigenstates would be just the CP eigenstates

$$\left|K^0_\pm\right\rangle = \frac{1}{\sqrt{2}}(\left|K^0\right\rangle \mp \left|\overline{K}^0\right\rangle), \quad CP\left|K^0_\pm\right\rangle = \pm\left|K^0_\pm\right\rangle. \quad (2.23)$$

In the actual CP-violating world, the mass eigenstates can be found by diagonalizing the hermitian Hamiltonian matrix 2.21. After some algebra, the eigenstates are found to be

$$K_S = \frac{K^0_+ + \overline{\epsilon}K^0_-}{\sqrt{1+|\overline{\epsilon}|^2}}, \quad (2.24)$$

$$K_L = \frac{K^0_- + \overline{\epsilon}K^0_+}{\sqrt{1+|\overline{\epsilon}|^2}}, \quad (2.25)$$

and eigenvalues are

$$M_{L/S} = M \pm \mathrm{Re}Q, \quad \Gamma_{L/S} = \Gamma \mp 2\mathrm{Im}Q, \quad (2.26)$$

where $\overline{\epsilon}$ is determined from

$$\frac{1-\overline{\epsilon}}{1+\overline{\epsilon}} = \sqrt{\frac{M^*_{12} - i\frac{\Gamma^*_{12}}{2}}{M_{12} - i\frac{\Gamma_{12}}{2}}} \quad (2.27)$$

and

$$Q = \sqrt{\left(M_{12} - i\frac{\Gamma_{12}}{2}\right)\left(M^*_{12} - i\frac{\Gamma^*_{12}}{2}\right)}. \quad (2.28)$$

The mixing can be directly observed from experiments by looking at the oscillation of the K^0 or $\overline{K}^0$ as a function of time. The mass difference $\delta m = M_L - M_S$ is accurately measured in this way to be $0.3480(6) \times 10^{-12}$ MeV. It can also be directly calculated from the standard model with the box diagrams. There are also first trial calculation using lattice QCD to include long distance effects [20].

The parameter $\bar{\epsilon}$ is a measure of the strength of mixing, and it is of the order of 10^{-3}. Since the two-π ground state has positive CP and the three-π ground state has negative CP, K_S decays to 2π and K_L decays to 3π predominately via the CP conserving decay modes. By examining the phase space of two particle final state and that of three particle final state, it can be explained why the K_L lives about 1000 times longer. From Eq. 2.25, K_L also includes a CP even piece, so it can directly decay to two pions without explicitly violating CP during decay. This is the so-called indirect CP violation that was first observed in 1964 [4]. It is convention to use parameter ϵ as a measure of indirect CP violation,

$$\varepsilon = \frac{A(K_L \to (\pi\pi)_{I=0})}{A(K_S \to (\pi\pi)_{I=0})}. \tag{2.29}$$

The advantage is that it is independent of the phase convention of K^0 and $\overline{K}^0$.

Later experiments confirmed that CP violation also happens during the decay process (for a review, see the chapter CP violation in meson decays in [7]). This is called direct CP violation and is measure by the parameter ϵ'. Therefore, K_L in Eq. 2.25 can decay to two pions in two different ways: the K_+ component decays to two pions without CP violation (indirect CP violation); the K_- component decays to two pions by violating CP explicitly (direct CP violation). Both ϵ and ϵ' are

determined from experiment by calculating the following two quantities

$$\eta_{+-} = |\eta_{+-}|e^{i\phi_{+-}} = \frac{A(K_L \to \pi^+\pi^-)}{A(K_S \to \pi^+\pi^-)}, \tag{2.30}$$

$$\eta_{00} = |\eta_{00}|e^{i\phi_{00}} = \frac{A(K_L \to \pi^0\pi^0)}{A(K_S \to \pi^0\pi^0)}, \tag{2.31}$$

and we have

$$\eta_{+-} = \epsilon + \epsilon', \qquad \eta_{00} = \epsilon - 2\epsilon'. \tag{2.32}$$

The current experiment values are

$$|\epsilon| = 2.228(11) \times 10^{-3}, \tag{2.33}$$

$$\mathrm{Re}\,(\epsilon'/\epsilon) = 1.65(26) \times 10^{-3}. \tag{2.34}$$

These numbers show that CP violating events in kaon decays are very rare, especially for the direct CP violation. Therefore, even after 30 years of experimental endeavor, ϵ' still has relative large error.

Since the up and down quark mass are very small compared to the scale of QCD, it is observed that isospin symmetry is a very good symmetry. Because of Bose symmetry, the final two-π state can only be in isospin 0 or isospin 2 states. For theoretical simplicity, it is convenient to study the decay amplitudes in the specific isospin channels, A_0 and A_2,

$$A(K^0 \to \pi\pi(I)) = A_I e^{i\delta_I}, \tag{2.35}$$

where δ_I is the strong phase from the $\pi - \pi$ interactions. From CPT symmetry, we also have

$$A(\overline{K}^0 \to \pi\pi(I)) = -A_I^* e^{i\delta_I}. \tag{2.36}$$

If A_I was real, then applying CP on Eq. 2.36 we would get back to Eq. 2.35 and that means CP is a good symmetry. Therefore, the imaginary parts of the decay amplitudes are the CP violating amplitudes. Without CP violation, the decay amplitudes A_I are actually all real.

We can rewrite ϵ and ϵ' in terms of the quantities in isospin channel 0 and 2,

$$\epsilon = \bar{\epsilon} + i\left(\frac{\mathrm{Im}A_0}{\mathrm{Re}A_0}\right), \tag{2.37}$$

$$\epsilon' = \frac{ie^{i(\delta_2-\delta_0)}}{\sqrt{2}}\frac{\mathrm{Re}A_2}{\mathrm{Re}A_0}\left[\frac{\mathrm{Im}A_2}{\mathrm{Re}A_2} - \frac{\mathrm{Im}A_0}{\mathrm{Re}A_0}\right]. \tag{2.38}$$

Both of expressions are phase convention independent. There are two important things we want to understand in this thesis,

1. $\Delta I = 1/2$ rule. Experimental value for the ratio $\mathrm{Re}A_0/\mathrm{Re}A_2$ is about 22.5 (see next section). We want to understand where this huge ratio comes from. Wilson coefficients evaluated at a QCD scale of about 2 GeV represent the short distance physics and can be evaluated from perturbation theory. However, these factors explain only a factor of 2 enhancement of the $I = 0$ amplitude [21, 22]. The remaining enhancement must arise from the hadronic matrix elements which require non-perturbative treatment.

2. Direct CP violation. Notice that $\mathrm{Im}(A_0)$ and $\mathrm{Im}(A_2)$ are CP violating amplitudes. If they have the same sign which is true in fact, there will be cancelations for the direct CP violation measure ϵ', and ϵ' is not necessarily non-zero even if there is actual direct CP violation in each individual channel. We want to see whether the SM can quantitatively explain the experimental value $\mathrm{Re}\,(\epsilon'/\epsilon) = 1.65(26) \times 10^{-3}$ for direct CP violation to check the KM mechanism of CP violation with a single complex phase.

2.3 Determination of Re(A_2) and Re(A_0) from Experiments

The decay rate of an unstable particle to two particle final state is

$$\Gamma = \frac{1}{2m_K}\int \frac{d\Omega}{4\pi}\frac{1}{8\pi}\frac{2|\vec{p}|}{m_K}|A(K\to\pi\pi)|^2 \tag{2.39}$$

$$= \frac{1}{8\pi}\frac{|\vec{p}|}{m_K^2}|A(K\to\pi\pi)|^2. \tag{2.40}$$

Based on this formula, the experimentally measured decay widths for $K_s \to \pi^+\pi^-$, $K_s \to \pi^0\pi^0$, and $K^+ \to \pi^+\pi^0$ are related to the corresponding decay amplitudes:

$$\Gamma_{+-} = \frac{1}{8\pi}|A_{+-}|^2\frac{\sqrt{m_{K^0}^2/4 - m_{\pi^+}^2}}{m_{K^0}^2} \tag{2.41}$$

$$\Gamma_{00} = \frac{1}{8\pi}|A_{00}|^2\frac{\sqrt{m_{K^0}^2/4 - m_{\pi^0}^2}}{m_{K^0}^2} \tag{2.42}$$

$$\Gamma_{+0} = \frac{1}{8\pi}|A_{+0}|^2\frac{p_{+0}}{m_{K^0}^2}, \tag{2.43}$$

where

$$\begin{aligned} p_{+0} =& \sqrt{(m_{K^+} - m_{\pi^+} - m_{\pi^0})(m_{K^+} + m_{\pi^+} + m_{\pi^0})(m_{K^+} - m_{\pi^+} + m_{\pi^0})} \\ & \cdot \sqrt{(m_{K^+} + m_{\pi^+} - m_{\pi^0})}/2m_{K^+}. \end{aligned} \tag{2.44}$$

Based on the experimental values that summarized in Table.2, it is straightforward to work out the magnitude of decay amplitudes:

$$|A_{+-}| = 3.9207(25)\times 10^{-7}\text{GeV}, \tag{2.45}$$

$$|A_{00}| = 2.5919(28)\times 10^{-7}\text{GeV}, \tag{2.46}$$

$$|A_{+0}| = 1.8110(51)\times 10^{-8}\text{GeV}. \tag{2.47}$$

Now let us work out the decay amplitudes in the specific isospin channels. Using the Wigner-Eckart theorem (Page 239 of [23]) it can be shown that

$$A_2 = \sqrt{\frac{2}{3}} A_{+0}. \tag{2.48}$$

plug in the value for $|A_{+0}|$, we get

$$|A_2| = 1.4787(41) \times 10^{-8} GeV. \tag{2.49}$$

Express the decay amplitudes A_{+-} and A_{00} in terms of A_0 and A_2,

$$A_{00} = \sqrt{\frac{1}{3}}|A_0|e^{i(\delta_0+\phi_0)} - \sqrt{\frac{2}{3}}|A_2|e^{i(\delta_2+\phi_2)}, \tag{2.50}$$

$$A_{+-} = \sqrt{\frac{2}{3}}|A_0|e^{i(\delta_0+\phi_0)} + \sqrt{\frac{1}{3}}|A_2|e^{i(\delta_2+\phi_2)}. \tag{2.51}$$

Canceling out the phase factor from these two equations, and using the result from K^+ decay for $|A_2|$, we get

$$|A_0| = 3.3201(18) \times 10^{-7} GeV, \tag{2.52}$$

$$|A_0/A_2| = 22.454(63). \tag{2.53}$$

Using the experimental value for the strong phase shift $\delta_2 - \delta_0 + \pi/2 = 42.3(1.5)^\circ$, and ignoring the small value of ϕ_0 and ϕ_2, we can also directly find $|A_2|$ and $|A_0|$ solely from the K_S decay by solving Eq. 2.50 and 2.51,

$$|A_2| = 1.573(56) \times 10^{-8} GeV, \tag{2.54}$$

$$|A_0| = 3.3197(19) \times 10^{-7} GeV, \tag{2.55}$$

$$|A_0/A_2| = 21.13(77). \tag{2.56}$$

In this case, because of the large uncertainty of the phase shift, $|A_2|$ has much larger error compared to the one determined from K^+ decay. These two results are consistent

within 2 sigma of the error. However, the effects of electromagnetism and isospin symmetry breaking are different in these two cases, so they supposedly have some differences. Since the imaginary part of A_2 and A_0 are about 1000 times smaller than the real part, the real parts of these decay amplitudes are approximated by their magnitudes.

One final comment about this experimental determination of A_2 and A_0 addresses how the error bar is calculated. To avoid complicated error propagation, I generated 10,000 samples for each of the experimental quantities. For each variable x with error Δx, 10,000 samples are drawn from $N(x, \Delta x)$ where $N(\mu, \sigma)$ stands for a normal distribution with mean μ and standard deviation σ. The values for A_2, A_0, etc. are calculated 10,000 times, and the average value and error are then calculated.

2.4 Effective Hamiltonian for $K^0 \to \pi\pi$ Decays

The weak decay of the neutral kaon involves all of the interactions in the SM. At a low energy scale, the non-perturbative feature of QCD complicates the problem and we have to separate it from the rest of the problem and solve it using lattice regularization. Using the operator product expansion, we get an effective Hamiltonian for $\Delta S = 1$ decays [18]:

$$H^{\Delta S=1} = \frac{G_F}{\sqrt{2}} V_{ud}^* V_{us} \sum_{i=1}^{10} [(z_i(\mu) + \tau y_i(\mu))] Q_i. \tag{2.57}$$

In this formula, we have integrated out all heavy degrees of freedom and only the up, down, and strange quarks are left as dynamic degrees of freedom. This is a form of four-fermion interaction theory where all operators contain four fermion fields. G_F

is the famous Fermi constant. $z_i(\mu)$ and $y_i(\mu)$ are called Wilson coefficients that summarize the short-distance effects. The calculation of their values is discussed in Section 4.4. The values for the CKM matrix elements V_{ud}, V_{us} and τ can be found in Tab.1.

In the actual calculation of the decay amplitudes, we need to obtain the weak matrix elements $\langle\pi\pi|Q_i(\mu)|K^0\rangle$ at the energy scale μ where the Wilson coefficients are evaluated. The μ dependence in the weak matrix elements and Wilson coefficients should cancel out and the final physical result is μ independent. Since lattice regularization is used to evaluate the weak matrix elements, we have to match it to the $\overline{\text{MS}}$ scheme in which the Wilson coefficients are evaluated. This is discussed in Section 4.5.

The detailed structure of the ten operators in Eq. 2.57 is

$$Q_1 = (\bar{s}_\alpha d_\alpha)_{V-A}(\bar{u}_\beta u_\beta)_{V-A}, \tag{2.58a}$$

$$Q_2 = (\bar{s}_\alpha d_\beta)_{V-A}(\bar{u}_\beta u_\alpha)_{V-A}, \tag{2.58b}$$

$$Q_3 = (\bar{s}_\alpha d_\alpha)_{V-A} \sum_{q=u,d,s} (\bar{q}_\beta q_\beta)_{V-A}, \tag{2.58c}$$

$$Q_4 = (\bar{s}_\alpha d_\beta)_{V-A} \sum_{q=u,d,s} (\bar{q}_\beta q_\alpha)_{V-A}, \tag{2.58d}$$

$$Q_5 = (\bar{s}_\alpha d_\alpha)_{V-A} \sum_{q=u,d,s} (\bar{q}_\beta q_\beta)_{V+A}, \tag{2.58e}$$

$$Q_6 = (\bar{s}_\alpha d_\beta)_{V-A} \sum_{q=u,d,s} (\bar{q}_\beta q_\alpha)_{V+A}, \tag{2.58f}$$

$$Q_7 = \frac{3}{2}(\bar{s}_\alpha d_\alpha)_{V-A} \sum_{q=u,d,s} e_q(\bar{q}_\beta q_\beta)_{V+A}, \tag{2.58g}$$

$$Q_8 = \frac{3}{2}(\bar{s}_\alpha d_\beta)_{V-A} \sum_{q=u,d,s} e_q(\bar{q}_\beta q_\alpha)_{V+A}, \tag{2.58h}$$

$$Q_9 = \frac{3}{2}(\bar{s}_\alpha d_\alpha)_{V-A} \sum_{q=u,d,s} e_q(\bar{q}_\beta q_\beta)_{V-A}, \tag{2.58i}$$

$$Q_{10} = \frac{3}{2}(\bar{s}_\alpha d_\beta)_{V-A} \sum_{q=u,d,s} e_q(\bar{q}_\beta q_\alpha)_{V-A}, \tag{2.58j}$$

where the subscripts α and β denote the color indices, and the operators with odd indices are called color unmixed and the operators with even indices are called color mixed operators. The subscripts $V-A$ (or $V+A$) following a quark bilinear $\overline{q}q$ means a structure $\overline{q}\gamma_\mu(1-\gamma_5)q$ (or $\overline{q}\gamma_\mu(1+\gamma_5)q$) and it is a left-hand (right-hand) current.

The origin of these operators from the full theory is shown in Fig.2. There are three different types. The current-current operator contributes the dominant part of the real part of the decay amplitudes. The QCD penguin operators only contribute to the $\Delta I = 1/2$ decay amplitudes. The Electro-Weak penguin and QCD penguin operators contribute to the CP violating imaginary parts of the decay amplitudes since they involve the complex V_{dt} element of the CKM matrix. We will look at the contribution from each individual operator in Chapter 5 and 6 with numerical results.

Notice that the operators listed in Eqs. 2.58 are not all independent. They satisfy three equalities:

$$Q_{10} - Q_9 = Q_4 - Q_3, \tag{2.59a}$$

$$Q_4 - Q_3 = Q_2 - Q_1, \tag{2.59b}$$

$$2Q_9 = 3Q_1 - Q_3. \tag{2.59c}$$

Therefore, only 7 operators are independent. In Section 4.5, we will introduce the chiral operator basis which includes only 7 independent operators. In lattice calculations, Eq. 2.59 also provides identities as a check.

Chapter 3

General Lattice QCD Approach

In this chapter, we discuss the general lattice regularization approach to address low energy QCD problems. First, we introduce the Iwasaki gauge action and Domain Wall Fermion (DWF) action that we will use to generate configurations and perform measurements for this thesis. Then the hybrid Monte Carlo algorithm is described. In Section 3.2, the power of the lattice QCD method is shown in two aspects: how to obtain the mass spectrum of mesons and how to calculate the weak matrix elements from lattice QCD by calculating the Euclidean correlators. In Section 3.3, we discuss the choice of sources for the full QCD propagators: Coulomb gauge-fixed wall sources, point sources and random wall sources are explained. Because we need to calculate many (~ 100) propagators for each configuration, an efficient algorithm called EigCG is introduced in Section 3.4, which turns out to speed up the light quark propagators by a factor of 5.5 for the $24^3 \times 64 \times 16$ lattice. Finally, the last section briefly reviews the widely used jackknife and bootstrap method and correlated minimum χ^2 fitting in data analysis.

3.1 Lattice Quantum Chromodynamics

We only consider the up, down and strange quark dynamic degrees of freedom. Because the mass of up and down quarks are very small and isospin symmetry is a good symmetry, we treat $m_u = m_d \equiv m_l$. Therefore, we have a $2+1$ flavor QCD theory. The path integral written in Euclidean space is

$$\begin{aligned} Z &= \int [\mathcal{D}U_\mu] e^{-S_G[U]} \prod_i \{ [\mathcal{D}\overline{\psi_i}][\mathcal{D}\psi_i] e^{-\overline{\psi_i}(D+m_i)\psi_i} \} && (3.1) \\ &= \int [\mathcal{D}U_\mu] e^{-S_G[U]} \det(D+m_u)\det(D+m_d)\det(D+m_s) && (3.2) \\ &= \int [\mathcal{D}U_\mu] e^{-S_G[U]} \det(D+m_l)^2 \det(D+m_s), && (3.3) \end{aligned}$$

where $S_G[U]$ is the pure gauge field action. With this formalism, we convert the QCD field theory problem to a standard statistical mechanics problem with Z being the partition function. Any observable $\mathcal{O}$ can be directly measured as

$$\langle \mathcal{O} \rangle = \frac{1}{Z} \int [\mathcal{D}U_\mu] e^{-S_G[U]} \det(D+m_l)^2 \det(D+m_s) \mathcal{O}. \quad (3.4)$$

We will discuss how to perform these calculations on the lattice in the following sections. First, let us review the gauge action and fermion action with the lattice regularization.

To preserve exact gauge invariance, Wilson introduced an elegant formalism to quantize gauge fields [24]. Specifically, for QCD, the gauge field is described by link variables of SU(3) matrices that connect the fermion fields that are defined on the lattice sites. The relationship of the link variables $U_\mu(x)$ to the continuum field $A_\mu(x)$ is given by

$$U_\mu(x) = \exp(iagA_\mu(x)) \quad (3.5)$$

and a gauge invariant action is

$$S_G^W[U] = -\frac{\beta}{3}\sum_{x,\mu<\nu} P[U]_{x,\mu\nu}. \tag{3.6}$$

It can be easily checked that, if we choose $\beta = 6/g^2$ and assume that gaA_μ is small, then Eq. 3.6 agrees with the continuum limit result:

$$S_G^{cont.} = \frac{1}{4}\int d^4x F_{\mu\nu}F_{\mu\nu} \tag{3.7}$$

with a leading order discretization error of $O(a^2)$. Notice that in Eq. 3.6, $P[U]_{x,\mu\nu}$ stands for the real part of the trace of the path ordered product of links around the 1×1 plaquette at point x in the μ, ν plane.

In this thesis, we use an improved gauge action which also contains the 1×2 plaquettes $R[U]_{x,\mu\nu}$

$$S_G[U] = -\frac{\beta}{3}[(1-8c_1)\sum_{x;\mu<\nu} P[U]_{x,\mu\nu} + c_1 \sum_{x;\mu\neq\nu} R[U]_{x,\mu\nu}]. \tag{3.8}$$

There are two common choices for the constant c_1 depending on the different approximations to the renormalization group trajectory: the Iwasaki action [25, 26] with $c_1 = -0.331$ and DBW2 action [27] with $c_1 = -1.4069$. The improved actions have better rotation symmetry and chiral symmetry properties. We use the Iwasaki gauge action for all the ensembles studied in this thesis.

Now let us introduce the fermions to the space-time lattice and figure out the best action we are going to use. The naive discretization fails because of the fermion doubling problem [28]. The so-called Wilson fermion formulation adds a second derivative term which vanishes in the continuum limit to make the doublers very heavy so they decouple from the system. However, it strongly violates the chiral symmetry that the

original theory possesses for vanishing fermion mass:

$$\psi \to e^{i\theta\gamma_5}\psi \quad ; \quad \overline{\psi} \to \overline{\psi}e^{i\theta\gamma_5}. \tag{3.9}$$

Since chiral symmetry is crucial for our $K \to \pi\pi$ decay calculations to avoid complicated operator mixings [8], Wilson fermions are not a good choice.

The other commonly used fermion action is the staggered fermion action [29] which is computationally much cheaper than other formulations. However, it suffers from the problems of flavor symmetry breaking and taking the suspicious fourth root of the staggered determinant [30, 31]. Therefore, we avoid using it here too.

Nielsen and Ninomiya proved that a local, real, free fermion lattice action, having chiral and translation invariance must have the doubling problem [32]. Therefore, we have to give up something to get rid of the doublers, e.g, chiral symmetry for Wilson fermion. However, we are actually in a much better situation by the work of Ginsparg and Wilson (GW) [33]. They define the chiral symmetry based on the GW-relation:

$$\{\gamma_5, D\} = aD\gamma_5 D, \tag{3.10}$$

where a is the lattice spacing and the curly parenthesis $\{\}$ stands for anti-commutator. With this definition of chiral symmetry on the lattice, both chiral symmetry and locality and be preserved. Narayanan and Neuberger derived a gauge covariant solution to the Ginsparg-Wilson relation of Eq. 3.10, and it is called overlap fermions [34]. Because of its demanding computation cost and the problem of fixed topology, we use an approximation to the overlap fermion action: the domain wall fermion action. It has very good chiral symmetry that is controlled by the length of the fifth dimension L_s. As L_s goes to infinity, we recover the overlap fermion action and the exact chiral symmetry. In contrast to the overlap fermions, the domain wall formulation can

also be used with a gauge action which allows the transition of topological charge, therefore ensuring egodicity.

The domain wall fermion formulation of Shamir [35], and Furman and Shamir [36] with fermion mass m_f is given by

$$D^{\rm DWF}_{x,s;x',s'}(M_5,m_f) = \delta_{s,s'}D^{\parallel}_{x,x'}(M_5) + \delta_{x,x'}D^{\perp}_{s,s'}(m_f), \tag{3.11}$$

where $D^{\parallel}_{x,x'}(M_5)$ is the Wilson fermion kernel with negative mass -M_5($0 < M_5 < 2$) :

$$\begin{aligned} D^{\parallel}_{x,x'}(M_5) &= \frac{1}{2}\sum_{\mu=1}^{4}\Big[(1-\gamma_\mu)U_{x,\mu}\delta_{x+\hat{\mu},x'} + (1+\gamma_\mu)U^{\dagger}_{x',\mu}\delta_{x-\hat{\mu},x'}\Big] \\ &+ (M_5-4)\delta_{x,x'} \end{aligned} \tag{3.12}$$

and

$$\begin{aligned} D^{\perp}_{s,s'}(m_f) &= \frac{1}{2}\Big[(1-\gamma_5)\delta_{s+1,s'} + (1+\gamma_5)\delta_{s-1,s'} - 2\delta_{s,s'}\Big] \\ &- \frac{m_f}{2}\Big[(1-\gamma_5)\delta_{s,L_s-1}\delta_{0,s'} + (1+\gamma_5)\delta_{s,0}\delta_{L_s-1,s'}\Big]. \end{aligned} \tag{3.13}$$

The lattice actions for domain wall fermions and the corresponding Pauli-Villars field that is introduced to cancel out unwanted bulk type infinities are [37]

$$S_F = -\sum_{i=1}^{3}\bar{\Psi}_i\left[D^{\rm DWF\dagger}(M_5,m_i)D^{\rm DWF}(M_5,m_i)\right]^{1/2}\Psi_i, \tag{3.14a}$$

$$S_{PV} = \sum_{i=1}^{3}\Phi^{\dagger}_i\left[D^{\rm DWF\dagger}(M_5,1)D^{\rm DWF}(M_5,1)\right]^{1/2}\Phi_i. \tag{3.14b}$$

The final partition function with the Iwasaki gauge action of Eq. 3.8 and the domain wall fermion action of Eq. 3.14 for $2+1$ flavors of fermions is

$$Z = \int [\mathcal{D}U_\mu]e^{-S_G[U]}\frac{\det(D^{\dagger}(m_l)D(m_l))}{\det(D^{\dagger}(1)D(1))}\frac{\det(D^{\dagger}(m_s)D(m_s))^{1/2}}{\det(D^{\dagger}(1)D(1))^{1/2}}. \tag{3.15}$$

For simplicity we have abbreviated $D^{\mathrm{DWF}\dagger}(M_5, m_i)$ as $D(m_i)$. This is the partition function with which the gauge configurations in this thesis are generated, upon which the measurements are performed.

A direct evaluation of the determinant in Eq. 3.15 is almost impossible on a moderate sized lattice. Therefore, we introduce pseudo-fermion fields ϕ_l and ϕ_s and use a Gaussian integral to represent the determinant,

$$Z = \int [\mathcal{D}U_\mu][\mathcal{D}\phi_l^\dagger][\mathcal{D}\phi_l][\mathcal{D}\phi_s^\dagger][\mathcal{D}\phi_s] e^{-S_{eff}}, \tag{3.16}$$

where the effective action is

$$\begin{aligned} S_{eff} &= S_G[U] + \phi_l^\dagger D(1)(D^\dagger(m_l)D(m_l))^{-1} D(1)^\dagger \phi_l \\ &\quad + \phi_s^\dagger (D(1)^\dagger D(1))^{1/4} (D(m_s)^\dagger D(m_s))^{-1/2} (D(1)^\dagger D(1))^{1/4} \phi_s. \end{aligned} \tag{3.17}$$

To generate configurations based on the distribution $\exp(-S_{eff})$, the Hybrid Monte Carlo (HMC) algorithm is applied. For a detailed discussion and introduction of HMC, please see chapter 16 of the reference book [28]. To evaluate the third term for the pseudo fermion ϕ_s in Eq. 3.17, rational expansion is used. The quotient and rational quotient HMC are discussed in detail by Michael Clark [38]. Other strategies are also used to speed up the calculation such as Hasenbusch's quotient split method [39] and the force gradient integrator [40, 41].

3.2 Physical Quantities from Euclidean Correlators

Let us take meson mass spectrum calculation as an example. First, we need to construct an operator O_m that carries the same quantum numbers as the specified meson. We have numerous choices for this. For example, for the π^+, we can use a *l*ocal operator

$$O_{\pi^+} = i \sum_{\vec{x}} \bar{d}(\vec{x}) \gamma_5 u(\vec{x}). \tag{3.18}$$

The correlation function that corresponds to creating a meson at time 0 and destroying it at time t is

$$\begin{aligned} C(t) &= \langle 0 | O_m^\dagger(t) O_m(0) | 0 \rangle & (3.19a) \\ &= \langle 0 | e^{Ht} O_m^\dagger(0) e^{-Ht} O_m(0) | 0 \rangle & (3.19b) \\ &= \sum_n \langle 0 | O_m^\dagger(0) e^{-Ht} | n \rangle \langle n | O_m(0) | 0 \rangle & (3.19c) \\ &= \sum_n \langle 0 | O_m^\dagger(0) | n \rangle \langle n | O_m(0) | 0 \rangle e^{-E_n t} & (3.19d) \\ &= \sum_n |\langle n | O_m(0) | 0 \rangle|^2 e^{-E_n t}. & (3.19e) \end{aligned}$$

From the second line to the third, we insert a complete set of eigenstates which have the same quantum number as the operator O_m, and use the fact that the vacuum state is time invariant $e^{-Ht}|0\rangle = |0\rangle$. Taking the large time limit, the contributions from excited high energy states are exponentially suppressed relative to the ground state. Therefore, we can extract the mass of the ground state meson (m_m) from the exponent,

$$C(t) \xrightarrow{t \to \infty} |\langle m | O_m(0) | 0 \rangle|^2 e^{-m_m t}. \tag{3.20}$$

On the lattice, the mesons can propagator through the boundaries. So we need to include the effect of the periodic boundary conditions. The correlation function becomes

$$C(t) \xrightarrow{t\to\infty} |\langle m|O_m(0)|0\rangle|^2(e^{-m_m t} + e^{-m_m(T-t)}), \tag{3.21}$$

where T is the lattice size in the time direction. For propagators contructed by adding those obeying periodic and anti-periodic boundary conditions, T should be replaced by $2T$.

At short time separation, the contamination from the excited states is not negligible. To figure out a good fitting range, we examine the effective mass plot $m_{\text{eff}}(t)$ which is calculated by solving for $m(t)$ solely from $C(t)$ and $C(t+1)$,

$$\frac{C(t+1)}{C(t)} = \frac{\cosh[m(T/2-t-1)]}{\cosh[m(T/2-t)]}. \tag{3.22}$$

Figure 3 shows a typical plot for the correlation function and a plot of effective mass of the pions using wall sources (see next section). From the plateau region, we choose the fitting range to be 6 to 31. Notice that in this calculation, we average over sources on all time slices, so the value of the correlation function from time 32 to 64 is a reflection of the value from 32 to 0. Therefore, only the time separations between 0 to 32 are shown.

We can actually work out more than the ground state. Being able to extract the low lying excited states is especially important for the case with almost degenerate ground states. If the statistics is sufficient large, we may fit two or more exponential terms directly from Eq. 3.19. To get a more reliable result, the method of solving a generalized eigenvalue problem can be used [42, 43, 44]. Suppose that we have a set of N operators O_i (i=1,2,... N) that share the same quantum numbers as those of the

states in which we are interested, the $N \times N$ correlation matrix is

$$C_{ij}(t) = \langle 0|O_i^\dagger(t)O_j(0)|0\rangle. \tag{3.23}$$

Let us keep the lowest N states only, then we can express

$$C(t) = a^\dagger \lambda_E(t) a, \tag{3.24}$$

where $a_{\alpha i} = \langle \alpha|O_i(0)|0\rangle$, $\lambda_E(t) = \mathrm{Diag}\{e^{-E_1 t}, e^{-E_2 t}, ...\}$. For the generalized eigenvalue problem:

$$C(t_0)^{-1}C(t)v(t,t_0) = \lambda(t,t_0)v(t,t_0), \tag{3.25}$$

let us plug in Eq. 3.24 and rearrange some terms to obtain:

$$\lambda_E^{-1}(t_0)\lambda_E(t) \cdot a\nu_n(t,t_0) = \lambda_n(t,t_0) \cdot a\nu_n(t,t_0). \tag{3.26}$$

It shows that the eigenvalues are $\lambda_n(t,t_0) = e^{-E_n(t-t_0)}$, and the eigenvectors are $\nu = a^{-1}$. The contamination from the neglected higher excited states is exponentially suppressed similar to the analysis of the ground state. For a detailed analysis, see appendix C of reference [44]. In actual numerical analysis, we can examine the effective mass plot for the eigenvalues of $C(t_0)^{-1}C(t)$ to get the energy of the low lying N states. A good application of this generalized eigenvalue analysis is to calculate the η and η' masses and its mixing angle. For details, see reference [12].

The above methods can be easily generalized to the determination of the baryon spectrum by choosing suitable interpolating operators. The accurate agreement of the lattice QCD results with experiments for the meson and baryon spectrum (for example, see reference [45]) not only are strong evidence that QCD is the correct theory for the strong interaction, but also shows the power of the lattice regularization to solve the non-pertubative QCD problem. With some extension, we can also

work out scattering lengths or phase shifts (Section 4.1) and weak matrix elements (Section 4.2).

For future reference, we use the following phase conventions for the meson states:

$$
\begin{array}{ll}
|\pi^+\rangle = i\overline{u}\gamma_5 d\,|0\rangle & \langle\pi^+| = \langle 0|\, i\overline{d}\gamma_5 u \\
|\pi^-\rangle = -i\overline{d}\gamma_5 u\,|0\rangle & \langle\pi^-| = -\langle 0|\, i\overline{u}\gamma_5 d \\
|\pi^0\rangle = \frac{i}{\sqrt{2}}(\overline{u}\gamma_5 u - \overline{d}\gamma_5 d)\,|0\rangle & \langle\pi^0| = \langle 0|\, \frac{i}{\sqrt{2}}(\overline{u}\gamma_5 u - \overline{d}\gamma_5 d) \\
|K^+\rangle = i\overline{u}\gamma_5 s\,|0\rangle & \langle K^+| = \langle 0|\, i\overline{s}\gamma_5 u \\
|K^-\rangle = -i\overline{s}\gamma_5 u\,|0\rangle & \langle K^-| = -\langle 0|\, i\overline{u}\gamma_5 s \\
|K^0\rangle = i\overline{d}\gamma_5 s\,|0\rangle & \langle K^0| = \langle 0|\, i\overline{s}\gamma_5 d \\
\left|\overline{K^0}\right\rangle = -i\overline{s}\gamma_5 d\,|0\rangle & \left\langle\overline{K^0}\right| = -\langle 0|\, i\overline{d}\gamma_5 s.
\end{array}
\tag{3.27}
$$

3.3 Propagator Sources

To evaluate the correlation function shown in Eq. 3.19, we only need to work out all possible Wick contractions. There is only one contraction for the single-pion case. With the local source in Eq. 3.18, the correlation function is calculated as

$$
C(t) = \left\langle \sum_{\vec{x},\vec{y}} \mathrm{Tr}\{S_u(\vec{y},t;\vec{x},0)\gamma_5 S_d(\vec{x},0;\vec{y},t)\gamma_5\} \right\rangle \tag{3.28}
$$

$$
= \left\langle \sum_{\vec{x},\vec{y}} \mathrm{Tr}\{S_u(\vec{y},t;\vec{x},0) S_d(\vec{y},t;\vec{x},0)^\dagger\} \right\rangle, \tag{3.29}
$$

where $S_i(y;x)$ stands for the full QCD propagator calculated on a specific lattice configuration and $< \cdots >$ indicates an average over configurations, with source position at x, sink position at y, quark type i (u, d or s). From the first line to the second, we

used the Hermiticity property of lattice propagators

$$S(x,y)^\dagger = \gamma^5 S(y,x)\gamma^5, \tag{3.30}$$

where † indicates the hermition conjugate of $S(x,y)$ viewed as a 12×12 spin and color matrix.

There are other properties of the lattice QCD propagators [8] (The $[U]$ in the expression of a propagator means that the propagator is calculated on the background gauge field $[U]$: S(x, y, [U])) which are very useful to explore the properties of correlation functions,

$$P : S(x,y,[U]) = \gamma^0 S(x^P, y^P, [U]^P)\gamma_0, \tag{3.31}$$

$$T : S(x,y,[U]) = \gamma^0\gamma^5 S(x^r, y^r, [U]^r)\gamma^5\gamma^0, \tag{3.32}$$

$$C : S(x,y,[U]) = \gamma^0\gamma^2 S^t(y,x,[U])\gamma^2\gamma^0, \tag{3.33}$$

where P, T, C are the parity, time-reversal and charge-conjugation operators. The symbol t denotes transpose on spin and color indices. With these symmetry properties, it can be easily shown that the expectation values of all correlation functions in this work are real.

For simplicity, we use $L(y;x)$ to stand for both $S_u(y;x)$ and $S_d(y;x)$, and $S(y;x)$ to stand for $S_s(y;x)$ in future discussions. A direct calculation of propagators at all possible positions $\vec{x}$ is computationally forbidding so a single point source is typically used, which dramatically reduces the effective statistics because there is no volume average. The point sink is summed over all spatial positions at a fixed time to project out the zero momentum state.

In this work, we adopt a Coulomb gauge fixed wall source and sink for all the pion and kaon states. Firstly, we effectively average the contribution from the whole

volume by just solving with one wall source. Secondly, numerical results show that the wall source has better overlap with the ground state of pions than the point source. With wall-type source operators,

$$O_{\pi^+} = i \sum_{\vec{x}} \sum_{\vec{y}} \overline{d}(\vec{x}) \gamma_5 u(\vec{y}), \tag{3.34}$$

the correlation function is calculated as

$$\begin{aligned} C(t) &= \mathrm{Tr}\{L(t;0)\gamma_5 L(0;t)\gamma_5\} & (3.35)\\ &= \mathrm{Tr}\{L(t;0)L(t;0)^\dagger\}, & (3.36) \end{aligned}$$

where $L(t;0) = \sum_{\vec{x},\vec{y}} L(\vec{y},t;\vec{x},0)$ is the Coulomb gauge fixed wall source to Coulomb gauge fixed wall sink propagator. Notice that we need to fix the gauge to get a non-zero correlation function, and we use five dimensional propagators evaluated with four dimensional sources and projected on four dimensional sinks. Let us work out the details since this is the standard source used in our calculation.

A Coulomb gauge fixed wall source located at the time t_w with spin α and color a is a five-dimension color and spin vector field $\mathcal{C}(\vec{x},t,s;t_w,\alpha,a)_{\beta,b}$ with spinor and color indices β and b and is given by:

$$\mathcal{C}(\vec{x},t,s;t_w,\alpha,a)_{\beta,b} = \left\{ \left(\frac{1-\gamma^5}{2}\right)_{\beta,\alpha} \delta_{s,L_s-1} + \left(\frac{1+\gamma^5}{2}\right)_{\beta,\alpha} \delta_{s,0} \right\} \delta_{t,t_w} V^C(\vec{x},t)^\dagger{}_{b,a}, \tag{3.37}$$

where $V^C(\vec{x},t)$ is the 3×3 local gauge transformation matrix that transforms the gauge links $U_i(\vec{x},t)$ into links $U_i^C(\vec{x},t)$ in Coulomb gauge:

$$U_i^C(\vec{x},t) = V^C(\vec{x},t) U_i(\vec{x},t) V^C(\vec{x}+\hat{e}_i a,t)^\dagger. \tag{3.38}$$

Here $\hat{e}_i$ is a unit vector in the i^{th} direction.

The color and spinor field $\mathcal{C}(\vec{x},t,s;t_w,\alpha,a)_{\beta,b}$ is used to define a five-dimensional propagator $G(\vec{x},t,s;t_w,\alpha,a)_{b,\beta}$ which obeys the domain wall fermion Dirac equation:

$$\sum_{x',t',s'}\left\{D^{\mathrm{DWF}}_{\vec{x},t,s;\vec{x}',t',s'}G(\vec{x}','t,s';t_w,\alpha,a)\right\}_{\beta,b}=\mathcal{C}(\vec{x},t,s;t_w,\alpha,a)_{\beta,b}, \tag{3.39}$$

Following the conventions in Ref. [46] we can project the five-dimensional propagator G onto the four-dimensional walls to construct the four-dimensional propagators L and S for the light and strange quarks. For example, the light quark propagator is constructed as follows:

$$L(\vec{x},t;t_w)_{\beta,b;\alpha,a}=\left\{\frac{1+\gamma^5}{2}G(\vec{x},t,L_s-1;t_w,\alpha,a)\right\}_{\beta,b}+\left\{\frac{1-\gamma^5}{2}G(\vec{x},t,0;t_w,\alpha,a)\right\}_{\beta,b}. \tag{3.40}$$

Critical to this approach is the limited gauge covariance of Eq. 3.39 under general gauge transformations of the underlying gauge configuration. This gauge covariance can be seen by considering a gauge transformation

$$U_\mu(x)\rightarrow U^V_\mu(x)=V(x)U_\mu(x)V(x+\hat{e}_\mu a)^\dagger, \tag{3.41}$$

where $x=(\vec{x},t)$ identifies a four vector and links in the general space-time direction μ are being transformed. The gauge covariance of Eq. 3.39 can be established if we view the Coulomb gauge transformation matrices $V^C[\{U\}](x)$ which appear in the source $\mathcal{C}$ as functionals of the gauge ensemble from which they were defined and observe that candidate Coulomb gauge transformation matrices for the transformed links can be easily constructed from the original Coulomb gauge transformation matrices $V^C[\{U\}]$ as:

$$V^C[\{U^V\}](x)=\mathcal{G}V^C[\{U\}](x)V(x)^\dagger, \tag{3.42}$$

where $\mathcal{G}$ is a 3×3 position-independent, global gauge transformation. If the original matrices $V^C[\{U\}](x)$ transform the configuration $\{U\}$ to Coulomb gauge, then by construction, the new matrices $V^C[\{U^V\}](x)$ will do the same for the gauge-transformed links $\{U^V\}$. Thus, if Eq. 3.42 holds, the left- and right-hand sides of Eq. 3.39 transform similarly under the gauge transformation of Eq. 3.41 (recall that $G(x, s; t_w)$ will also transform as a color vector at x).

However, there are two issues that must be addressed. First the global gauge transformation $\mathcal{G}$ transforms the right-hand indices of the $(V^C)^\dagger$ on the right-hand side of Eq. 3.39 but does not appear on the left-hand side when a gauge transformation is performed. Nevertheless, this lack of invariance under a general gauge transformation can be removed if the propagators $G(\vec{x}, t, s; t_w, \alpha, a)_{\beta,b}$ always appear in products in which the source color indices a are arranged in gauge invariant combinations. Second, the Coulomb gauge transformation for the gauge-transformed configuration can be guaranteed to be given by Eq. 3.42 only if the transformation to Coulomb gauge is unique up to a global gauge transformation, an assumption violated by Gribov copies. Thus, we expect hadronic propagators constructed from these Coulomb gauge fixed wall sources to be affected by gauge noise generated by Gribov copies. However, in practice we find these are excellent sources for creating pseudoscalar mesons providing good statistics from volume averaging and long plateaus when the effective mass of the mesons is examined.

Another important source in this work for fermion loop evaluation is the random Gaussian wall source. The construction of the random Gaussian wall sources is similar and straightforward. As described earlier, a separate random source is generated for each spin-color pair α, a. Thus, a random Gaussian wall source at the time t_w with

spin α and color a is given by the five-dimensional spin-color vector

$$\mathcal{R}(\vec{x},t,s;t_w,\alpha,a)_{b,\beta}=\eta(\vec{x},t)\delta_{t,t_w}\delta_{a,b}\left\{\left(\frac{1-\gamma^5}{2}\right)_{\alpha,\beta}\delta_{s,L_s-1}+\left(\frac{1+\gamma^5}{2}\right)_{\alpha,\beta}\delta_{s,0}\right\}, \tag{3.43}$$

where $\eta(\vec{x},t)$ are independent Gaussian random numbers defined for each space-time point. An independent set of random numbers, $\eta(\vec{x},t)$ is generated for all the twelve separate sources corresponding to the twelve possible choices of spin(α) and color(a). The corresponding propagators G^R and L^R are constructed in a fashion completely analogous to that described above for G, L and S in Eqs. 3.39 and 3.40.

The above discussion summarizes the sources we use in this work. There are other complicated sources such as box source, gaussian source, smeared source, etc. From our experience, they do not have clear advantage over the Coulomb gauge fixed wall source for the pions and kaons, and they are much more difficult to deal with. My recent experiments show that the exponential smearing source may have advantages of reducing the vacuum noise if the all-to-all propagators techniques are used. This will wait for future calculations and experiments. A final comment for the choice of source and sink is that sometimes there are advantages to use different type of operators for the source and sink. For example, the combination of a wall source with a point sink may provide us a better effective mass plateau. Using O_w to stand for a wall source pion, and O_p for a point source, the correlation function becomes

$$\begin{aligned} C(t) &= \langle 0|O_p^\dagger(t)O_w(0)|0\rangle & \text{(3.44a)}\\ &= \sum_n \langle 0|O_p^\dagger(0)|n\rangle\langle n|O_w(0)|0\rangle e^{-E_n t}. & \text{(3.44b)} \end{aligned}$$

If the wall source and point source creates different excited states of pion, the relative contribution from the excited states in the above expression may be much smaller than

both the wall source with wall sink case and the point source with point sink case, and thus give a better effective mass plot, with less contamination from the excited states.

3.4 EigCG Algorithm

In this section, we discuss how to effectively solve the 5D propagators (Eq. 3.39) with many different sources on a single gauge field configuration. The 5D DWF operator D^{DWF} is not positively definite. Our experiences show that solving this equation directly using the Biconjugate Gradient Stabilized (BiCGStab) method does not converge at all. The improved algorithm BiCGStab(L) [47] with sufficiently large L can lead the algorithm to converge, but still very slowly. To our knowledge, the Conjugate Gradient (CG) algorithm works best for a single solve of the DWF operator. We use CG to solve the normal equation,

$$D^{\mathrm{DWF}\dagger} D^{\mathrm{DWF}} G = D^{\mathrm{DWF}\dagger} C. \tag{3.45}$$

Because the DWF operator contains nearest neighbor coupling, we can apply 5D even-odd preconditioning which typically speeds up the calculation by roughly a factor of two. Writing the DWF operator in terms of the even and odd sites,

$$D^{\mathrm{DWF}} = \begin{pmatrix} 1 & D_{eo} \\ D_{oe} & 1 \end{pmatrix}. \tag{3.46}$$

We can apply the Schur decomposition,

$$D^{\mathrm{DWF}} = \begin{pmatrix} 1 & D_{eo} \\ 0 & 1 \end{pmatrix} \begin{pmatrix} 1 - D_{eo} D_{oe} & 0 \\ 0 & 1 \end{pmatrix} \begin{pmatrix} 1 & 0 \\ D_{oe} & 1 \end{pmatrix}. \tag{3.47}$$

Then the equation to be solved becomes half of the original size,

$$M^{\rm pc} x = b'$$

, where the preconditioned domain wall matrix $M^{\rm pc}$ is defined as

$$M^{\rm pc} = 1 - D_{eo} D_{oe}. \tag{3.48}$$

The final normal equation that we solve is

$$M^{\rm pc\dagger} M^{\rm pc} x = M^{\rm pc\dagger} b' \equiv b \tag{3.49}$$

and we use the CG algorithm to solve this normal equation.

As it will become clearer in Section 4.1 and 4.2, we need to solve many propagators for a given configuration because of the disconnected graphs. Roughly speaking, $2T$ light quark propagators are required at least. On a typical T=64 lattice, this is equivalent to 1536 Dirac operator solves. Therefore, a good algorithm to speed up multiple right-hand side solves is crucial for such a calculation to be manageable.

There are two recently published algorithms for the calculation of propagators that could potentially provide a factor of 5-10 speed up. The first is Lüscher's inexact low modes deflation algorithm with the domain-decomposed subspaces that are based on the property called local coherence of the low modes [48]. The second is the EigCG algorithm by Stathopoulos and Orginos [49]. With the inexact low modes deflation method, we obtained a big factor of improvement with a $16^3 \times 32 \times 8$ lattice on a single node machine. However, it is very difficult to implement it efficiently for a highly parallel machine because of the complex structure of the little Dirac operator in the case of DWFs. Because the operator we solve has to be $D^{DWF\dagger} D^{DWF}$, the resulting

little Dirac operator has many hopping terms and it is very inefficient to calculate its inverse. In comparison, the EigCG algorithm only requires a few linear algebra operations and can easily adapt to a massively parallel machine no matter what the operators are. So we used it in our calculation. The disadvantage of the EigCG algorithm compared to Lüscher's is the huge memory requirement. Nevertheless, our current machine has sufficient memory even for the largest lattice we are currently working on, so the need for large memory is not a serious issue.

We follow very closely the original work on EigCG in Ref. [49]. Our goal is to solve Eq. 3.49 fast for a large number of right hand side vectors $\{b_i\}$. The idea is to accumulate low modes in the first few solvings (EigCG algorithm) and using these low modes to speed up later solves (incremental EigCG algorithm). The EigCG algorithm adds the functionality of low modes acuumulation to the CG algorithm, so it requires some extra cost if this functionality is turned on. Once the desired number of low modes are obtained, this part will be turned off. The incremental EigCG algorithm accumulates many low modes during each of the first few CG solves. For each new solve with a new right hand side vector, it first projects out this low mode space that the EigCG algorithm already accumulated and then apply the EigCG algorithm which converges rapidly. The projection is achived by constructing an initial solution (For convenience, define $A = M^{pc\dagger}M^{pc}$.)

$$x_0 = U(U^\dagger AU)^{-1}U^\dagger b, \tag{3.50}$$

where U projects onto the low mode space spanned by the low mode vectors. A typical convergence behavior with the incremental EigCG method is shown in Figure 4. The first EigCG solving converges at the same speed as the normal CG algorithm since there is no low modes vectors yet. The second solving becomes a little bit faster

because of the initial projection of the low modes that we already accumulated during the first solving. Gradually, the new solvings become faster and faster with more and more low modes available. Finally, when the desired number of low modes is obtained, we will stop accumulating low modes and simply do projections to speed up the calculation.

However, Fig. 4 shows a clear turning point (around $res \sim 10^{-6}$) on the convergence curve for the sped-up solves. It dramatically slows down to the normal CG speed at some point. This is because of the inaccuracy of the low modes we obtained from each CG solving. Typically, we try to obtain roughly 16 low modes from each solve and throw away a few with eigenvalue larger than a specified threshold. It is therefore impossible to get all these 16 low modes very accurately. The strategy to avoid the critical slow down arsing from the inaccuracy of the low modes is to do multiple projections by restarting the CG algorithm using the true residual of the previous inversion attempt as the new right hand side, therefore we achieve further speed-up. Following an initial projection as shown in Eq.3.50, we do a few more projections in the middle of the solving process. For example, suppose that after n iterations the relative residual reduces to 10^{-5}, with solution x_n and residual $r_n = b - Ax_n$, we can restart the CG with initial solution $x'_0 = U(U^\dagger AU)^{-1}U^\dagger r_n$ on the equation $Ax' = r_n$, and the total solution is $x_n + x'$. As shown in Fig.4, the relative residual goes straight down once a restart point at 10^{-5} is introduced.

There are two things worth noticing. First, during the low mode accumulation stage, we prefer not to do multiple restarts since it may affect the efficiency of the low modes accumulation. This is the reason that there are turning points in the first 60 convergence curves (except the one goes straight down in 1500 iterations)

in Fig. 4. Second, if the low modes are extremely inaccurate, we have to do many projections by restarting the CG algorithm. In the worst case, we may need to do one projection after each CG step. Then we could better incorporate the projection operator in the original operator to perform a so-called oblique projection as Luscher's algorithm does [48]. On the other hand, for each restart of the CG, we lose all previous information about the direction vectors of the CG algorithm (which is the advantage of the CG to the steepest descent algorithm), so it leads to a decrease in efficiency of the CG algorithm. Therefore, it is better to do fewer restarts, only when it is necessary.

We have shown in Fig.4 that we could successfully apply EigCG to a $32^3 \times 64 \times 32$ lattice, and gain a factor of 7 speedup. The number of low modes we accumulate, the required memory to achieve this, and the comparison of the number of iterations to the original CG is summarized in Tab.3. Notice that to reduce the memory requirement, we used single precision to store the low modes. It has no negative effect on the EigCG algorithm since the low modes we obtained were not very accurate anyway. The largest lattice we tested ($32^3 \times 64 \times 32$) requires 2 Tera bytes of memory, and the code runs efficiently on a 4k BGL nodes machine, which provides 4 Tera bytes memory.

The EigCG algorithm has an amazing characteristic that it is almost mass independent. Figure 5 shows a comparison of different quark mass calculation using EigCG on the $16^3 \times 32 \times 16$ lattice. The number of iterations of normal CG grows quickly as one reduces the quark mass. With EigCG, however, the number of iteration is almost independent of mass after a few initial solves. Therefore, in our $K \to \pi\pi$ calculation, the cost for the light quark mass is reduced to the same as the cost of

strange quark.

3.5 Data Analysis

Once we have calculated the correlation functions like $C(t)$ for the pion from N configurations, we usually have to fit it to some specific function form $f(t,\theta)$ as in Eq. 3.21. This is accomplished by minimizing the correlated χ^2,

$$\chi^2 = \sum_{t,t'}[f(t,\theta) - \overline{C(t)}]V^{-1}(t,t')[f(t',\theta) - \overline{C(t')}], \tag{3.51}$$

where $V(t,t')$ is the covariance matrix for C(t),

$$V(t,t') = \frac{1}{N(N-1)}\sum_{i=1}^{N}(C^i(t) - \overline{C(t)})(C^i(t') - \overline{C(t')}). \tag{3.52}$$

An acceptable fit should have χ^2 per degree of freedom around 1. A too large value means that the fitted model is wrong (e.g. excited state contamination in the pion case if we fit a single exponential starting from t=1). A too small value indicates that the measured errors are overestimated. We use the Levenberg-Marquardt (chapter 15 of Ref. [50]) method to minimize χ^2.

If the data are strongly correlated, it is usually better to use this correlated fit which may give a more accurate result and a clear meaning for the χ^2. For example, our earlier work for the η and $\eta\prime$ mass calculation [12] shows much smaller error bar with the correlated fit than the uncorrelated fit. However, for simplicity, we just use the uncorrelated fit for the simple exponential or cosh fits for the pions and kaons since it usually gives equally good results (especially for small data sets)

$$\chi^2 = \sum_{t}[\frac{f(t,\theta) - \overline{C(t)}}{\sigma(t)}]^2, \tag{3.53}$$

where $\sigma^2(t) = \sum_{i=1}^{N}(C^i(t) - \overline{C(t)})^2/N$.

The correlated or uncorrelated fit gives us the central value only. There are two common ways to calculate the error on the fitted values (for complicated data fitting process): bootstrap and jackknife method. They are very similar methods. Let $C_i(t)$ to stand for the correlation function we calculated from the configuration number i, and we have a sample of N configurations $S = \{C_i(t), i = 1 \ldots N\}$. Based on the correlated fit or uncorrelated fit from the previous discussion, we can compute the parameter θ. Let us label it as $\theta = g(S)$.

The bootstrap method of estimating the standard deviation of the fitted parameter θ works as follow:

1. Draw B independent bootstrap samples S_1^*, S_2^*, ..., S_B^*. A bootstrap sample is obtained by randomly drawing N items with replacement from S. Notice that for such a sample, only approximately 63.2% of the original samples shows up, and 36.8%[1] does not.

2. For each bootstrap sample, fit the parameter θ and get the value $\theta_i = g(S_i^*)$, $i = 1, \ldots, B$.

3. Compute the average and standard deviation of θ_i.

The standard deviation of θ_i estimated from B bootstrap samples is then used as an estimator of the error on θ.

The jackknife method is very similar:

[1]The probability that one specific sample is not drawn is $(1 - 1/N)^N$. For large N, it is approximately $1/e \approx 0.368$.

1. Get N samples from S by leaving one out a time: S_{-i}, for i=1, ..., N.

2. For each sample, fit the parameter θ and get the value $\theta_i = g(S_{-i})$.

3. Compute the average of θ_i: $\overline{\theta}$. The error on θ is estimated as

$$\sigma_J^2 = \frac{N-1}{N} \sum_{i=1}^{N} (\theta_i - \overline{\theta})^2. \tag{3.54}$$

Both methods should give very similar results. If N is large, using a relatively small B may reduce the number of fits. Since the number of configurations in our work is not very big, we use jackknife method to estimate errors, primarily because of its simplicity.

Chapter 4

Kaon Decay from Lattice QCD

In Chapter 2 we have reviewed the standard model and the effective Hamiltonian for kaon to two pions decays. In the previous chapter, the basic lattice QCD techniques were discussed. We now combine all things together, and discuss details how to calculate the decay amplitudes using lattice QCD techniques in this chapter. Specifically, starting from the effective Hamiltonian of Eq. 2.57, the decay amplitudes is calculated as

$$A_{2/0} = F\frac{G_F}{\sqrt{2}}V_{ud}V_{us}\sum_{i=1}^{10}\sum_{j=1}^{7}\left[\Big(z_i(\mu)+\tau y_i(\mu)\Big)Z_{ij}^{\text{lat}\to\overline{\text{MS}}}M_j^{\frac{3}{2}/\frac{1}{2},\text{lat}}\right], \tag{4.1}$$

where the factor F is to correct the finite volume effect (Section 4.3), $Z_{ij}^{\text{lat}\to\overline{\text{MS}}}$ is the renormalization matrix (Section 4.5) to convert the weak matrix elements $M_j^{\frac{3}{2}/\frac{1}{2},\text{lat}}$, (Section 4.2) calculated with lattice regularization to the $\overline{\text{MS}}$ scheme. In the following sections, we will explain in detail each building block of this equation. In addition to the topics identified abouve, we will also present the $\pi-\pi$ scattering calculation that is useful for the normalization of $\pi-\pi$ state and the finite volume correction in kaon decays (Section 4.1), and the calculation of Wilson coefficients (Section 4.4).

4.1 $\pi - \pi$ Scattering

Assuming isospin symmetry, the two pion can have isospin 2, 1, or 0 eigenstates. We use label $|II_z\rangle$ to label isospin eigenstates with isospin I and the z component I_z. The isospin eigenstates expressed in terms of the $\pi\pi$ states are (assuming that the pion labeled first carries momentum $\vec{p}_1$, and the second one carries momentum $\vec{p}_2$) :

$I = 2$:

$$\begin{aligned} |22\rangle =& \left|\pi^+\right\rangle \left|\pi^+\right\rangle, \\ |21\rangle =& \frac{1}{\sqrt{2}}(\left|\pi^+\right\rangle \left|\pi^0\right\rangle + \left|\pi^0\right\rangle \left|\pi^+\right\rangle), \\ |20\rangle =& \frac{1}{\sqrt{6}}(\left|\pi^+\right\rangle \left|\pi^-\right\rangle + 2\left|\pi^0\right\rangle \left|\pi^0\right\rangle + \left|\pi^-\right\rangle \left|\pi^+\right\rangle), \\ & \ldots \end{aligned} \tag{4.2}$$

$I = 1$:

$$\begin{aligned} |11\rangle =& \frac{1}{\sqrt{2}}(\left|\pi^+\right\rangle \left|\pi^0\right\rangle - \left|\pi^0\right\rangle \left|\pi^+\right\rangle), \\ |10\rangle =& \frac{1}{\sqrt{2}}(\left|\pi^+\right\rangle \left|\pi^-\right\rangle - \left|\pi^-\right\rangle \left|\pi^+\right\rangle), \\ & \ldots \end{aligned} \tag{4.3}$$

$I = 0$:

$$|00\rangle = \frac{1}{\sqrt{3}}(\left|\pi^+\right\rangle \left|\pi^-\right\rangle - \left|\pi^0\right\rangle \left|\pi^0\right\rangle + \left|\pi^-\right\rangle \left|\pi^+\right\rangle). \tag{4.4}$$

Let us work out the details of the zero momentum case here. Extension to the case with momentum is straightforward. Bosonic symmetry forbids the $I = 1$ states, so we only consider the $I = 2$ and $I = 0$ states. Similar to the calculation of the pion

mass, we can compute the $\pi - \pi$ energy by computing all possible contractions. The correlation function for $I = 2$ and $I = 0$ eigenstates are

$$\left\langle O_2^{\pi\pi}(t+t')^\dagger O_2^{\pi\pi}(t')\right\rangle = 2\big(D(t) - C(t)\big), \tag{4.5}$$

$$\left\langle O_0^{\pi\pi}(t+t')^\dagger O_0^{\pi\pi}(t')\right\rangle = 2D(t) + C(t) - 6R(t) + 3V(t). \tag{4.6}$$

Here the operator $O_I^{\pi\pi}(t)$ creates a two-pion state with total isospin I (it does not matter what the z-component of isospin I_z is) using two quark and two anti-quark wall-sources located at the time-slice t. The definition for the Direct (D), Cross (C), Rectangular (R), and Vacuum (V) graphs are shown in Fig.6. For convenience, the minus sign arising from the number of fermion loops is not included in the definition of these graphs but instead is introduced in Eqs. 4.5 and 4.6. Each of these graphs represents a contraction. The interpretation is straightforward: simply follow the backward direction of the propagators and write down each propagator, with the big dark point representing a γ_5 matrix for the pseudoscalar. For each loop, we need to take a trace over the spin-color matrix. The vacuum contraction $V(t)$ should be accompanied by a vacuum subtraction. These contractions can be calculated in terms of the light quark propagator $L(t_{\rm snk}, t_{\rm src})$ for a Coulomb gauge fixed wall source located at the time $t_{\rm src}$ and a similar wall sink located at $t_{\rm snk}$. The resulting amplitude for each of these contractions, including the vacuum subtraction for the vacuum graph, is given by

$$D(t) = \frac{1}{T}\sum_{t'=0}^{T-1}\Big\{\Big\langle {\rm tr}[L(t+t',t')L(t+t',t')^\dagger]{\rm tr}[L(t+t',t')L(t+t',t')^\dagger]\Big\rangle\Big\}, \tag{4.7a}$$

$$C(t) = \frac{1}{T}\sum_{t'=0}^{T-1}\Big\{\Big\langle {\rm tr}[L(t+t',t')L(t+t',t')^\dagger L(t+t',t')L(t+t',t')^\dagger]\Big\rangle\Big\}, \tag{4.7b}$$

$$R(t) = \frac{1}{T}\sum_{t'=0}^{T-1}\Big\{\Big\langle {\rm tr}[L(t',t')L(t',t+t')^\dagger L(t+t',t+t')L(t+t',t')^\dagger]\Big\rangle\Big\}, \tag{4.7c}$$

$$V(t) = \frac{1}{T}\sum_{t'=0}^{T-1}\Big\{\Big\langle \mathrm{tr}[L(t',t')L(t',t')^\dagger]\mathrm{tr}[L(t+t',t+t')L(t+t',t+t')^\dagger]\Big\rangle - \Big\langle \mathrm{tr}[L(t',t')L(t',t')^\dagger]\Big\rangle\Big\langle \mathrm{tr}[L(t+t',t+t')L(t+t',t+t')^\dagger]\Big\rangle\Big\} \quad (4.7d)$$

where the indicated traces are taken over spin and color, the hermiticity properties of the domain wall propagator have been used to eliminate factors of γ^5 and we are explicitly combining the results from each of the T time slices.

Once these correlation functions are calculated, Eq. 4.5 and 4.6 give us the combinations providing the complete $I = 2$ and $I = 0$ correlation functions, which are fit with the following functional form,

$$\frac{1}{T}\sum_{t'=0}^{T-1}\langle O^{\pi\pi}(t+t')O^{\pi\pi}(t')\rangle = N_{\pi\pi}^2\left(e^{-E_{\pi\pi}t} + e^{-E_{\pi\pi}(T-t)} + C\right). \quad (4.8)$$

The constant C arises when the two pions join the source at t' and sink at $t+t'$ by traveling in opposite time directions. From the fit, we obtain the $I = 2$ and $I = 0$ energies in a box. If the two-pion interaction is attractive which is the case for $I = 0$ state, the energy will become lower than twice the pion mass. On the contrary if the interaction is repulsive which is the case for $I = 2$ state, the energy will be higher. In Chapter 5 and 6, we will show numerical results to confirm both arguments. The resulting $\pi - \pi$ state normalization coefficient $N_{\pi\pi}$ will also be needed in the following $K \to \pi\pi$ calculations.

The energy shift of two pions in a box tells us more information than the sign of the interaction. Lüscher showed that the energy spectrum of two-particle states in a finite box with periodic boundary conditions and size L directly connects to the scattering phase shift $\delta(p)$ [51]. Below the inelastic threshold $E < 4m_\pi$, and assuming that the scattering phases $\delta_l(p)$ with $l = 4, 6, \ldots$ are negligible, the formula for the

phase shift is simplified and described by

$$\delta(p) = n\pi - \phi(q), q = pL/2\pi, \tag{4.9}$$

where the momentum p is determined from the energy of the two pions

$$E_{\pi\pi} = 2\sqrt{m_\pi^2 + p^2}, \tag{4.10}$$

the value of n equals 0 in our setup which results in a small value of p. The function $\phi(q)$ is defined by

$$\tan\phi(q) = -\frac{q\pi^{3/2}}{Z_{00}(1;q^2)}, \tag{4.11}$$

$$Z_{00}(1;q^2) = \frac{1}{\sqrt{4\pi}}\sum_{n\in\mathbb{Z}^3}\frac{1}{n^2-q^2}. \tag{4.12}$$

For the evaluation of the Z_{00} function, a direct sum fails to converge. We follow the method proposed in the appendix A of Ref. [52].

Once the phase shift $\delta(p)$ is obtained at a few specific momentum p by changing the box size L, the scattering length can be determined from

$$a = \lim_{p\to 0}\frac{\delta(p)}{p}. \tag{4.13}$$

With a sufficiently large box size, the energy shift is small so p is also small (if the pions do not explicitly carry a momentum such as $2\pi/L$). We can then obtain the scattering length approximately from a single calculation $a = \delta(p)/p$. Pluging into the formula for δ, we can approximately compute the scattering length from [53]

$$\begin{aligned} E_{\pi\pi} =& 2m_\pi - \frac{4\pi a}{m_\pi L^3}\{1 + c_1\frac{a}{L} + c_2(\frac{a}{L})^2\} + O(L^{-6}), \\ c_1 =& -2.837297, \quad c_2 = 6.375182. \end{aligned} \tag{4.14}$$

Notice that even though the phase shift itself is meaningless for negative p^2 as in the case of the attractive $I = 0$ two-pion channel, the expression for the scattering length in Eq. 4.13 and 4.14 is still correct.

Simple Arguments for Lüshcer's Formula

A direct proof of Lüscher's Formula [51] is very complicated. To understand how the formula comes about, we give a proof for some very simple cases here. First let us work on a one dimensional model with two identical particles interacting though a δ potential $V(x) = V_0\delta(x)$. In infinite space, the scattering phase shift with incoming waves with wave number k and $-k$ can be easily calculated by solving the Schrödinger equation:

$$\delta(k) = -\arctan(\frac{mV_0}{4k}). \tag{4.15}$$

Now let us put the two particles in a one-dimensional box of size L, which obeys periodic boundary conditions. Solving the Schrödinger equation eigenvalue problem, we get the quantization condition for the energy of the two particles $E = 2\sqrt{m^2 + \hat{k}^2}$, with $\hat{k}$ satisfying

$$\frac{mV_0}{4\hat{k}} = \tan(\hat{k}L). \tag{4.16}$$

In a lattice calculation, we can only determine the quantized energy E of the two particles or the quantized momentum (wave number) $\hat{k}$. Plug Eq. 4.16 into Eq. 4.15, we get the phase shift formula at these specific momentums,

$$\begin{aligned} \delta(\hat{k}) &= -\arctan(\frac{mV_0}{4\hat{k}}) = -\arctan(\tan\hat{k}L) \\ &= -\hat{k}L + n\pi. \end{aligned} \tag{4.17}$$

With a definition of the function $\phi(q) = 2q\pi$, we recover Lüscher's formula of Eq. 4.9. The above equation tells us the phase shift at the quantized momentum $\hat{k}$. In 3 dimensions, the only difference is that the $\phi(q)$ function is much more complicated.

Another simplified problem for studying two particles in a box is to consider a sphere instead of a box. The solution to the 3 dimensional infinite space scattering problem is

$$A_l(r) = e^{i\delta_l}[\cos\delta_l j_l(2kr) - \sin\delta_l n_l(2kr)], \tag{4.18}$$

where the subindex l stands for the angular momentum number. The function $j_l(x)$ and $n_l(x)$ are the first kind and second kind of the spherical Bessel functions. Ignore all high angular momentum terms with $l > 0$, and assume periodic boundary conditions on the sphere with radius R, then we require

$$\left.\frac{dA_0(r)}{dr}\right|_{r=R} = 0, \tag{4.19}$$

which gives us the formula for the phase shift at the quantized momentum $\hat{k}$,

$$\tan\delta_0 = \frac{2\hat{k}R\cos(2\hat{k}R) - \sin(2\hat{k}R)}{2\hat{k}R\sin(2\hat{k}R) + \cos(2\hat{k}R)} \equiv -\tan\phi(q). \tag{4.20}$$

Again, this case has a much simpler function $\phi(q)$. One interesting observation from this simplified model is that, for very small k (large R), the shape of the boundary does not matter very much, so Eq. 4.20 could give results similar to the results of Eq. 4.9 with a box shape. Let the volume of the sphere and the box be the same, $4\pi R^3/3 = L^3$, which gives $R = \sqrt[3]{3/4\pi}L$. The calculated phase shift from both equations agree very well for small k as shown in Fig.7.

Numerical Check of Lüscher's Formula

In writing down the scatting phase shift formula in Eq. 4.9, we used the approximation that high angular momentum terms do not contribute. In this subsection, we test

how well this approximate formula performs for two non-relativistic particles in a box of size that is typical to lattice simulations.

Suppose that the two particles (with mass m_N) interact through the Yukawa interaction,

$$V(r) = g\frac{e^{-m_\pi r}}{r}, \tag{4.21}$$

and their behavior is governed by the Schrödinger equation

$$[-\frac{\nabla^2}{2\mu} + V(r)]\phi(r) = E\phi(r), \tag{4.22}$$

where $\mu = m_N/2$ is the reduced mass. Putting the two particles in box of size L with periodic boundary conditions, we solve the Schrödinger equation numerically, and study the energy shift as a function of the interaction strength g and the box size L. Figure 8 shows the calculated results. Notice that theoretically, for $g < -2.7$, bound state exists. This is reflected in our results for $g = -3.0$ and $g = -3.5$: the energy shift becomes flat as we continue increasing the box size. For other g, it looks like the energy shift converges to zero as the box size increases, which also agrees with our expectation.

From the energy shift, we can calculate the phase shift using Lüscher's formula 4.9. We also calculated the phase shift in the infinite volume scattering, using the Born approximation, both to first and second order based on the following formula:

$$\delta_1 = -\frac{m_N g}{4p}\ln(1+\frac{4p^2}{m_\pi^2}), \tag{4.23}$$

$$\delta_2 = \delta_1 + \frac{2m_N^2 g^2}{p^2}\int_0^\infty dy \frac{\sin(2y)}{2y} e^{-m_\pi y/p}\int_0^y dx \frac{\sin^2 x}{x} e^{-m_\pi x/p}. \tag{4.24}$$

The calculated results are summarized in Tab. 5, and Fig. 9 shows the comparison of the two different methods. We can see that Eq. 4.9 gives a very good approximation

for relatively large box. Since $1/m_\pi$ represents the interaction range, we want to have $L/(1/m_\pi) = m_\pi L$ be large for the best approximation.

4.2 Weak Matrix Elements and Contractions

The most difficult and important part of this work is to calculate the weak matrix elements $M_j^{\frac{3}{2}/\frac{1}{2},\mathrm{lat}}$ on the lattice. In this section, we will enumerate all contractions that contribute and explain in detail how the weak matrix elements are calculated.

We list all of the possible contractions contributing to the matrix elements $\langle\pi\pi|Q_i|K^0\rangle$ in Figs. 10-13. There are 48 different contractions which are labeled by circled numbers ranging from 1 to 48, and grouped into four categories labeled as *type*1, *type*2, *type*3, and *type*4 according to their topology. Once we have calculated all of these contractions, the correlation functions $\langle O_I^{\pi\pi}(t_\pi)Q_i(t_{\mathrm{op}})K^0(t_K)\rangle$ are then obtained as combinations of these contractions. In order to simplify the following formulae, we use the amplitude $A_{I,i}(t_\pi, t, t_K)$ to represent three point function $\langle O_I^{\pi\pi}(t_\pi)Q_i(t_{\mathrm{op}})K(t_K)\rangle$. Using this notation, the $I = 2$ amplitudes can be written,

$$A_{2,1}(t_\pi, t_{\mathrm{op}}, t_K) = i\sqrt{\frac{2}{3}}\{① - ⑤\} \tag{4.25a}$$

$$A_{2,2}(t_\pi, t_{\mathrm{op}}, t_K) = i\sqrt{\frac{2}{3}}\{② - ⑥\} \tag{4.25b}$$

$$A_{2,3}(t_\pi, t_{\mathrm{op}}, t_K) = 0 \tag{4.25c}$$

$$A_{2,4}(t_\pi, t_{\mathrm{op}}, t_K) = 0 \tag{4.25d}$$

$$A_{2,5}(t_\pi, t_{\mathrm{op}}, t_K) = 0 \tag{4.25e}$$

$$A_{2,6}(t_\pi, t_{\mathrm{op}}, t_K) = 0 \tag{4.25f}$$

$$A_{2,7}(t_\pi, t_{\mathrm{op}}, t_K) = i\sqrt{\frac{3}{2}}\{③ - ⑦\} \tag{4.25g}$$

$$A_{2,8}(t_\pi, t_{\rm op}, t_K) = i\sqrt{\frac{3}{2}}\{④ - ⑧\} \tag{4.25h}$$

$$A_{2,9}(t_\pi, t_{\rm op}, t_K) = i\sqrt{\frac{3}{2}}\{① - ⑤\} \tag{4.25i}$$

$$A_{2,10}(t_\pi, t_{\rm op}, t_K) = i\sqrt{\frac{3}{2}}\{② - ⑥\} \tag{4.25j}$$

and in the I=0 case,

$$A_{0,1}(t_\pi, t_{\rm op}, t_K) = i\frac{1}{\sqrt{3}}\{-① - 2\cdot⑤ + 3\cdot⑨ + 3\cdot⑰ - 3\cdot㉝\} \tag{4.26a}$$

$$A_{0,2}(t_\pi, t_{\rm op}, t_K) = i\frac{1}{\sqrt{3}}\{-② - 2\cdot⑥ + 3\cdot⑩ + 3\cdot⑱ - 3\cdot㉞\} \tag{4.26b}$$

$$\begin{aligned} A_{0,3}(t_\pi, t_{\rm op}, t_K) = i\sqrt{3}\{&-⑤ + 2\cdot⑨ - ⑬ + 2\cdot⑰ + ㉑ \\ &-㉕ - ㉙ - 2\cdot㉝ - ㊲ + ㊶ + ㊺\} \end{aligned} \tag{4.26c}$$

$$\begin{aligned} A_{0,4}(t_\pi, t_{\rm op}, t_K) = i\sqrt{3}\{&-⑥ + 2\cdot⑩ - ⑭ + 2\cdot⑱ + ㉒ \\ &-㉖ - ㉚ - 2\cdot㉞ - ㊳ + ㊷ + ㊻\} \end{aligned} \tag{4.26d}$$

$$\begin{aligned} A_{0,5}(t_\pi, t_{\rm op}, t_K) = i\sqrt{3}\{&-⑦ + 2\cdot⑪ - ⑮ + 2\cdot⑲ + ㉓ \\ &-㉗ - ㉛ - 2\cdot㉟ - ㊴ + ㊸ + ㊼\} \end{aligned} \tag{4.26e}$$

$$\begin{aligned} A_{0,6}(t_\pi, t_{\rm op}, t_K) = i\sqrt{3}\{&-⑧ + 2\cdot⑫ - ⑯ + 2\cdot⑳ + ㉔ \\ &-㉘ - ㉜ - 2\cdot㊱ - ㊵ + ㊹ + ㊽\} \end{aligned} \tag{4.26f}$$

$$\begin{aligned} A_{0,7}(t_\pi, t_{\rm op}, t_K) = i\frac{\sqrt{3}}{2}\{&-③ - ⑦ + ⑪ + ⑮ + ⑲ \\ &-㉓ + ㉗ + ㉛ - ㉟ + ㊴ - ㊸ - ㊼\} \end{aligned} \tag{4.26g}$$

$$\begin{aligned} A_{0,8}(t_\pi, t_{\rm op}, t_K) = i\frac{\sqrt{3}}{2}\{&-④ - ⑧ + ⑫ + ⑯ + ⑳ \\ &-㉔ + ㉘ + ㉜ - ㊱ + ㊵ - ㊹ - ㊽\} \end{aligned} \tag{4.26h}$$

$$\begin{aligned} A_{0,9}(t_\pi, t_{\rm op}, t_K) = i\frac{\sqrt{3}}{2}\{&-① - ⑤ + ⑨ + ⑬ + ⑰ \\ &-㉑ + ㉕ + ㉙ - ㉝ + ㊲ - ㊶ - ㊺\} \end{aligned} \tag{4.26i}$$

$$A_{0,10}(t_\pi, t_{\rm op}, t_K) = i\frac{\sqrt{3}}{2}\{-\textcircled{2} - \textcircled{6} + \textcircled{10} + \textcircled{14} + \textcircled{18} \\ -\textcircled{22} + \textcircled{26} + \textcircled{30} - \textcircled{34} + \textcircled{38} - \textcircled{42} - \textcircled{46}\}, \tag{4.26j}$$

where the factor i comes from our definition of the interpolation operator for the mesons, *e.g.* $K^0 = i(\overline{d}\gamma_5 s)$.

A few notes about the contractions shown in the Figs. 10 - 13 may be useful:

1. The contractions identified by circled numbers do not carry the minus sign required when there is an odd number of fermion loops. Instead, the signs are included explicitly in Eqs. 4.25 and 4.26.

2. The routing of the solid line indicates spin contraction while that of the dashed line indicates the contraction of color indices. If there is no dashed line, then solid line indicates connections implied by the trace over both color and spin indices. (This will be explained in more detail below.)

3. A line represents a light quark propagator if it is not explicitly labeled with 's'. Up and down quarks and particular flavors of pion are not distinguished in Figs. 10 - 13. Instead these specific contractions of strange and light quark propagators are combined in Eqs. 4.25 and 4.26 to give the $I = 2$ and $I = 0$ amplitudes directly.

4. Using Fierz symmetry:

$$[\gamma^\mu(1-\gamma_5)]_{\alpha\beta}[\gamma_\mu(1-\gamma_5)]_{\gamma\delta} = -[\gamma^\mu(1-\gamma_5)]_{\alpha\delta}[\gamma_\mu(1-\gamma_5)]_{\gamma\beta}, \tag{4.27}$$

it can be shown that there are 12 identities among these contractions:

$$⑥ = -①, \quad ⑤ = -②, \quad ⑭ = -⑨, \quad ⑬ = -⑩, \tag{4.28a}$$

$$㉖ = -⑰, \quad ㉕ = -⑱, \quad ㉙ = -㉒, \quad ㉚ = -㉑, \tag{4.28b}$$

$$㊷ = -㉝, \quad ㊶ = -㉞, \quad ㊺ = -㊳, \quad ㊻ = -㊲. \tag{4.28c}$$

A consequence of these identities is that Eq. 4.26 is consistent with only seven of the ten operators Q_i being linearly independent and with the three usual relations shown in Eq. 2.59.

5. Based on charge conjugation symmetry and γ^5 hermiticity, the gauge field average of each of these contractions is real.

6. The loop contractions of *type*3 and *type*4 are calculated using the Gaussian, stochastic wall sources described in Sec. 3.3.

In order to make our approach more explicit, we will discuss some examples. First consider the two contractions of *type*1 identified as ① and ② and shown in the top half of Fig. 10:

$$\begin{aligned} ① \;=\; & \mathrm{Tr}\Big\{\gamma_\mu(1-\gamma_5)L(x_{op},t_\pi)L(x_{op},t_\pi)^\dagger\Big\} \\ & \cdot\mathrm{Tr}\Big\{\gamma^\mu(1-\gamma_5)L(x_{op},t_\pi)\gamma^5\left[\sum_{\vec{x}_\pi}L((\vec{x}_\pi,t_\pi),t_K)\right]S(x_{op},t_K)^\dagger\Big\} \end{aligned} \tag{4.29}$$

$$\begin{aligned} ② \;=\; & \mathrm{Tr}_c\Bigg\{\mathrm{Tr}_s\Big\{\gamma_\mu(1-\gamma_5)L(x_{op},t_\pi)L(x_{op},t_\pi)^\dagger\Big\} \\ & \cdot\mathrm{Tr}_s\Big\{\gamma^\mu(1-\gamma_5)L(x_{op},t_\pi)\gamma_5\left[\sum_{\vec{x}_\pi}L((\vec{x}_\pi,t_\pi),t_K)\right]S(x_{op},t_K)^\dagger\Big\}\Bigg\}, \end{aligned} \tag{4.30}$$

where t_K is the time of the kaon wall source, t_π the time at which the two pions are absorbed and $x_{op} = (\vec{x}_{op}, t_{op})$ the location of the weak operator. The func-

tion $L(x_{\rm sink}, t_{\rm src})$ is the light quark propagator, a 12×12 spin-color matrix, while $S(x_{\rm sink}, t_{\rm src})$ is the strange quark propagator. The hermitian conjugation operation, $\dagger$, operates on these 12×12 matrices. We use Tr_c to indicate a color trace, Tr_s a spin trace, and Tr, with no subscript, stands for both a spin and color trace. We have also used the γ^5 hermiticity of the quark propagators to realize the combination of quark propagators given in Eqs. 4.29 and 4.30, allowing both contractions to be constructed from light and strange propagators computed using Coulomb gauge fixed wall sources located only at the times t_π and t_K. Note the sum over the spatial components of the sink $\vec{x}_\pi$ creates a symmetrical wall sink provided that the appropriate Coulomb gauge transformation matrix has been applied to the sink color index of this propagator to duplicate the Coulomb gauge transformation that was used to create the Coulomb gauge fixed wall source. We will sum over the spatial location, $\vec{x}_{op}$, of the weak operator, to project onto zero spatial momentum and improve statistics. In Chapter 5 and 6, we will show results as a function of the separations between t_π, $t_{\rm op}$ and t_K.

As a third example, which illustrates the use of random wall sources, consider contraction ⑲ shown in Fig. 12. Using the notation introduced above, this contraction is given by

$$\begin{aligned} ⑲ \;=\; & \mathrm{Tr}\Big\{\gamma_\mu(1+\gamma_5)L^R(x_{\rm op},t_{\rm op})\Big\}\eta(x_{\rm op})^* \cdot \mathrm{Tr}\Big\{\gamma^\mu(1-\gamma_5)L(x_{\rm op},t_\pi) \\ & \left[\sum_{\vec{x}'_\pi} L\Big((\vec{x}'_\pi,t_\pi),t_\pi\Big)^\dagger\right]\left[\sum_{\vec{x}_\pi} L\Big((\vec{x}_\pi,t_\pi),t_K\Big)\right] S(x_{\rm op},t_K)^\dagger\Big\}. \end{aligned} \tag{4.31}$$

Here $\eta(x)$ is the value of the complex, Gaussian random wall source at the space-time position x, while $L^R(x_{\rm sink}, t_{\rm src})$ is the propagator whose source is $\eta(x)\delta(x_0 - t_{\rm src})$. The Dirac delta function $\delta(x_0 - t_{\rm src})$ restricts the source to the time plane $t = t_{\rm src}$. In the usual way, the average over the random source $\eta(\vec{x})$ which accompanies the

configuration average, will set to zero all terms in which the source and sink positions for the propagator $L^R(x_{\rm op}, t_{\rm op})$ in Eq. 4.31 differ, giving us the contraction implied by the closed loop in the top left panel of Fig. 12. By using 32 separate propagators each with a random source non-zero on only one of our 32 time slices we obtain more statistically accurate results than would result from a single random source spread over all times.

An important objective of this calculation is to learn how to accurately evaluate the quark loop integration that is present in *type*3 and *type*4 graphs and which contains a $1/a^2$, quadratically divergent component. As it can be recognized from the structure of the diagrams, these divergent terms can be interpreted as arising from the mixing between the dimension-six operators Q_i and a dimension-3 "mass" operator of the form $\overline{s}\gamma_5 d$. Such divergent terms are expected and do not represent a breakdown of the standard effective Hamiltonian written in Eq. 2.57. In fact, given the good chiral symmetry of domain wall fermions all other operators with dimension less than six which might potentially mix with those in Eq. 2.57 will vanish if the equations of motion are imposed. Therefore these operators cannot contribute to the Green's functions evaluated in Eqs. 4.25 and 4.26 where the operators in H_W are separated in space-time from those operators creating the K meson and destroying the π mesons, a circumstance in which the equations of motion can be applied.

The problematic operator $\overline{s}\gamma_5 d$ is not explicitly removed from the effective Hamiltonian because, again using the equations of motion, $\overline{s}\gamma_5 d$ can be written as the divergence of an axial current and hence will vanish in the physical case where the weak operator H_W carries no four-momentum and is evaluated between on-shell states. While we can explicitly sum the effective Hamiltonian density $\mathcal{H}_W$ over space to en-

sure H_W carries no spatial momentum, to ensure that no energy is transferred we must arrange that the kaon mass and two-pion energy are equal. We may achieve this condition, at least approximately, but there will be contributions from heavier states, which are normally exponentially suppressed, but which will violate energy conservation and hence will be enhanced by this divergent $\overline{s}\gamma_5 d$ term.

Since $\overline{s}\gamma_5 d$ will not contribute to the physical, energy-conserving $K \to \pi\pi$ amplitude, there is no theoretical requirement that it be removed. The coefficient of this $\overline{s}\gamma_5 d$ piece is both regulator dependent and irrelevant. The contribution of these terms in a lattice calculation of $K \to \pi\pi$ decay amplitudes will ultimately vanish as the equality of the initial and final energies is made more precise and as increased time separations are achieved. However, the unphysical effects of this $\overline{s}\gamma_5 d$ mixing are much more easily suppressed by reducing the size of this irrelevant term than by dramatically increasing the lattice size and collecting the substantially increased statistics required to work at large time separations.

A direct way to remove this $1/a^2$ enhancement is to explicitly subtract an $\alpha_i \overline{s}\gamma_5 d$ term from each of the relevant operators Q_i where the coefficient α_i can be fixed by imposing the condition:

$$\langle 0|Q_i - \alpha_i \overline{s}\gamma_5 d|K\rangle = 0, \tag{4.32}$$

a condition that is typically required in the chiral perturbation theory for $K \to \pi\pi$ [54]. Of course, this arbitrary condition will leave a finite, regulator-dependent $\overline{s}\gamma_5 d$ piece behind in the subtracted operator $Q_i - \alpha_i \overline{s}\gamma_5 d$. However, this unphysical piece will not contribute to the energy-conserving amplitude being evaluated. Since it is no longer $1/a^2$-enhanced its effects on our calculation will be similar to those of the many other energy non-conserving terms which we must suppress by choosing

equal energy K and $\pi\pi$ states and using sufficient large time separation to suppress the contributions of excited states.

Following Eq. 4.32 we will choose the coefficient α_i from the ratio

$$\alpha_i = \frac{\langle 0|Q_i|K^0\rangle}{\langle 0|\overline{s}\gamma_5 d|K^0\rangle}. \tag{4.33}$$

(Note, with this definition the coefficient α_i is proportional to the difference of the strange and light quark masses.) Thus, we will improve the accuracy when calculating graphs of $type3$ and $type4$ by including an explicit subtraction term for those operators Q_i where mixing with $\overline{s}\gamma_5 d$ is permitted by the symmetries:

$$\left\langle O_0^{\pi\pi}(t_\pi)Q_i(t_{\rm op})K^0(t_K)\right\rangle_{sub} = \left\langle O_0^{\pi\pi}(t_\pi)Q_i(t_{\rm op})K^0(t_K)\right\rangle - \alpha_i \left\langle O_0^{\pi\pi}(t_\pi)\overline{s}\gamma_5 d(t_{\rm op})K^0(t_K)\right\rangle. \tag{4.34}$$

We should recognize that there is a second, divergent, parity-even operator $\overline{s}d$ which mixes with our operators Q_i. However, we choose to neglect this effect because parity symmetry prevents it from contributing to either the $K \to \pi\pi$ or $K \to |0\rangle$ correlation functions being evaluated here.

The amplitude $\langle O_0^{\pi\pi}(t_\pi)\overline{s}\gamma_5 d(t_{\rm op})K^0(t_K)\rangle$ includes two contractions, one connected and one disconnected as shown in Fig. 14. These terms, which arise from the mixing of the operators Q_i with $\overline{s}\gamma_5 d$, are labeled $mix3$ and $mix4$. To better visualize the contributions from different types of contractions, we can write the right hand side of Eq. 4.34 symbolically as

$$\begin{aligned} & type1 + type2 + type3 + type4 - \alpha\cdot(mix3 + mix4) \\ = \;& type1 + type2 + sub3 + sub4, \end{aligned} \tag{4.35}$$

where $sub3 = type3 - \alpha\cdot mix3$ and $sub4 = type4 - \alpha\cdot mix4$. Note, here and in later

discussions we refer to the term being subtracted as "mix" and the final difference as the subtracted amplitude "sub".

The correlation functions we used to evaluate the final weak matrix elements are averaged over all possible positions of sources. For a given kaon-pion separation Δ, we compute $C_{i,j}(\Delta, t)$, for isospin I=0 or 2, and operators i=1, 2, ..., 10,

$$C_{I,i}(\Delta, t) = \frac{1}{T}\sum_{t'=0}^{T-1} A_{I,i}(t_\pi = t' + \Delta, t_{\rm op} = t + t', t_K = t'). \tag{4.36}$$

In the case $0 \ll t \ll \Delta$, the excited states contamination are exponentially suppressed relative to the ground state. We fit the correlators $C_{i,j}(\Delta, t)$ using a single free parameter which is the weak matrix element we want $M_i^{\frac{3}{2}/\frac{1}{2},\rm lat}$:

$$C_{I,i}(\Delta, t) \;\; = \;\; M_i^{\frac{3}{2}/\frac{1}{2},\rm lat} N_{\pi\pi} N_K e^{-E_{\pi\pi}\Delta} e^{-(m_K - E_{\pi\pi})t}, \tag{4.37}$$

where N_K, m_K and $N_{\pi\pi}$, $E_{\pi\pi}$ are determined by fitting the kaon and two-pion correlators 4.8 respectively:

$$\frac{1}{T}\sum_{t'=0}^{T-1} \langle K(t+t')K(t')\rangle = N_K^2 \left(e^{-m_K t} + e^{-m_K(T-t)}\right) \tag{4.38}$$

We will show numerical results for these fittings and the results for the weak matrix elements in Chapter 5 and 6.

4.3 Finite Volume Effects

The weak matrix elements M calculated from correlation functions in Euclidean space have no simple relation to the desired transition matrix elements in Minkowski space. The Maiani-Testa no-go theorem [55] summarized this difficulty. However, with a

finite volume box, because the two particle energy spectrum is far from being continuous, Lellouch and Lüscher discovered that the weak matrix elements calculated in a finite lattice are directly connected to the physical weak matrix element in infinite volume [53].

First, let us turn off the weak interaction. Eq. 4.9 and 4.10 gives us the phase shift $\delta(\hat{p}_\pi)$ at the value of $\hat{p}_\pi$. Now turn on the weak interaction, and assume the kaon and the two-pion state are degenerate. Then degenerate perturbation theory in the first order gives us

$$W = m_K \pm |M|, \tag{4.39}$$

where M is the weak matrix element on the lattice. From equation 4.10, we find

$$\hat{p} = \hat{p}_\pi \pm \Delta p, \quad \Delta p \equiv \frac{m_K}{4\hat{p}_\pi}|M|, \tag{4.40}$$

and Eq. 4.9 tells us the new phase shift $\delta(\hat{p})$, now including the effects of the weak interactions.

Let us calculate $\delta(\hat{p})$ with another method. It has two major contributions: one is from the direct $\pi - \pi$ scattering $\hat{\delta}(p)$ (here we added a hat symbol to our previous expression to indicate this expression only includes the $\pi - \pi$ scattering effect), the other is from the kaon resonance (see. Fig. 2 of Ref. [53]). The contributions from other states are ignored because those energy levels are far off from $E_{\pi\pi}$ in the lattice. The effective coupling vertex for the second term is

$$i\lambda = (-iA^*)\frac{i}{W^2 - m_K^2}(iA) \approx i\frac{|A|^2}{\pm 2m_K|M|}, \tag{4.41}$$

where A is the infinite volume decay amplitude. Given this effective coupling vertex,

the contribution to the phase shift from quantum mechanics scattering formula is

$$-\frac{\lambda\hat{p}}{8\pi W} \approx \mp\frac{\hat{p}_\pi |A|^2}{16\pi m_K^2 |M|}. \tag{4.42}$$

Equate $\delta(\hat{p})$ from these two different methods and simplify it:

$$\begin{aligned}
\delta(\hat{p}) &= \hat{\delta}(\hat{p}_\pi \pm \Delta p) \pm \frac{\hat{p}_\pi |A|^2}{16\pi m_K^2 |M|}, & (4.43)\\
-\phi(\hat{p}_\pi \pm \Delta p) &= -\phi(\hat{p}_\pi) \pm \Delta p \frac{\partial\hat{\delta}(p)}{\partial p}|_{p=\hat{p}_\pi} \mp \frac{\hat{p}_\pi |A|^2}{16\pi m_K^2 |M|}, & (4.44)\\
\mp\Delta q \frac{\partial\phi(q)}{\partial q}|_{q=\hat{q}_\pi} &= \Delta p \frac{\partial\hat{\delta}(p)}{\partial p}|_{p=\hat{p}_\pi} \mp \frac{\hat{p}_\pi |A|^2}{16\pi m_K^2 |M|}, & (4.45)\\
|A|^2 &= 4\pi\{q\frac{\partial\phi(q)}{\partial q} + p\frac{\partial\hat{\delta}(p)}{\partial p}\}|_{p=\hat{p}_\pi} (\frac{m_K}{\hat{p}_\pi})^3 |M|^2. & (4.46)
\end{aligned}$$

The last line is the Lellouch-Lüscher formula. Notice that there is a factor of 2 difference in the formula from the original paper. This is because we use different $\pi - \pi$ state normalization convention, which gives us the experiment value of $\mathrm{Re}(A_2)$ and $\mathrm{Re}(A_0)$ that are shown in Section 2.3.

In summary, the infinite volume amplitude A can be calculated from the $K \to \pi\pi$ matrix element M of the effective weak Hamiltonian of Eq. 2.57 calculated using finite volume states normalized to unity, by multiplying the Lellouch-Lüscher factor (F), $|A|^2 = F^2 M^2$, where

$$F^2 = 4\pi \left(\frac{E_{\pi\pi}^2 m_K}{p^3}\right) \left\{ p\frac{\partial\delta_2(p)}{\partial p} + q\frac{\partial\phi(q)}{\partial q} \right\}\Bigg|_{p=\hat{p}_\pi}. \tag{4.47}$$

We have rewritten this form a little bit so that in the free field limit of non-interacting pions, the factor F becomes $F_{\mathrm{free}}^2 = 2(2m_\pi)^2 m_K L^3$, which agrees with the factor connecting the different normalization of states in a box and plane wave states in infinite volume.

4.4 Wilson Coefficients

Wilson coefficients summarize the effect of short-distance contributions. We calculate them using the renormalization group improved perturbation theory to the next leading order by following exactly the method and techniques of reference [18].

We use the Naive Dimensional Regularization (NDR) for the treatment of γ_5 in D dimensions. The initial values, renormalization-group evolution and anomalous-dimension matrices, and quark threshold matching matrix are all described in section VII/G of [18]. The calculated Wilson coefficients at the renormalization energy scale $\mu = 2.15$ GeV with 3 flavors are listed in Tab.4. All the standard model parameters used in this calculation are from PDG 2010 [7] and summarized in Tab.1.

Notice that to obtain the results in Tab.4, we used the same strategy as in [18]: only the leading order terms are kept, others are thrown away. For example, if we have an expression $(1+a\alpha_s)(1+b\alpha_s)$, we should not do the calculation by computing the two terms numerically in the two parentheses. Instead, the expression is expanded, and only the term $1 + a\alpha_s + b\alpha_s$ is kept and calculated. The initial condition, evolution operator matrix and matching matrix are all functions of α and α_s. We need to keep the analytical form, expand the expressions, and keep the $O(1)$, $O(\alpha_s)$, $O(\alpha)$, and $O(\alpha/\alpha_s)$ term at the end. By following this method, we were able to exactly reproduce the results in [18] (when using the same parameters). This is the advantage of explicitly dropping all higher order terms: others can recognize exactly what kinds of terms are dropped so the results can be easily reproduced exactly.

4.5 Non-perturbative Renormalization

In order to combine our lattice matrix elements with the Wilson coefficients describing the short-distance weak interaction physics responsible for $K \to \pi\pi$ decay we must convert our lattice operators into those normalized according to that $\overline{\text{MS}}$ scheme in which the Wilson coefficients are evaluated. We will discuss the details of this procedure in this section.

The first step is converting the lattice operators into those normalized according to the RI/MOM scheme [16].

$$Q_i^{\text{RI}}(\mu) = \sum_{j=1}^{7} Z_{ij}^{\text{lat}\to\text{RI}}(\mu, a) Q_j'^{lat}(a). \tag{4.48}$$

For the operators with a prime, we follow the procedure of Ref. [54] and make use of the fact that the ten operators which enter the conventional expression given in Eq. 2.57 are linearly dependent and can be reduced to a set of seven independent operators, Q_1', Q_2', Q_3', Q_5', Q_6', Q_7' and Q_8':

$$Q_1'' = Q_1' = 3Q_1 + 2Q_2 - Q_3, \tag{4.49a}$$

$$Q_2'' = Q_2' = \frac{1}{5}(2Q_1 - 2Q_2 + Q_3, \tag{4.49b}$$

$$Q_3'' = Q_3' = \frac{1}{5}(-3Q_1 + 3Q_2 + Q_3), \tag{4.49c}$$

$$Q_4'' = Q_5' = Q_5, \tag{4.49d}$$

$$Q_5'' = Q_6' = Q_6, \tag{4.49e}$$

$$Q_6'' = Q_7' = Q_7, \tag{4.49f}$$

$$Q_7'' = Q_8' = Q_8. \tag{4.49g}$$

These have been defined so that the resulting operators belong to specific irreducible representations of $SU_L(3) \times SU_R(3)$. The operator Q_1' transforms as a $(27, 1)$. The

four operators Q'_2, Q'_3, Q'_5 and Q'_6 all belong to the $(8,1)$ representation, while Q'_7 and Q'_8 each transform as an $(8,8)$. Here (m,n) denotes the product of an m-dimensional irreducible representation of $SU_L(3)$ with an n-dimensional irreducible representation of $SU_R(3)$. We refer to the basis of these seven independent operators as the chiral basis. The introduction of the double prime symbols is just for future convenience. Because $SU_L(3) \times SU_R(3)$ is an exact symmetry of the large momentum, massless limit which our NPR calculation is intended to approximate, the mixing matrix $Z^{\mathrm{lat}\to\mathrm{RI}}$ given in Eq. 4.48 which relates the lattice and RI-normalized operators will be block diagonal, only connecting operators which belong to the same irreducible representation of $SU_L(3) \times SU_R(3)$.

The RI/MOM conditions which define the operators O_i^{RI} and determine the 7×7 matrix $Z^{\mathrm{lat}\to\mathrm{RI}}$ are imposed on the Green's functions:[1]

$$G_i(p_1,p_2)^f_{\alpha\beta\gamma\delta} = \prod_{i=1}^{4}\left\{\int d^4x_i\right\}\left\langle s(x_1)_\alpha f(x_2)_\beta Q_i^{\mathrm{RI}}(0)\overline{d}_\gamma(x_3)\overline{f}_\delta(x_4)\right\rangle e^{-ip_2(x_1+x_2)}e^{ip_1(x_3+x_4)} \tag{4.50}$$

evaluated for $p_1^2 = p_2^2 = (p_1-p_2)^2 = \mu^2$. Here α, β, γ and δ are spin and color indices. The fields $\overline{d}$ and $\overline{f}$ create a down quark and a quark of flavor $f = u$ or d while s and f destroy a strange quark and a quark of flavor f. The RI/MOM conditions are imposed by removing the four external quark propagators from the amplitudes in Eq. 4.50, and then contracting each of the resulting seven amputated Green's functions obtained from Eq. 4.50 with seven projectors $\{\Gamma^{ij;f}_{\alpha\beta\gamma\delta}\}_{1\le j\le 7}$. The matrix $Z^{\mathrm{lat}\to\mathrm{RI}}$ is then determined by requiring that the resulting 49 quantities take

[1]While this equation agrees with Eqs. 143 and 152 of Ref. [54], a different choice of momenta was actually used in that earlier reference. These two equations accurately describe the earlier kinematics only after one pair of the momenta p_1 and p_2 are exchanged: $p_1 \leftrightarrow p_2$.

their free field values, as is described in detail in Refs. [54] and [17].

The choice of external momenta specified by Eq. 4.50 is non-exceptional since no partial sum of these momenta vanish (if their signs are chosen so that all four momenta are incoming) and is the choice used in Refs. [1] and [17]. Such a choice of kinematics is expected to result in normalization conditions which are less sensitive to non-zero quark masses and QCD vacuum chiral symmetry breaking than would be the case if an exceptional set of momenta had been used [56].

Since these RI/MOM renormalization conditions are being imposed for off-shell, gauge-fixed external quark lines, we must in principle include a larger number of operators than the minimal set of seven independent operators which can represent all gauge invariant matrix elements between physical states of H_W. Therefore, we must also employ a correspondingly larger set of conditions to distinguish among this larger set of operators. These additional operators are two-quark operators of dimension three, four and six and are either gauge invariant or non gauge invariant. The treatment of those operators of dimension three and four follows closely that given in Ref. [54]. Equations (12) and (89) of Ref. [17] give a complete list of the corresponding gauge-invariant operators of dimension six. If evaluated between on-shell states, however, these additional operators can be expressed by linear combinations of the seven operators Q'_i.[2] Thus, the relations given in Eq. 4.48 between the seven lattice and the seven RI operators are valid only when those operators appear in physical matrix elements between on-shell states. For this equation to be valid when the operators appear in the off-shell, gauge-fixed Green's functions that define the RI

[2]Exceptions to this statement come from the two dimension-3, mass operators $\overline{s}(1 \pm \gamma^5)d$ which do contribute independently to on-shell matrix elements in which four-momentum is not conserved.

scheme, additional RI/MOM-normalized operators must be added.

This is the meaning of the 7×7 matrix $Z^{\mathrm{lat}\to\mathrm{RI}}$ matrix we evaluate here: gauge symmetry and the equations of motion must be imposed to reduce to the seven RI-normalized operators to which the seven lattice operators are equated. In the calculation of $Z^{\mathrm{lat}\to\mathrm{RI}}$, all such extra dimension six operators are neglected. For all but one, this might be justified for the current calculation because these operators enter only at two loops or beyond and the perturbative coefficients that we are using in later steps are computed at only one loop. A single operator, given in Eq. 146 of Ref. [54] and Eq. 12 of Ref. [17] does appear at one loop but has also been neglected because it is expected to give a smaller contribution than other two-quark operators with quadratically divergent coefficients whose effects are indeed small. While these contributions of such extra operators are believed to be small for the current calculation, care must be taken in future calculations in which a continuum limit is attempted that any neglected counter terms with coefficients of the form $\log(\mu a)$ do not become important.

Based on these discussions, we considered the subtraction of the following dimension 3 and 4 operators,

$$B_1 = \bar{s}d + \bar{s}\gamma_5 d, \tag{4.51a}$$

$$B_2 = \bar{s}(-\overleftarrow{\not{D}} + \overrightarrow{\not{D}})d + \bar{s}(-\overleftarrow{\not{D}} + \overrightarrow{\not{D}})\gamma_5 d, \tag{4.51b}$$

$$B_3 = \bar{s}(\overleftarrow{\not{D}} + \overrightarrow{\not{D}})d + \bar{s}(\overleftarrow{\not{D}} + \overrightarrow{\not{D}})\gamma_5 d, \tag{4.51c}$$

where B_3 is a total derivative operator, and can be rewritten as $B_3 = \not{\partial}(\bar{s}d + \bar{s}\gamma_5 d)$.

The backward and forward derivative operator is implemented on lattice as

$$\bar{s}(x)\overleftarrow{\not{D}}d(x) = (\bar{s}(x+\mu)U_\mu^\dagger(x) - \bar{s}(x))\frac{\gamma_\mu}{2}d(x), \tag{4.52}$$

$$\bar{s}(x)\overrightarrow{\not{D}}d(x) = \bar{s}(x+\mu)\frac{\gamma_\mu}{2}(d(x+\mu) - U_\mu^\dagger(x)d(x)). \tag{4.53}$$

By doing so, the sum of these two terms gives a total derivative

$$\bar{s}(x)(\overleftarrow{\not{D}} + \overrightarrow{\not{D}})d(x) = \bar{s}\gamma_\mu d(x+\mu) - \bar{s}\gamma_\mu d(x) \equiv B_3. \tag{4.54}$$

The subtracted operator is defined as,

$$Q_i''^{sub} = Q_i'' + C_{i1}B_1 + C_{i2}B_2 + C_{i3}B_3, \tag{4.55}$$

where the subtraction coefficients are calculated by imposing the following three conditions:

$$Tr[\left\langle s(p_1)Q_i''^{sub}(x)e^{-i(p_2-p_1)x}\bar{d}(p_2)\right\rangle_{amp}] = 0, \tag{4.56a}$$

$$Tr[(\not{p}_1 + \not{p}_2)\left\langle s(p_1)Q_i''^{sub}(x)e^{-i(p_2-p_1)x}\bar{d}(p_2)\right\rangle_{amp}] = 0, \tag{4.56b}$$

$$Tr[(\not{p}_1 - \not{p}_2)\left\langle s(p_1)Q_i''^{sub}(x)e^{-i(p_2-p_1)x}\bar{d}(p_2)\right\rangle_{amp}] = 0. \tag{4.56c}$$

Based on the structure of the operators Q_i'', let us define a set of flavor, color, and spin structures $H = E_H\Gamma_H$,

$$H_1 = E_1\Gamma_{LL}, \tag{4.57a}$$

$$H_2 = E_2\Gamma_{LL}, \tag{4.57b}$$

$$H_3 = E_3\Gamma_{LL}, \tag{4.57c}$$

$$H_4 = E_1\Gamma_{LR}, \tag{4.57d}$$

$$H_5 = E_2\Gamma_{LR}, \tag{4.57e}$$

$$H_6 = E_3\Gamma_{LR}, \tag{4.57f}$$

$$H_7 = E_4\Gamma_{LR}, \tag{4.57g}$$

where E_i has the structure $E_i^{\alpha\beta\gamma\delta} = q_\alpha(p_1)\bar{q}_\beta(p_2)q_\gamma(p_1)\bar{q}_\delta(p_2)$ where α, β, γ and σ are spinor indices, with different flavor and color structures:

$$E_1 = s^a\bar{d}^a u^b\bar{u}^b, \tag{4.58a}$$

$$E_2 = s^a\bar{d}^b u^b\bar{u}^a, \tag{4.58b}$$

$$E_3 = s^a\bar{d}^a(u^b\bar{u}^b + d^b\bar{d}^b + s^b\bar{s}^b), \tag{4.58c}$$

$$E_4 = s^a\bar{d}^b(u^b\bar{u}^a + d^b\bar{d}^a + s^b\bar{s}^a), \tag{4.58d}$$

and the Γs are the spin tensor structure:

$$\Gamma_{LL} = (V-A)(V-A) = [\gamma_\mu(1-\gamma_5)] \otimes [\gamma_\mu(1-\gamma_5)], \tag{4.59}$$

$$\Gamma_{LR} = (V-A)(V+A) = [\gamma_\mu(1-\gamma_5)] \otimes [\gamma_\mu(1+\gamma_5)]. \tag{4.60}$$

Following the Rome-Southampton prescription, we first calculate the 7×7 matrix M,

$$M_{ij} = Q_i''^{sub} H_j \tag{4.61}$$

This equation symbolically stands for the following operations,

$$Q''^{sub}H = \left[\left\langle Q''^{sub}(x)e^{-i2(p_2-p_1)x}E_H\right\rangle_{amp}\right]^{\alpha\beta,\gamma\delta}\Gamma_H^{\beta\alpha,\delta\gamma}. \tag{4.62}$$

Once we compute M, and the corresponding tree level matrix F, then the mixing NPR matrix is calculated from $Z/Z_q^2 \times M = F$,

$$\frac{Z}{Z_q^2} = FM^{-1}. \tag{4.63}$$

If we had used another set of projection operators H which is a linear transform of our choice of H, say $H' = H \times A$ (we treat H as a row vector), then both M and F will be different, but $Z/Z_q^2 = F'M'^{-1} = (FA) * (MA)^{-1} = FM^{-1}$ is the same.

The tree level mixing matrix F (parity-even part or parity-odd part) can be directly calculated, with the above convention,

$$F = \begin{bmatrix} 3072 & 3072 & 0 & 0 & 0 & 0 & 0 \\ 537.6 & -230.4 & 1152 & 0 & 0 & 0 & 0 \\ -230.4 & 537.6 & 384 & 0 & 0 & 0 & 0 \\ 0 & 0 & 0 & 1152 & 384 & 3456 & 1152 \\ 0 & 0 & 0 & 384 & 1152 & 1152 & 3456 \\ 0 & 0 & 0 & 1152 & 384 & 0 & 0 \\ 0 & 0 & 0 & 384 & 1152 & 0 & 0 \end{bmatrix}.$$

If we have used $H' = HF^{-1}$ with the transformation matrix F^{-1}:

$$(F^{-1}) = \frac{1}{9216} \begin{bmatrix} 9/5 & 3 & -9 & 0 & 0 & 0 & 0 \\ 6/5 & -3 & 9 & 0 & 0 & 0 & 0 \\ -3/5 & 6 & 6 & 0 & 0 & 0 & 0 \\ 0 & 0 & 0 & 0 & 0 & 9 & -3 \\ 0 & 0 & 0 & 0 & 0 & -3 & 9 \\ 0 & 0 & 0 & 3 & -1 & -3 & 1 \\ 0 & 0 & 0 & -1 & 3 & 1 & -3 \end{bmatrix}.$$

then we will get $F' = 1$, and $Z/Z_q^2 = M'^{-1}$ with the off-diagonal terms of Z all coming from M'.

There are three stuctures we need to consider based on the path of the contractions on the spin index, which are shown in Fig.15. For each graph, the color can be mixed or unmixed in the operator. We use letter $\mathcal{M}$ to stands for color mixed structure. Then there are six different structures, which define six 4-Tensors. Reading

from the graph, for example, we have the amputated Green's function (a 4-tensor),

$$\begin{aligned}(F_{\Gamma_A\Gamma_B})^{abcd}_{\alpha\beta\gamma\delta} =&\langle\frac{1}{V}\sum_{x,\mu}[e^{-i2(p_2-p_1)x}(\gamma_5 S^\dagger(x,p_1)\gamma_5)^{aa'}\Gamma^\mu_A S(x,p_2)^{a'b} \\ &\cdot(\gamma_5 S^\dagger(x,p_1)\gamma_5)^{cc'}\Gamma^\mu_B S(x,p_2)^{c'd}]\rangle_{amp},\end{aligned} \tag{4.64}$$

$$\begin{aligned}(F_{\Gamma_A\Gamma_B})^{abcd}_{\alpha\beta\gamma\delta} =&\langle\frac{1}{V}\sum_{x,\mu}[e^{-i2(p_2-p_1)x}(\gamma_5 S^\dagger(x,p_1)\gamma_5)^{aa'}\Gamma^\mu_A S(x,p_2)^{c'b} \\ &\cdot(\gamma_5 S^\dagger(x,p_1)\gamma_5)^{cc'}\Gamma^\mu_B S(x,p_2)^{a'd}]\rangle_{amp},\end{aligned} \tag{4.65}$$

where $S(x,p)$ stands for a volume momentum propagator, with the source carrying momentum p. All other contraction terms can be written done following the graph in Fig.15. The loop in the contraction is approximated by a few random volume source propagators $S_r(x)$ with the source $\xi_r(x)$

$$L(x,x) \approx \frac{1}{N}\sum_{r=1}^{N} S_r(x)\xi_r^*(x). \tag{4.66}$$

One example of these graphs,

$$\begin{aligned}(\mathcal{M}_{\Gamma_A\Gamma_B D_1})^{abcd}_{\alpha\beta\gamma\delta} =&\langle\frac{1}{V}\sum_{x,\mu}[e^{-i2(p_2-p_1)x}(\gamma_5 S^\dagger(x,p_1)\gamma_5)^{aa'}\Gamma^\mu_A S(x,p_2)^{b'b} \\ &\cdot Tr_s(\Gamma^\mu_B L(x,x))^{a'b'}]S(p1,p2)^{cd}\rangle_{amp}.\end{aligned} \tag{4.67}$$

The amputation of a 4-tensor A means:

$$[\langle A\rangle_{amp}]_{\alpha\beta\gamma\delta} = \langle A\rangle_{\alpha'\beta'\gamma'\delta'}\,(\gamma_5 S^\dagger(p_1)\gamma_5)^{-1}_{\alpha\alpha'}(\gamma_5 S^\dagger(p_1)\gamma_5)^{-1}_{\gamma\gamma'}S(p_2)^{-1}_{\beta'\beta}S(p_2)^{-1}_{\gamma'\gamma}, \tag{4.68}$$

where the indices stand for both color and spin indices.

We calculate $MF^{-1} = Z^{\text{lat}\to\text{RI}}(\mu,a)/Z_q^2$ using volume momentum sources on the $16^3\times 32$ lattices. Since the parity-even and parity-odd parts do not mix, we calculated the NPR matrix in both ways. In addition, to show the effects of the mixing operators, we also include the results without the mixing operators. Table 6 summarizes the

results with input quark mass 0.01 (and valence quark mass 0.01) and energy scale 2.15 GeV. It shows that the mixing operators have negligible effects. The results from parity-even and parity-odd part of the operators are statistically consistent except a few zero elements (notice that these ensembles also have large discritization error).

The parity-even part gives nonzero value for the mixing between Q_6'' and Q_1'', etc, while the parity-odd part gives zero. This can be qualitative understood from the difference of Λ_V and Λ_A. Since we have

$$\begin{aligned}(MF^{-1})_{6,1} =& \frac{1}{30720} Tr[\{(V-A)(V-A)\} \\ & \cdot \langle Q_6''(3E_1+2E_2-E_3)\rangle_{amp}],\end{aligned} \tag{4.69}$$

$$\begin{aligned}(MF^{-1})_{1,6} =& \frac{1}{9216} Tr[\{(V-A)(V+A)\} \\ & \cdot \langle Q_1''(9E_1-3E_2-3E_3+E_4)\rangle_{amp}].\end{aligned} \tag{4.70}$$

the parity even part looks something like $\Lambda_V^2 - \Lambda_A^2$ which equals 0.0041 for $(ap)^2 = 1.234$ case. And parity odd case looks like $\Lambda_V\Lambda_A - \Lambda_A\Lambda_V$, therefore gives zero. Table 7 is similar to Table 6 except that the momentum scale is at 1.92 GeV. Table 8 is the result for the $m_l = 0.02$ lattice.

The final matrix $Z^{\text{lat}\to\text{RI}}(\mu, a)/Z_q^2 = FM^{-1} = (MF^{-1})^{-1}$ obtained at $\mu = 2.15$ GeV that we used in this thesis is given in Tab. 9. Since the main goal of this work is on the weak matrix elements and that is the main source of error, we use the old data from Ref. [1] for consistency with Ref. [57] even though it has larger error (but much smaller than the error from the weak matrix elements in Isospin 0 channel).

In the second step we convert the seven RI operators obtained above into the $\overline{\text{MS}}$ scheme:

$$Q_i'^{\overline{\text{MS}}} = \sum_j \left(1 + \Delta r^{\text{RI}\to\overline{\text{MS}}}\right)_{ij} Q_j^{\text{RI}}. \tag{4.71}$$

Here the indices i and j run over the set $\{1, 2, 3, 5, 6, 7, 8\}$ corresponding to the chiral basis of the operators Q_j defined above and a set of operators $Q'^{\overline{\rm MS}}_j$, with identical chiral properties, which are defined in Ref. [17]. We use the computational framework described in Ref. [17] and the resulting 7×7 matrix $\Delta r^{\rm RI \to \overline{MS}}$ is given in Tab. VIII of that reference. As in the case of Eq. 4.48, the two sets of seven RI and $\overline{\rm MS}$ operators are related by this 7×7 matrix only when appearing in physical matrix elements. Since the values in this table were obtained in Ref. [1] for the case that the wave function renormalization constant for the quark field is the quantity $Z_q^{\not q}$ defined in Ref. [17], it is that factor which we use to extract $Z^{\rm lat \to RI}$ from the matrix $Z^{\rm lat \to RI}/Z_q^2$ given in Tab. 9. For our $\beta = 2.13$, Iwasaki gauge ensembles $Z_q^{\not q} = 0.8016(3)$. (Note, $Z_q^{\not q}$ is the same as the quantity Z'_q introduced in earlier exceptional momentum schemes [58].)

A third and final step is needed before we can combine the Wilson coefficients with the matrix elements determined in our calculation to obtain the physical amplitudes A_0 and A_2. The 7×7 matrix given in Tab. VIII of Ref. [17] gives us $\overline{\rm MS}$ operators defined in the chiral basis. However, the Wilson coefficients which are available in Ref. [18] are defined for the ten operators basis referred to as basis I in Ref. [17]. The conversion between the linearly independent, seven operator basis and the conventional set of ten linearly dependent operators is correctly given by the application of simple Fierz identities for the case of the lattice and RI/MOM operators. As is explained, for example, in Ref. [17], this procedure is more complex for operators defined using $\overline{\rm MS}$ normalization. Here subtleties of defining γ^5 in dimensions different from four result in ten $\overline{\rm MS}$-normalized operators, $Q_i^{\overline{\rm MS}}$, which are not related by the usual Fierz identities, with Fierz violating terms appearing at order α_s.

Thus, the conventional ten $\overline{\rm MS}$-normalized operators $Q_i^{\overline{\rm MS}}$ which appear in Eq. 2.57

must be constructed, again through one-loop perturbation theory, from the seven operators $Q_i'^{\overline{\rm MS}}$:

$$Q_i^{\overline{\rm MS}} = \sum_j \left(T + \Delta T_I^{\overline{\rm MS}} \right)_{ij} Q'^{\overline{\rm MS}}_j, \tag{4.72}$$

in the notation of Ref. [17]. The 10×7 matrices, T and $\Delta T_I^{\overline{\rm MS}}$ are given in Eqs. 59 and 65 of that reference. (The subscript I on the matrix $\Delta T_I^{\overline{\rm MS}}$ identifies the particular ten-operator, $\overline{\rm MS}$ basis required by the Wilson coefficients of Ref. [18].)

This entire set of non-perturbative and perturbative transformations can be summarized by the following equation which expresses the ten $\overline{\rm MS}$-normalized operators $Q_i^{\overline{\rm MS}}$ in terms of the seven, chiral basis, lattice operators whose matrix elements we actually compute:

$$\begin{aligned} Q_i^{\overline{\rm MS}} &= \sum_j \left[\left(T + \Delta T_I^{\overline{\rm MS}} \right)_{10\times 7} \left(1 + \Delta r^{\rm RI \to \overline{\rm MS}} \right)_{7\times 7} \left(Z^{\rm lat \to RI} \right)_{7\times 7} \right]_{ij} Q_j^{\rm lat} \qquad (4.73) \\ &= \sum_j \left[\left(Z^{\rm lat \to \overline{\rm MS}} \right)_{10\times 7} \right]_{ij} Q_j^{\rm lat}, \qquad (4.74) \end{aligned}$$

where the subscripts indicate the dimensions of the matrices being multiplied and the matrix $Z_{ij}^{\rm lat \to \overline{\rm MS}}$ is used in Eq. 4.1.

Chapter 5

Results from the $16^3 \times 32 \times 16$ Lattice

In the previous chapter, we have set up all the building blocks for the decay amplitudes calculation. In this chapter, we will show the results from the $16^3 \times 32 \times 16$ lattice. Because of the computational difficulty associated with this calculation, our first trial calculation uses a relatively small lattice, and the kaons and pions are unphysical. It is a threshold calculation in which the two pions carry very small momentum. The details of this lattice ensemble and the computation setup are described in Section 5.1. Then the $\pi - \pi$ scattering results are shown for both $I = 2$ and $I = 0$ in Section 5.2. For this lattice, because the time extent T=32 is small, we find that the contributions from the around-the-world graphs are large. They are discussed together with the results of the decay amplitudes in Section 5.3 for the $\Delta I = 3/2$ channel and Section 5.4 for the $\Delta I = 1/2$ channel.

5.1 Computational Details

This lattice ensemble uses the Iwasaki gauge action with $\beta = 2.13$ and domain wall fermions that we briefly described in Section 3.1. The light sea quark mass is $m_l = 0.01$ and the strange quark mass is $m_s = 0.032$. This ensemble is similar to the $m_l = 0.01$ ensemble reported in Ref. [59] except we use the improved RHMC-II algorithm of Ref. [60] and a more physical value for the strange quark mass. The inverse lattice spacing for these input parameters was determined to be 1.73(3) GeV and the residual mass is $m_{\rm res} = 0.00308(4)$ [60]. The total number of configurations we used is 800, each separated by 10 time units. We initially generated an ensemble one-half of this size. When our analysis showed a non-zero result for ReA_0, we then doubled the size of the ensemble to assure ourselves that the result was trustworthy and to reduce the resulting error. We have performed the analysis described below both by treating the results from each configuration as independent and by grouping them into blocks. The resulting statistical errors are independent of block size suggesting that the individual configurations are essentially uncorrelated for our observables.

We use anti-periodic boundary conditions in the time direction, and periodic boundary conditions in the space directions for the Dirac operator. The propagators (inverses of the Dirac operator) are calculated using a Coulomb gauge fixed wall source (used for meson propagators) and a random wall source (used to calculate the loops in the *type*3 and *type*4 graphs shown in Figs. 12 and 13 below) for each of the 32 time slices in our lattice volume. The details of these sources are already discussed in Section 3.3. For each time slice and source type, twelve inversions are required corresponding to the possible 3 color and 4 spin choices for the source. Thus, all

together we carry out 768 inversions for each quark mass on a given configuration. As it will be shown below, this large number of inversions, performed on 800 configurations, provides the substantial statistics needed to resolve the real part of the $I = 0$ amplitude A_0 with 25% accuracy.

The situation described above in which 768 Dirac propagators must be computed on a single gauge background is an excellent candidate for the use of EigCG algorithm that we described earlier. However, at the time this calculation was done, the EigCG algorithm was not available, so we used deflation techniques. The overhead associated with determining a set of low eigenmodes of this single Dirac operator can be effectively amortized over the many inversions in which those low modes can be used. Our $m_l = 0.01$, light quark inversions are accelerated by a factor of 2-3 by using exact, low-mode deflation [61] in which we compute the Dirac eigenvectors with the smallest 35 eigenvalues and limit the conjugate gradient inversion to the remaining orthogonal subspace.

In order to obtain energy-conserving $K^0 \to \pi\pi$ decay amplitudes, the mass of the valence strange quark in the kaon is assigned a value different from that appearing in the fermion determinant used to generate the ensembles, *i.e.* the strange quark is partially quenched. Since the mass of the dynamical strange quark is expected to have a small effect on amplitudes of the sort considered here [60, 62], this use of partial quenching is appropriate for the purposes of this paper. Valence strange quark masses are chosen to be $m_s = 0.066$, 0.099 and 0.165, which are labeled 0, 1 and 2 respectively. The resulting kaon masses are shown in Tab. 10. In the following section we will see that by using these values for m_s we can interpolate to energy-conserving decay kinematics for both the $I = 2$ and $I = 0$ channels.

5.2 Two Pions States

Our results for each of the four types of contractions that we describe in Section 4.1 are shown in the top panel of Fig. 16. Notice that the disconnected (vacuum) graph has an almost constant error with increasing time separation between the source and sink, so it appears to have an increasing error bar in the log plot, while the signal decreases exponentially.

The fitted energies are summarized in Tab. 10. In order to see clearly the effect of the disconnected graph, we also perform the calculation for the $I = 0$ channel without the disconnected graphs. This result is given in Tab. 10 with a label with an additional prime ($\prime$) symbol. The resulting effective mass plots for each case are shown in the bottom panel of Fig. 16. For comparison, a plot of twice the pion effective mass is also shown. This figure clearly demonstrates that the two-pion interaction is attractive in the $I = 0$ channel with the finite volume, $I = 0$ $\pi - \pi$ energy $E_0^{\pi\pi}$ lower than $2m_\pi$. In contrast, the $I = 2$ channel is repulsive with $E_2^{\pi\pi}$ larger than $2m_\pi$. The fitted parameters $N_I^{\pi\pi}$ and $E_I^{\pi\pi}$ will be used to extract weak matrix elements from the $K^0 \to \pi\pi$ correlation functions discussed below in which these same operators $O_I^{\pi\pi}(t)$ are used to construct the two-pion states.

5.3 $\Delta I = 3/2$ Amplitude

As Eqs. 4.25 and 4.28a show, the $\Delta I = 3/2$ $K^0 \to 2\pi$ decay amplitude includes only *type*1 contractions and four of the correlation functions are related

$$A_{2,10} = A_{2,9} = \frac{3}{2} A_{2,1} = \frac{3}{2} A_{2,2}. \tag{5.1}$$

Therefore, we need only to calculate $A_{2,1}$, $A_{2,7}$ and $A_{2,8}$. The corresponding three correlation functions, $C_{2,i}(\Delta, t)$ for $i = 1$, 7 and 8, with the choice of $m_K^{(1)}$ for the kaon mass, are shown in Fig. 17. In the figure, we plot $C_{2,i}(\Delta, t)$ for $0 < t < \Delta$ at fixed $\Delta = 12$ or 16. Table 10 shows that $m_K^{(1)}$ is almost equal to the energy of $I = 2$, $\pi - \pi$ state, so the 3-point correlation function $C_{2,i}(\Delta, t)$ should be approximately independent of t in the central region where the time coordinate of the operator is far from both the kaon and the two-pion sources, $0 \ll t \ll \Delta$. Based on Eq. 4.37, the fitted results for the matrix elements $M_i^{3/2,\mathrm{lat}}$ from $\Delta = 12$ are listed in Tab. 11 in lattice units.

Figure 17 shows that for the operators Q_7 and Q_8 the larger separation, $\Delta = 16$, between the kaon source and $\pi - \pi$ sink gives a much shorter plateau region than the case $\Delta = 12$. This behavior is inconsistent with the usual expectation that they are the contributions from excited states of the kaon and pion, contributions which should be suppressed for larger Δ, that cause the poor plateau. An alternative, consistent explanation attributes the shortened plateau region seen for $\Delta = 16$ to the 'around-the-world' effect. This is the contribution to the correlation function in which the two-pion interpolating operator at the sink annihilates one pion and creates another (instead of annihilating two pions as in the $K \to \pi\pi$ contribution we are seeking) and the process at the weak operator is $K\pi \to \pi$ (instead of $K \to \pi\pi$). While one pion travels from the weak operator to the $\pi - \pi$ sink the second is created at the sink and travels forward in time, passing through the periodic boundary to reach the weak operator together with the kaon. The corresponding dominant path is shown in Fig. 18. The time dependence of this behavior can be estimated as

$$\sim M_i^{3/2,\mathrm{lat}} N_\pi^2 N_K e^{-m_\pi T} e^{-(E_{K\pi} - m_\pi)t} \tag{5.2}$$

which is Δ independent but suppressed by the factor $\exp(-m_\pi T)$, where N_π is the analogue of N_K for the case of single pion production and $T = 32$ is the temporal extent of the lattice. In contrast, the physical contribution in Eq. 4.37 is suppressed by $\exp(-E_{\pi\pi}\Delta)$. Thus, the second, standard term falls with increasing Δ and the two factors are of similar size when $\Delta = T/2$. Therefore, we should expect to see a large contamination from such around-the-world effects in the $\Delta = 16$ case, consistent with Fig. 17. In both panels of that figure, we plot as three horizontal lines the fitted result from $\Delta = 12$ for the three amplitudes $M_i^{3/2,\mathrm{lat}} N_{\pi\pi} N_K \exp\{-\Delta E_{\pi\pi}\}$ for $i = 1$, 7 and 8. The agreement between these lines and the short plateaus seen in the right-hand, $\Delta = 16$ panel indicates consistency between these two values of Δ.

Additional evidence supporting this explanation for the short plateau in the case of $\Delta = 16$ can be obtained by examining the explicit dependence on t given by Eq. 5.2 for the around-the-world contribution. Examining the exponential decay with t in the $\Delta = 16$ correlators plotted in the right panel of Fig. 17, for operators Q_7 and Q_8 we find a value for $E_{K\pi} - m_\pi$ varying between 0.4 and 0.5 depending on the choice of fit range. A more accurate value of 0.498(2) can be obtained by fitting the corresponding correlator for $\Delta = 20$ and a fit range of 5 to 11. The strangeness-carrying state whose mass we have labeled $E_{K\pi}$ can be formed from two quarks and must be parity even. Direct calculation of $E_{K\pi}$ from a scalar $\overline{s}d$ correlator yields $E_{K\pi} = 0.752(12)$ which is consistent with the sum of the result above, $E_{K\pi} - m_\pi = 0.498(2)$, and the pion mass $m_\pi = 0.2437(5)$. (This energy difference is also close to the kaon mass $m_K^{(1)} = 0.50729$ given in Tab. 10.) Thus, the time dependence expected from the around-the-world path is quite consistent with that seen in Fig. 17.

We conclude that it is important to increase the lattice extent in the time direction

both to suppress this around-the-world effect and to permit the use of a larger source-sink separation giving a longer plateau. We will return to discussion of the around-the-world effect below for the $\Delta I = 1/2$ kaon decay where it creates even greater difficulties. However, here we can begin to appreciate the severity of this effect in the $K^0 \to \pi\pi$ system for our temporal lattice extent of 32, given our values of the lattice spacing and meson masses. In the next chapter, we will show our results from $T = 64$ lattice and no such difficulties there.

The $I = 2$ phase shift $\delta_2(p)$ is determined from the measured two-pion energy $E_{\pi\pi} = 0.443(13)$ given in Tab. 10 and the finite volume quantization condition of Eq. 4.9 gives $\delta_2(p) = -0.0849(43)$. Because of the small value of p we assume that $\delta_2(p)$ is a linear homogenous function of p and write $\delta_2(p) = p\partial\delta_2(p)/\partial p$, the quantity required in Eq. 4.47 and given in Tab. 12. Results for F in this $I = 2$ case and the quantities used to determine it are given in Tab. 12. We should note that applying the finite volume correction of Eq. 4.47 gives us a finite-volume corrected amplitude for a $\Delta I = 3/2$, $K \to \pi\pi$ decay that is slightly above threshold by the amount $E_2^{\pi\pi} - 2m_\pi = 33(1)$ MeV.

We can now combine everything and calculate the $K^0 \to \pi\pi$ decay amplitudes based on Eq. 4.1. The results for the complex $\Delta I = 3/2$ decay amplitude A_2 are summarized in Tab. 13, including those for the other two, energy-non-conserving choices of kaon mass. Since $m_K^{(1)}$ differs from the isospin-2 $\pi - \pi$ energy by only 0.2 percent, we quote this case as our energy-conserving kaon decay amplitude. Therefore, in physical units, we obtain the energy-conserving $\Delta I = 3/2$, $K^0 \to \pi\pi$ complex,

threshold decay amplitude for $m_K = 877$ MeV and $m_\pi = 422$ MeV:

$$\mathrm{Re}(A_2) = 4.911(31) \times 10^{-8}\mathrm{GeV} \quad (5.3)$$

$$\mathrm{Im}(A_2) = -0.5502(40) \times 10^{-12}\mathrm{GeV}. \quad (5.4)$$

5.4 $\Delta I = 1/2$ Amplitude

Based on Eq. 4.26 and 4.36, we have calculated the $\Delta I = 1/2$ kaon decay correlation functions, $C_{0,i}(\Delta, t)$ for each of the ten effective weak operators. In the calculation we treat each of these ten operators as independent and then verify that the identities shown in Eq. 2.59 are automatically satisfied. Figures 19 and 20 show two examples of the resulting correlation functions for the operators Q_2 and Q_6, in the case of the lightest kaon $m_K^{(0)}$. Table 10 shows that the mass of this kaon is very close to the energy of the I=0 two-pion state. Therefore, we expect to get a reasonably flat plateau when the operator is far from both the source and sink.

Given this good agreement between the energies of the K and $\pi - \pi$ states, we might expect that the unphysical, dimension three operator, $\overline{s}\gamma^5 d$ which mixes with the $(8, 1)$ operators in Eq. 2.57 and is itself a total divergence, will also give a negligible contribution to such an energy and momentum conserving matrix element. However, as can be seen from Figs. 19(a) and 20(a), the matrix element of this term is large and the explicit subtraction described in Sec. 4.2 is necessary.

This difficulty is created by the combination of two phenomena. First the mixing coefficient which multiplies the $\overline{s}\gamma^5 d$ operator when it appears in our weak $(8, 1)$ operators is large, of order $(m_s - m_l)/a^2$. Second, in our lattice calculation the

necessary energy conserving kinematics (needed to insure that this total divergence does not contribute) is only approximately valid. The required equality of the spatial momenta of the kaon and $\pi - \pi$ states is assured by our summing the location of the weak vertex over a complete temporal hyperplane. On the other hand, the equality of the energies of the initial and final states results only if we have adjusted the kaon mass to approximately that of the two-pion state and chosen the time extents sufficiently large that other states with different energies have been suppressed. However, as can be seen in Figs. 19(a) and 20(a) the subtraction terms $mix3$ and $mix4$ show strong dependence on the time at which they are evaluated. This implies that there are important contributions coming from initial and final states which have significantly different energies. One or both of these states is then not the intended K or $\pi - \pi$ state but instead an unwanted contribution which has been insufficiently suppressed by the time separations between source, weak operator and sink.

Thus, instead of relying on large time extents and energy conserving kinematics to suppress this unphysical, $O(1/a^2)$ term we must explicitly remove it. As explained in Sec. 4.2 this can be done by including an explicit subtraction which we fix by the requirement that the kaon to vacuum matrix element of the complete subtracted operator vanishes as in Eq. 4.32. Thus, we determine the divergent coefficient of this mixing term from the ratio $\alpha_i = \langle 0|Q_i|K\rangle / \langle 0|\bar{s}\gamma^5 d|K\rangle$ and then perform the explicit subtraction of the resulting terms, labeled $\alpha_i \cdot mix3$ and $\alpha_i \cdot mix4$ in Figs. 19 and 20.

Of course, the finite part of such a subtraction is not determined from first principles and our choice, specified by Eq. 4.32 is arbitrary. Thus, we must rely on our identification of a plateau and the approximate energy conservation of our kinematics to make the arbitrary part of this subtraction small, along with the other errors

associated with evaluating the decay matrix element of interest between initial and final states with slightly different energies.

We now examine the very visible time dependence in Figs. 19(a) and 20(a) for both the original matrix elements and the subtraction terms in greater detail. As discussed above one might expect these divergent subtraction terms to contribute to excited state matrix elements in which the energies of the initial and final states are very different. Typical terms should be exponentially suppressed as the separation between the weak operator and the source or sink is increased, with the time behavior $\exp\{-(m_K^*-m_K)t\}$ or $\exp\{-(E_{\pi\pi}^*-E_{\pi\pi})(\Delta-t)\}$, which ever is larger. (The $*$ denotes an excited state.) However, by carefully examining the time behavior of the $mix3$ amplitude, we find that the time dependence, at least in the vicinity of the central region, is less rapid than might be expected from such excited states suggesting that it is probably not due primarily to contamination from excited states.

We believe that the dominant, energy-nonconserving matrix elements which cause the significant time dependence in Figs. 19 and 20 arise from the around-the-world effects identified and discussed in the previous $\Delta I = 3/2$ section. In fact, for the reasons just discussed associated with divergent operator mixing, such around-the-world effects are a more serious problem in the $\Delta I = 1/2$ case. The dominant around-the-world graphs are shown in Fig. 21. An estimate of the time dependence of these graphs gives,

$$\begin{aligned} &< K^0\pi|Q_i|\pi > N_\pi N_K N_\pi e^{-m_\pi T} e^{-(E_{K\pi}-m_\pi)t} \\ &+ < 0|Q_i|K^0\pi\pi > N_\pi N_K N_\pi e^{-m_K((T-\Delta)+(\Delta-t))}\,, \end{aligned} \tag{5.5}$$

where the first term comes from the first two graphs of Fig. 21, while the second term

comes from the third graph. (Recall that $t = t_{\rm op} - t_K$ and $\Delta = t_\pi - t_K$). Notice that these two terms involve amplitudes which are far from energy conserving and therefore contain large divergent contributions from mixing with the operator $\overline{s}\gamma_5 d$ which will be removed only when combined with the corresponding around-the-world paths occuring in the $mix3$ contraction.

We conclude that it is these around-the-world matrix elements which are the reason for the observed large divergent subtraction in the $type3$ graph. The largest divergent contribution is thus not the subtraction for the matrix element we are trying to evaluate, $< \pi\pi|Q_i|K^0 >$; rather, it is the divergent subtraction for the matrix elements $< K^0\pi|Q_i|\pi >$ and $< 0|Q_i|K^0\pi\pi >$ which arise from the around-the-world paths which are not sufficiently suppressed by our lattice size. Two important lessons can be learned from this analysis. First, it is important to perform an explicit subtraction of the divergent mixing with the operator $\overline{s}\gamma_5 d$. While this term will not contribute to the energy conserving matrix element of interest, in a Euclidean space lattice calculation there are in general, other, unwanted, energy non-conserving terms which may be uncomfortably large if this subtraction is not performed. Second it would be wise to work on a lattice with a much larger size T in time direction in order to suppress further the around-the-world terms which give such a large contribution in the present calculation. Using the average of propagators computed with periodic plus anti-periodic boundary conditions to effectively double the length in the time direction would be a good solution.

We should emphasize that these divergent, around-the-world contributions do not pose a fundamental difficulty. The largest part of these amplitudes are removed by the corresponding subtraction terms constructed from the operator $\overline{s}\gamma_5 d$. The remaining

finite contributions from this and other around-the-world terms are suppressed by the factor $\exp(-m_\pi T)$ or $\exp(-m_K(T-\Delta))$. Fortunately, the large divergent subtraction also reduces the statistical errors substantially, especially for the *type*4 vacuum graphs, which indicates the expected strong correlation between the divergent part of the weak operator and the corresponding $\overline{s}\gamma_5 d$ subtraction. Our results suggest that the separation of $\Delta = 16$ gives a relatively longer plateau region, so we use that $K - \pi\pi$ time separation in the analysis below.

The lattice matrix elements are determined by fitting the $I = 1/2$ correlators $C_0^i(\Delta, t)$ with the function form described in Eq. 4.37. The fitted results for the weak, $\Delta I = 1/2$ matrix elements of all ten operators are summarized in Tab. 14. To see the effects of the disconnected graph clearly, a second fit is performed to the amplitude from which the disconnected, *type*4 graphs have been omitted and the calculated results are shown with an additional $\prime$ label, as in the earlier two-pion scattering section.

The calculation of the $\Delta I = 1/2$ decay amplitude A_0 from the lattice matrix elements $M_i^{1/2,\mathrm{lat}}$ given in Tab. 14 is very similar to the $\Delta I = 3/2$ case: the values of $M_i^{1/2,\mathrm{lat}}$ are simply substituted in Eq. 4.1. However, the attractive character of the $I = 0$, $\pi - \pi$ interaction and resulting negative value of p^2 makes the Lellouch-Lüscher treatment of finite volume corrections inapplicable. For the repulsive $I = 2$ case, we could apply this treatment to obtain the decay amplitude for a two-pion final state which was slightly above threshold corresponding to the actual finite volume kinematics. In the present case there is no corresponding infinite-volume decay into two pions below threshold and an unphysical increase of m_π to compensate for the finite volume $\pi - \pi$ attraction will introduce an $O(1/L^3)$ error in the decay amplitude

of the same size as that which the Lellouch-Lüscher treatment corrects. Thus, for this $\Delta I = 1/2$ we do not include finite volume corrections and simply use the free-field value for the factor F in Eq. 4.1.

While we believe that we cannot consistently apply the Lellouch-Lüscher finite volume correction factor to improve our result for the $I = 0$, $K \to \pi\pi$ decay amplitude, we might still be able to use the quantization condition of Eq. 4.9 to determine the $I = 0$ $\pi - \pi$ scattering phase shift $\delta_0(p)$. Even though Eq. 4.9 can be analytically continued to imaginary values of the momentum p, its application for large negative p^2 is uncertain since the function $\phi(q)$ becomes ill defined. In fact, our value of p^2 sits very close to a singular point of $\phi(q)$. We believe this happens because the condition on the interaction range $R \ll L/2$ used to derive the quantization condition in Eq. 4.9 is not well satisfied for our small volume. This impediment to determining $\delta_0(p)$ will naturally disappear once we work with lighter pions in a larger volume or pions that carry momentum.

The results for $\mathrm{Re}(A_0)$ and $\mathrm{Im}(A_0)$ are summarized in Tab. 15 and the individual contribution from each of the operators is detailed in the last two columns of Tab. 14. Within a large uncertainty Tab. 14 shows that the largest contribution to $\mathrm{Re}(A_0)$ comes from operator Q_2, and that to $\mathrm{Im}(A_0)$ from Q_6 as found, for example, in Refs. [54, 63].

Since the choice $m_K^{(0)}$ for the kaon mass is not precisely equal to the energy of the $I = 0$ $\pi\pi$ state, we carried out a simple linear interpolation between $m_K^{(0)}$ and $m_K^{(1)}$ to obtain an energy conserving matrix element, which is shown in the last row of Tab 15. In terms of physical units, therefore, our full calculation gives the energy conserving, $K^0 \to \pi\pi$, $\Delta I = 1/2$, complex decay amplitude A_0 for $m_K = 766$ MeV

and $m_\pi = 422$ MeV:

$$\mathrm{Re}(A_0) = 3.80(82) \times 10^{-7}\mathrm{GeV} \quad (5.6)$$

$$\mathrm{Im}(A_0) = -2.5(2.2) \times 10^{-11}\mathrm{GeV}. \quad (5.7)$$

These complete results can be compared with those obtained when the disconnected graphs are neglected given in Tab. 15. We will discuss more about these numerical results in Chapter 7.

Chapter 6

Results from the $24^3 \times 64 \times 16$ Lattice

The successful calculation that we described in the last chapter encouraged us to perform the calculation on another lattice with larger volume and lighter pion mass. In this chapter, we will show the results from the $24^3 \times 64 \times 16$ lattice ensemble that is generated using the same techniques described in the last chapter for the $16^3 \times 32$ lattice. First, with a sufficiently large T of 64, the around-the-world graph that causes difficulty for the $T = 32$ lattice is completely removed. Second, we implement the EigCG algorithm described in Section 3.4 which gives us a factor of 5.5 speed up for the light quark mass calculation, or an overall total speedup of 3.3. Last, we use a new technique to suppress the vacuum noise, by separating the two wall source pions by a few times slices. In the following, we will first introduce this technique together with the $\pi - \pi$ scattering results. Then the decay amplitudes are calculated for a threshold calculation as we did in the last chapter. All the results are from 138

configurations separated by 40 trajectories.

6.1 Time Separated $\pi - \pi$ Source

The sea quark masses for this ensemble are $m_l = 0.005$, $m_s = 0.032$. To allow threshold kaon decay close to energy conserving, the strange quark mass is partially quenched. The valence strange quark mass is chosen to be $m_s^{val} = 0.056$, which makes the kaon mass approximately equal to twice of the pion mass. The fitted mass are summarized in Tab.16.

In this section, we introduce a new technique that targets the calculation of the $I = 0$ $\pi-\pi$ state. The disconnected graph imposes a great difficulty to our calculation. One way to suppress the vacuum noise is to separate the two pions in space to avoid direct overlap of the two pions and suppress their immediate annihilation into the vacuum. However, this introduces other difficulties because we have to use some other complicated sources different from the wall source. On the other hand, separating the two-pion sources in the time direction can achieve vacuum noise suppression as well, while we can still use wall sources. As shown in Fig.22, for both $\pi - \pi$ scattering and kaon decay calculations, we introduce a separation δ in the time direction between the two wall source pions. We use a conservative difinition of time separation t between the source and sink.

The calculated $\pi - \pi$ energies in $I = 2$ and $I = 0$ channel are summarized in Tab.16. With $\pi - \pi$ separation of 0, 2, and 4, we can see from Fig.23 that the introduction of a small separation on the two pion sources greatly improves the quality of the effective mass plateau for the $I = 0$ $\pi - \pi$ state. The fitted energies with

errors for the different values of δ are summarized in Tab.17. For $I = 2$ states, the introduction of δ does not help.

6.2 $\Delta I = 3/2$ Amplitude

The calculated correlation functions and the fits for the matrix elements of the operator Q_1, Q_7 and Q_8 are shown in Fig.24. Since we already averaged over all possible time locations for sources, averaging over the calculated values with different source-sink separations does not help to reduce the noise. So we pick the one that has a long good plateau. Figure 24 shows the result with $\Delta = 20$ and $\delta = 4$. The fitted values of the weak matrix elements on lattice are summarized in Tab.18. Notice that with this $T = 64$ lattice, we have completely removed the contribution from the around-the-world graph that we have seen with the $T = 32$ lattice.

The Lellouch-Lüscher factor calculation is shown in Tab.19. Putting things together in the same way as we did in the last chapter, we calculate the $\Delta I = 3/2$ decay amplitude, and the contribution from each of the operators. These results are presented in Tab.18. In summary, we performed a threshold decay calculation for a $m_K = 662$ MeV kaon decaying to two $m_\pi = 329$ MeV pions in the $\Delta I = 3/2$ channel. The amplitudes are

$$\mathrm{Re}(A_2) = 2.668(14) \times 10^{-8}\mathrm{GeV} \quad (6.1)$$

$$\mathrm{Im}(A_2) = -6.509(34) \times 10^{-13}\mathrm{GeV}. \quad (6.2)$$

6.3 $\Delta I = 1/2$ Amplitude

Figure 25 to 34 show the calculated weak matrix elements in the $\Delta I = 1/2$ channel for each of the ten operators, with and without the disconnected graph, with $K - \pi$ separation $\Delta = 16$ and $\pi - \pi$ separation $\delta = 4$. The fitted value for the weak matrix elements are summarized in Tab.20. In the same fashion as the last chapter, the calculated decay amplitudes and the contributions from each of the ten operators are also assembled together in Tab.20.

Using a shorter separation can suppress the noise. So we also calculate the results with $\Delta = 12$. Figure 35 to 44 shows the correlation function and fitting for the weak matrix elements. The fitted results and the decay amplitudes are summarized in Tab.21. It shows that the results from $\Delta = 12$ are a little bit more accurate. However, we should notice that it is sensitive to the fitting range we used. In $\Delta = 12$, the fitting range is from 4 to 8. And in $\Delta = 16$ case, we use fitting range from 5 to 11.

The results from these two different separations are consistent. We quote the results from $\Delta = 12$ as our final result. The amplitudes for the $\Delta I = 1/2$, 662 MeV kaon to two 329 MeV pions, are

$$\mathrm{Re}(A_0) = 3.21(45) \times 10^{-7}\mathrm{GeV} \tag{6.3}$$

$$\mathrm{Im}(A_0) = -3.3(15) \times 10^{-11}\mathrm{GeV}. \tag{6.4}$$

Chapter 7

Conclusions and Discussions

In the previous two chapters, we showed detailed results for the kaon decay amplitudes from a $16^3 \times 32$ lattice and a $24^3 \times 64$ lattice, with $L_s = 16$ for the DWF action. These are all non-physical, threshold calculations. The kaons and pions have masses much heavier than their experimental values, and the decaying pions do not carry momentum. However, as a pioneering calculation on the difficult problem of calculating A_0 with disconnected graphs, our results have shown success of the lattice methodology of a direct treatment of the weak matrix elements. We can obtain quite accurate (statistical error only) result for $\mathrm{Re}(A_0)$ from a few hundreds of configurations. For $\mathrm{Im}(A_0)$, our calculation shows that it is much more difficult than other amplitudes. The number can only serve as an order of magnitude constrain, since it has over 50% error.

There are a few important things worth further discussion even though our calculation is performed with unphysical kinematics:

1. *Contributions to the decay amplitudes from different operators.* One can see that the kaon decays through the current-current operators predominately ($\sim 99\%$) by examining the our earlier results for $\mathrm{Re}(A_2)$ and $\mathrm{Re}(A_0)$. Table 11 and 18 show that the QCD penguin operators make no contribution, and electroweak penguin operators make approximately 1% contribution to the $\Delta I = 3/2$ channel decay. Table 14 and 21 show that QCD penguin operators make roughly 1%, and electroweak penguin operators make less then 0.1% contribution to the $\Delta I = 1/2$ channel.

   For the CP violating (imaginary part) decay amplitudes, which are at least 10,000 times smaller than the corresponding real parts receive all their contributions from the penguin operators as required by the standard model (the single complex phase in the CKM matrix elements V_{ub} and V_{td}). For $\mathrm{Im}(A_2)$, all contributions are from electroweak penguin operators (Tab.11 and 18). For $\mathrm{Im}(A_0)$, the QCD penguin operators make the predominate contribution, and the electro penguin operators only makes roughly 10% contribution(Tab.14 and 21).

2. *The importance of the disconnected graphs.* It has been very clear that the disconnected graphs are the major problem for the calculations with the isospin zero, $\pi - \pi$ state. While the signal decays exponentially with increasing time separation, the noise from the disconnected graphs remains constant because the lowest lying state is the vacuum state. The results without the disconnected graphs for A_0 in Tab.14 and 21 shows much more statistically accurate results. However, they agree with the full results including the disconnected graphs.

   The empirical OZI rule says that decays through the disconnected graph are

strong suppressed. The argument for this rule is that, if the graph is disconnected, the connecting gluons may be hard and therefore have weak quark-gluon coupling because of the asymptotic freedom of QCD. The good agreement of the full results and the results without the disconnected graphs for the decay amplitude A_0 demonstrate consistency with the OZI rule. If we could safely ignore the disconnected graphs, the results could be calculated with our method to a high accuracy relatively easily. However, this is not fully justified and there is no strict theoretical basis for us to ignore the disconnected graphs safely. There are cases where the disconnected graph can not be ignored. For example, our earlier $\eta - \eta'$ project [12] demonstrated that the disconnected graphs are extremely important to make the η' mass much heavier than the masses of the goldstone bosons and to give the correct mixing angle between the octet and singlet states.

3. $\Delta I = 1/2$ *rule.* Based on the results of the previous two chapters, we can examine the $\Delta I = 1/2$ rule for the ratio of $\mathrm{Re}(A_0)$ to $\mathrm{Re}(A_2)$ for a 877 MeV kaon decaying into two 422 MeV pions,

$$\frac{\mathrm{Re}(A_0)}{\mathrm{Re}(A_2)} = 9.1(21), \tag{7.1}$$

and a 662 MeV kaon to two 329 MeV pions,

$$\frac{\mathrm{Re}(A_0)}{\mathrm{Re}(A_2)} = 12.0(17). \tag{7.2}$$

Both of these results are clearly still far away from the experimental value of 22.5 because our calculation is far from physical kinematics. Actually, our results for A_0 are relatively close to experimental value, but A_2 is far off. The decay

amplitude A_2 depends on the kinematics in a very strong way [64]. Based on other's results on the calculation of A_2 [64, 13] with similar techniques that we used, the lattice results agree with experiment value very well for A_2. Our results indicate that A_0 depends on the kinematics in a weaker way so it could stay around the experimental value as the simulation gets close to the physical kinematics.

The factor of 12 we obtained is a already a large $\Delta I = 1/2$ enhancement effect, comparing to the argument from the Wilson coefficients evaluated around 2 GeV which explains only a factor of 2 enhancement [21, 22]. The major enhancement arises from the weak matrix elements, as we can see it from Tab.18 for $\Delta I = 3/2$ weak matrix elements and Tab.21 for $\Delta I = 1/2$ channel. The most important reason for us seeing this $\Delta I = 1/2$ enhancement comes from the addition of the contractions ① and ② in the $\Delta I = 1/2$ case and their cancellation in the $\Delta I = 3/2$ case. For example, based on Eq. 4.25, 4.26 and 4.28, keeping only the dominant current-current operator contributions, we have

$$A_{2,2}(t_\pi, t_{\rm op}, t_K) = i\sqrt{\frac{2}{3}}\{① + ②\}, \tag{7.3}$$

$$A_{0,2}(t_\pi, t_{\rm op}, t_K) \approx i\frac{1}{\sqrt{3}}\{2 \cdot ① - ②\}. \tag{7.4}$$

From Fig. 10, we know that contraction ② is the color mixing version of ①. Therefore, a naive argument would suggest that ② should have the same sign and equal one third of ①. If this were true, the two weak matrix elements should be roughly the same size. However, in the actual interacting world, we find that in fact they have opposite signs, as shown in Fig.45. They also have a similar size, which leads to strong cancellation for the amplitudes of $A_{2,2}$. Therefore,

the final weak matrix elements in the $\Delta I = 1/2$ channel is significantly larger than that of $\Delta I = 3/2$ channel for the current-current operators which make the largest contribution to the real part of the decay amplitdues. This explains the $\Delta I = 1/2$ rule. To see clearly how the relative size of contraction ② to contraction ① changes as the quark mass decreases, we calculate these graphs on the $16^3 \times 32$ lattice with both $m_l = 0.01$ and $m_l = 0.001$ (partially quenched). The corresponding pion masses are 422 MeV and 247 MeV respectively. The results are shown in Fig. 46. We can see that as the pion masses reduces, the relative size of the absolute value of ② gets much closer to ①. Therefore, there is a stronger cancellation for the amplitude of $M_2^{3/2}$, and a larger ratio for the $\Delta I = 1/2$ rule.

4. *Direct CP violation measure ϵ'.* For completeness, let us also calculate the direct CP violation measure ϵ' at the kinematics we have used. Based on equation

$$\mathrm{Re}\left(\frac{\epsilon'}{\epsilon}\right) = \frac{\omega}{\sqrt{2}|\epsilon|}\left[\frac{\mathrm{Im}(A_2)}{\mathrm{Re}(A_2)} - \frac{\mathrm{Im}(A_0)}{\mathrm{Re}(A_0)}\right], \tag{7.5}$$

the calculated value for a 877 MeV kaon to two 422 MeV pions is

$$\mathrm{Re}(\epsilon'/\epsilon) = (2.7 \pm 2.6) \times 10^{-3}, \tag{7.6}$$

and a 662 MeV kaon to two 329 MeV pions is

$$\mathrm{Re}(\epsilon'/\epsilon) = (2.0 \pm 1.7) \times 10^{-3}. \tag{7.7}$$

They have the same sign and are at the same order of magnitude as the experimental value $1.65(26) \times 10^{-3}$ even though they have an associated 100% error. The two terms in Eq. 7.5 have opposite sign so there are cancellations

which give the final result for ϵ' an even larger relative error. E.g, for the 662 MeV kaon case, $\mathrm{Im}(A_2)/\mathrm{Re}(A_2) = -0.2440(11) \times 10^{-4}$ and $\mathrm{Im}(A_0)/\mathrm{Re}(A_0) = -1.02(57) \times 10^{-4}$.

In the future, much work still must be done to calculate the physical value of the decay amplitude A_0. We must perform the calculation with a much larger lattice to allow us to access the physical pion mass. We could use the DSDR lattice configurations with which the $\Delta I = 3/2$ amplitudes with physical kinematics have been calculated [13]. A more difficult problem is to give physical relative momentum to the two pions. This can be accomplished while keeping the two-pion state in which we are interested as the ground state, if the kaon is given non-zero spatial momentum relative to the lattice. In this case the lowest energy final state can be arranged to have one pion at rest while the other pion carries the kaon momentum, as in the $\Delta I = 3/2$ calculation of Ref. [64]. However, this requires the momentum carried by the initial kaon and final pion to be 739 MeV, which is 5.4 times larger than the physical pion mass. Such a large spatial momentum will likely make the calculation extremely noisy. For the $\Delta I = 3/2$ calculation, it is possible to use anti-periodic boundary conditions in one or more spatial directions for one of the light quarks so that each pion necessarily carries the physical, 206 MeV momentum present in the actual decay while the kaon is at rest [14, 65, 13]. However, this approach cannot be used for the $I = 0$ final state being studied here. Instead, the use of G-parity boundary conditions [66, 67] may be the solution to this problem.

Appendix A

$k \to \pi\pi$ contractions

As we discussed in Section 4.2, there are 48 contractions in total that are shown in figure 10-13 and we label it with number from 1 to 48. We have expclicity explained a few examples already. In this appredix, we write down the specific expressions for each of the graphs from 1 to 48. In these expressions, $L(\vec{x}_{op}, t_{op}; t_\pi)$ stands for a light propagator with a Couloumb gauge fixed wall source at time $t = t_\pi$ and sink at space time point $(\vec{x}_{op}, t_{op})$. The same expression with symbol S stands for strange quark propagator. $L_w(t_{sink}, t_{src})$ stands for a light quark coulomb gauge fiexed wall source with coloumb gauge fixed wall sink propagator, so it is the same as $\sum_{\vec{x}_\pi} L((\vec{x}_\pi, t_\pi), t_K)$ that we use in Section 4.2. In the calculation of the type 3 and type 4 contractions, the fermion loop is evaluated using a random wall source. Therefore, in the following expressions, $L(\vec{x}_{op}, t_{op}; \vec{x}_{op}, t_{op})$ is replaced by $L^R(x_{\rm op}, t_{\rm op})\eta(x_{\rm op})^*$ in the actual calculation.

For the *type*4 contrations, we only show part of the expression for simplicity. The

actual result is calculated as follow

$$\langle ⓘ \cdot Tr\{L_w(t_\pi,t_\pi)L_w^\dagger(t_\pi,t_\pi)\}\rangle - \langle ⓘ\rangle\langle Tr\{L_w(t_\pi,t_\pi)L_w^\dagger(t_\pi,t_\pi)\}\rangle \tag{A.1}$$

where ⓘ is the expression shown below for i=33 to 48.

$$\begin{aligned}
①/③ &= \pm\sum_{\vec{x}_{op}}\{Tr\{\gamma_\mu(1\mp\gamma_5)L(\vec{x}_{op},t_{op};t_\pi)L^\dagger(\vec{x}_{op},t_{op};t_\pi)\}\\
&\quad\cdot Tr\{\gamma^\mu(1-\gamma_5)L(\vec{x}_{op},t_{op};t_\pi)\gamma_5 L_w(t_\pi,t_k)S^\dagger(\vec{x}_{op},t_{op};t_k)\}\}\\
②/④ &= \pm\sum_{\vec{x}_{op}}Tr_c\{Tr_s\{\gamma_\mu(1\mp\gamma_5)L(\vec{x}_{op},t_{op};t_\pi)L^\dagger(\vec{x}_{op},t_{op};t_\pi)\}\\
&\quad\cdot Tr_s\{\gamma^\mu(1-\gamma_5)L(\vec{x}_{op},t_{op};t_\pi)\gamma_5 L_w(t_\pi,t_k)S^\dagger(\vec{x}_{op},t_{op};t_k)\}\}\\
⑤/⑦ &= \pm\sum_{\vec{x}_{op}}Tr\{\gamma_\mu(1-\gamma_5)L(\vec{x}_{op},t_{op};t_\pi)L^\dagger(\vec{x}_{op},t_{op};t_\pi)\\
&\quad\cdot\gamma^\mu(1\mp\gamma_5)L(\vec{x}_{op},t_{op};t_\pi)\gamma_5 L_w(t_\pi,t_k)S^\dagger(\vec{x}_{op},t_{op};t_k)\}\\
⑥/⑧ &= \pm\sum_{\vec{x}_{op}}Tr_s\{Tr_c\{\gamma_\mu(1-\gamma_5)L(\vec{x}_{op},t_{op};t_\pi)L^\dagger(\vec{x}_{op},t_{op};t_\pi)\}\\
&\quad\cdot Tr_c\{\gamma^\mu(1\mp\gamma_5)L(\vec{x}_{op},t_{op};t_\pi)\gamma_5 L_w(t_\pi,t_k)S^\dagger(\vec{x}_{op},t_{op};t_k)\}\}\\
⑨/⑪ &= \pm\sum_{\vec{x}_{op}}\{Tr\{\gamma_\mu(1-\gamma_5)L(\vec{x}_{op},t_{op};t_k)S^\dagger(\vec{x}_{op},t_{op};t_k)\}\\
&\quad\cdot Tr\{\gamma^\mu(1\mp\gamma_5)L(\vec{x}_{op},t_{op};t_\pi)\gamma_5 L_w(t_\pi,t_\pi)L^\dagger(\vec{x}_{op},t_{op};t_\pi)\}\}\\
⑩/⑫ &= \pm\sum_{\vec{x}_{op}}Tr_c\{Tr_s\{\gamma_\mu(1-\gamma_5)L(\vec{x}_{op},t_{op};t_k)S^\dagger(\vec{x}_{op},t_{op};t_k)\}\\
&\quad\cdot Tr_s\{\gamma^\mu(1\mp\gamma_5)L(\vec{x}_{op},t_{op};t_\pi)\gamma_5 L_w(t_\pi,t_\pi)L^\dagger(\vec{x}_{op},t_{op};t_\pi)\}\}\\
⑬/⑮ &= \pm\sum_{\vec{x}_{op}}Tr\{\gamma_\mu(1\mp\gamma_5)L(\vec{x}_{op},t_{op};t_k)S^\dagger(\vec{x}_{op},t_{op};t_k)\\
&\quad\cdot\gamma^\mu(1-\gamma_5)L(\vec{x}_{op},t_{op};t_\pi)\gamma_5 L_w(t_\pi,t_\pi)L^\dagger(\vec{x}_{op},t_{op};t_\pi)\}\\
⑭/⑯ &= \pm\sum_{\vec{x}_{op}}Tr_s\{Tr_c\{\gamma_\mu(1\mp\gamma_5)L(\vec{x}_{op},t_{op};t_k)S^\dagger(\vec{x}_{op},t_{op};t_k)\}\\
&\quad\cdot Tr_c\{\gamma^\mu(1-\gamma_5)L(\vec{x}_{op},t_{op};t_\pi)\gamma_5 L_w(t_\pi,t_\pi)L^\dagger(\vec{x}_{op},t_{op};t_\pi)\}\}
\end{aligned}$$

$$
\begin{aligned}
⑰/⑲ &= \sum_{\vec{x}_{op}} \{Tr\{\gamma_\mu(1-\gamma_5)L(\vec{x}_{op},t_{op};t_\pi)L_w^\dagger(t_\pi,t_\pi)L_w(t_\pi,t_k)S^\dagger(\vec{x}_{op},t_{op};t_k)\} \\
&\quad \cdot Tr\{\gamma^\mu(1\mp\gamma_5)L(\vec{x}_{op},t_{op};\vec{x}_{op},t_{op})\}\} \\
⑱/⑳ &= \sum_{\vec{x}_{op}} Tr_c\{Tr_s\{\gamma_\mu(1-\gamma_5)L(\vec{x}_{op},t_{op};t_\pi)L_w^\dagger(t_\pi,t_\pi)L_w(t_\pi,t_k)S^\dagger(\vec{x}_{op},t_{op};t_k)\} \\
&\quad \cdot Tr_s\{\gamma^\mu(1\mp\gamma_5)L(\vec{x}_{op},t_{op};\vec{x}_{op},t_{op})\}\} \\
㉑/㉓ &= \sum_{\vec{x}_{op}} \{Tr\{\gamma_\mu(1-\gamma_5)L(\vec{x}_{op},t_{op};t_\pi)L_w^\dagger(t_\pi,t_\pi)L_w(t_\pi,t_k)S^\dagger(\vec{x}_{op},t_{op};t_k)\} \\
&\quad \cdot Tr\{\gamma^\mu(1\mp\gamma_5)S(\vec{x}_{op},t_{op};\vec{x}_{op},t_{op})\}\} \\
㉒/㉔ &= \sum_{\vec{x}_{op}} Tr_c\{Tr_s\{\gamma_\mu(1-\gamma_5)L(\vec{x}_{op},t_{op};t_\pi)L_w^\dagger(t_\pi,t_\pi)L_w(t_\pi,t_k)S^\dagger(\vec{x}_{op},t_{op};t_k)\} \\
&\quad \cdot Tr_s\{\gamma^\mu(1\mp\gamma_5)S(\vec{x}_{op},t_{op};\vec{x}_{op},t_{op})\}\} \\
㉕/㉗ &= \sum_{\vec{x}_{op}} Tr\{\gamma_\mu(1\mp\gamma_5)L(\vec{x}_{op},t_{op};t_\pi)L_w^\dagger(t_\pi,t_\pi)L_w(t_\pi,t_k)S^\dagger(\vec{x}_{op},t_{op};t_k) \\
&\quad \cdot\gamma^\mu(1-\gamma_5)L(\vec{x}_{op},t_{op};\vec{x}_{op},t_{op})\} \\
㉖/㉘ &= \sum_{\vec{x}_{op}} Tr_s\{Tr_c\{\gamma_\mu(1\mp\gamma_5)L(\vec{x}_{op},t_{op};t_\pi)L_w^\dagger(t_\pi,t_\pi)L_w(t_\pi,t_k)S^\dagger(\vec{x}_{op},t_{op};t_k)\} \\
&\quad \cdot Tr_c\{\gamma^\mu(1-\gamma_5)L(\vec{x}_{op},t_{op};\vec{x}_{op},t_{op})\}\} \\
㉙/㉛ &= \pm\sum_{\vec{x}_{op}} Tr\{\gamma_\mu(1-\gamma_5)L(\vec{x}_{op},t_{op};t_\pi)L_w^\dagger(t_\pi,t_\pi)L_w(t_\pi,t_k)S^\dagger(\vec{x}_{op},t_{op};t_k) \\
&\quad \cdot\gamma^\mu(1\mp\gamma_5)S(\vec{x}_{op},t_{op};\vec{x}_{op},t_{op})\} \\
㉚/㉜ &= \pm\sum_{\vec{x}_{op}} Tr_s\{Tr_c\{\gamma_\mu(1-\gamma_5)L(\vec{x}_{op},t_{op};t_\pi)L_w^\dagger(t_\pi,t_\pi)L_w(t_\pi,t_k)S^\dagger(\vec{x}_{op},t_{op};t_k)\} \\
&\quad \cdot Tr_c\{\gamma^\mu(1\mp\gamma_5)S(\vec{x}_{op},t_{op};\vec{x}_{op},t_{op})\}\}
\end{aligned}
$$

$$
\begin{aligned}
㉝/㉟ &= \sum_{\vec{x}_{op}} \{Tr\{\gamma_\mu(1-\gamma_5)L(\vec{x}_{op},t_{op};t_k)S^\dagger(\vec{x}_{op},t_{op};t_k)\} \\
&\quad \cdot Tr\{\gamma^\mu(1\mp\gamma_5)L(\vec{x}_{op},t_{op};\vec{x}_{op},t_{op})\}\} \\
㉞/㊱ &= \sum_{\vec{x}_{op}} Tr_c\{Tr_s\{\gamma_\mu(1-\gamma_5)L(\vec{x}_{op},t_{op};t_k)S^\dagger(\vec{x}_{op},t_{op};t_k)\} \\
&\quad \cdot Tr_s\{\gamma^\mu(1\mp\gamma_5)L(\vec{x}_{op},t_{op};\vec{x}_{op},t_{op})\}\} \\
㊲/㊴ &= \sum_{\vec{x}_{op}} \{Tr\{\gamma_\mu(1-\gamma_5)L(\vec{x}_{op},t_{op};t_k)S^\dagger(\vec{x}_{op},t_{op};t_k)\} \\
&\quad \cdot Tr\{\gamma^\mu(1\mp\gamma_5)S(\vec{x}_{op},t_{op};\vec{x}_{op},t_{op})\}\} \\
㊳/㊵ &= \sum_{\vec{x}_{op}} Tr_c\{Tr_s\{\gamma_\mu(1-\gamma_5)L(\vec{x}_{op},t_{op};t_k)S^\dagger(\vec{x}_{op},t_{op};t_k)\} \\
&\quad \cdot Tr_s\{\gamma^\mu(1\mp\gamma_5)S(\vec{x}_{op},t_{op};\vec{x}_{op},t_{op})\}\} \\
㊶/㊸ &= \sum_{\vec{x}_{op}} Tr\{\gamma_\mu(1\mp\gamma_5)L(\vec{x}_{op},t_{op};t_k)S^\dagger(\vec{x}_{op},t_{op};t_k) \\
&\quad \cdot \gamma^\mu(1-\gamma_5)L(\vec{x}_{op},t_{op};\vec{x}_{op},t_{op})\} \\
㊷/㊹ &= \sum_{\vec{x}_{op}} Tr_s\{Tr_c\{\gamma_\mu(1\mp\gamma_5)L(\vec{x}_{op},t_{op};t_k)S^\dagger(\vec{x}_{op},t_{op};t_k)\} \\
&\quad \cdot Tr_c\{\gamma^\mu(1-\gamma_5)L(\vec{x}_{op},t_{op};\vec{x}_{op},t_{op})\}\} \\
㊺/㊼ &= \pm\sum_{\vec{x}_{op}} Tr\{\gamma_\mu(1-\gamma_5)L(\vec{x}_{op},t_{op};t_k)S^\dagger(\vec{x}_{op},t_{op};t_k) \\
&\quad \cdot \gamma^\mu(1\mp\gamma_5)S(\vec{x}_{op},t_{op};\vec{x}_{op},t_{op})\} \\
㊻/㊽ &= \pm\sum_{\vec{x}_{op}} Tr_s\{Tr_c\{\gamma_\mu(1-\gamma_5)L(\vec{x}_{op},t_{op};t_k)S^\dagger(\vec{x}_{op},t_{op};t_k)\} \\
&\quad \cdot Tr_c\{\gamma^\mu(1\mp\gamma_5)S(\vec{x}_{op},t_{op};\vec{x}_{op},t_{op})\}\}
\end{aligned}
$$

Bibliography

[1] S. Li, *Kaon matrix elements and CP violation from lattice QCD with 2+1 flavors of domain wall fermions*, Ph.D. thesis, Columbia University (2008), aAT-3333388.

[2] T. D. Lee and C. N. Yang, Phys. Rev. **104**, 254 (1956).

[3] C. S. Wu, E. Ambler, R. W. Hayward, D. D. Hoppes, and R. P. Hudson, Phys. Rev. **105**, 1413 (1957).

[4] J. H. Christenson, J. W. Cronin, V. L. Fitch, and R. Turlay, Phys. Rev. Lett. **13**, 138 (1964).

[5] V. Fanti *et al.* (NA48 Collaboration), Phys.Lett. **B465**, 335 (1999), hep-ex/9909022.

[6] B. Aubert *et al.* (BaBar Collaboration), Phys.Rev.Lett. **93**, 131801 (2004), hep-ex/0407057.

[7] K. Nakamura *et al.* (Particle Data Group), J.Phys.G **G37**, 075021 (2010).

[8] C. Bernard and A. Soni, Nuclear Physics B - Proceedings Supplements **9**(0), 155 (1989), ISSN 0920-5632.

[9] T. Blum, P. Chen, N. Christ, C. Cristian, C. Dawson, G. Fleming, R. Mawhinney, S. Ohta, G. Siegert, A. Soni, P. Vranas, M. Wingate, *et al.*, Phys. Rev. D **68**, 114506 (2003).

[10] S. Li and N. H. Christ, PoS **LATICE 2008**, 272 (2008), 0812.1368.

[11] J. Laiho and R. S. Van de Water, PoS **LATTICE2010**, 312 (2010), 1011.4524.

[12] N. Christ, C. Dawson, T. Izubuchi, C. Jung, Q. Liu, *et al.*, Phys.Rev.Lett. **105**, 241601 (2010), 1002.2999.

[13] T. Blum, P. Boyle, N. Christ, N. Garron, E. Goode, *et al.* (2011), 1111.1699.

[14] C. Kim, Nucl. Phys. Proc. Suppl. **129**, 197 (2004), hep-lat/0311003.

[15] C. T. Sachrajda and G. Villadoro, Phys. Lett. **B609**, 73 (2005), hep-lat/0411033.

[16] G. Martinelli, C. Pittori, C. T. Sachrajda, M. Testa, and A. Vladikas, Nucl. Phys. **B445**, 81 (1995), hep-lat/9411010.

[17] C. Lehner and C. Sturm (2011), 1104.4948.

[18] G. Buchalla, A. J. Buras, and M. E. Lautenbacher, Rev. Mod. Phys. **68**, 1125 (1996), hep-ph/9512380.

[19] T. P. Cheng and L. F. Li, *Gauge Theory of Elementary Particle Physics* (Oxford University Press, 2008), 1 ed.

[20] J. Yu (2011), 1111.6953.

[21] M. Gaillard and B. W. Lee, Phys.Rev.Lett. **33**, 108 (1974).

[22] G. Altarelli and L. Maiani, Phys.Lett. **B52**, 351 (1974).

[23] J. J. Sakurai, *Modern Quantum Mechanics* (Pearson Education, 2005), revised ed.

[24] K. G. Wilson, Phys. Rev. D **10**, 2445 (1974).

[25] Y. Iwasaki and T. Yoshie, Physics Letters B **143**(4-6), 449 (1984), ISSN 0370-2693.

[26] Y. and Iwasaki, Nuclear Physics B **258**(0), 141 (1985), ISSN 0550-3213.

[27] T. Takaishi, Phys. Rev. D **54**, 1050 (1996).

[28] H. J. Rothe, *Lattice Gauge Theories* (World Scientific Publishing Co. Pte. Ltd, 2006), 3rd ed.

[29] J. B. Kogut and L. Susskind, Phys. Rev. **D11**, 395 (1975).

[30] B. Bunk, M. Della Morte, K. Jansen, and F. Knechtli, Nucl.Phys. **B697**, 343 (2004), hep-lat/0403022.

[31] A. Hart and E. Muller, Phys.Rev. **D70**, 057502 (2004), hep-lat/0406030.

[32] H. Nielsen and M. Ninomiya, Physics Letters B **105**(2-3), 219 (1981), ISSN 0370-2693.

[33] P. H. Ginsparg and K. G. Wilson, Phys. Rev. D **25**, 2649 (1982).

[34] R. Narayanan and H. Neuberger, Phys. Rev. Lett. **71**, 3251 (1993).

[35] Y. Shamir, Nucl. Phys. **B406**, 90 (1993), hep-lat/9303005.

[36] V. Furman and Y. Shamir, Nucl. Phys. **B439**, 54 (1995), hep-lat/9405004.

[37] D. J. Antonio, T. Blum, K. C. Bowler, P. A. Boyle, N. H. Christ, S. D. Cohen, M. A. Clark, C. Dawson, A. Hart, K. Hashimoto, T. Izubuchi, B. Joó, *et al.* (RBC Collaboration and UKQCD Collaboration), Phys. Rev. D **75**, 114501 (2007).

[38] M. A. Clark, *The Rational Hybrid Monte Carlo Algorithm*, Ph.D. thesis, The University of Edinburgh (2005).

[39] M. Hasenbusch, Physics Letters B **519**(1-2), 177 (2001), ISSN 0370-2693.

[40] A. Kennedy and M. Clark, PoS **LAT2007**, 038 (2007), 0710.3611.

[41] H. Yin and R. D. Mawhinney, PoS **LATTICE2011**, 051 (2011), 1111.5059.

[42] M. Luscher and U. Wolff, Nuclear Physics B **339**(1), 222 (1990), ISSN 0550-3213.

[43] B. Blossier, G. von Hippel, T. Mendes, R. Sommer, and M. Della Morte, PoS **LATTICE2008**, 135 (2008), 0808.1017.

[44] J. J. Dudek, R. G. Edwards, N. Mathur, and D. G. Richards, Phys. Rev. D **77**, 034501 (2008).

[45] S. Durr, Z. Fodor, J. Frison, C. Hoelbling, R. Hoffmann, S. D. Katz, S. Krieg, T. Kurth, L. Lellouch, T. Lippert, K. K. Szabo, and G. Vulvert, Science **322**(5905), 1224 (2008).

[46] T. Blum, P. Chen, N. H. Christ, C. Cristian, C. Dawson, *et al.*, Phys.Rev. **D69**, 074502 (2004), hep-lat/0007038.

[47] G. L. G. Sleijpen and D. R. Forkkema, Electronic Transactions on Numerical Analysis **1**, 11 (1993).

[48] M. Luscher, JHEP **0707**, 081 (2007), 0706.2298.

[49] A. Stathopoulos and K. Orginos, SIAM J. Sci. Comput. **32**, 439 (2010), 0707.0131.

[50] W. H. Press, S. A. Teukolsky, W. T. Vetterling, and B. P. Flannery, *Numerical Recipes* (Cambridge University Press, 2007), 3rd ed.

[51] M. Luscher, Nuclear Physics B **354**, 531 (1991).

[52] T. Yamazaki, S. Aoki, M. Fukugita, K.-I. Ishikawa, N. Ishizuka, Y. Iwasaki, K. Kanaya, T. Kaneko, Y. Kuramashi, M. Okawa, A. Ukawa, and T. Yoshié (CP-PACS Collaboration), Phys. Rev. D **70**, 074513 (2004).

[53] L. Lellouch and M. Luscher, Commun.Math.Phys. **219**, 31 (2001), hep-lat/0003023.

[54] T. Blum *et al.* (RBC), Phys. Rev. **D68**, 114506 (2003), hep-lat/0110075.

[55] L. Maiani and M. Testa, Physics Letters B **245**(3-4), 585 (1990), ISSN 0370-2693.

[56] Y. Aoki *et al.*, Phys. Rev. **D78**, 054510 (2008), 0712.1061.

[57] T. Blum, P. Boyle, N. Christ, N. Garron, E. Goode, *et al.*, Phys.Rev. **D84**, 114503 (2011), 40 pages, 12 figures, 1106.2714.

[58] C. Sturm *et al.*, Phys. Rev. **D80**, 014501 (2009), 0901.2599.

[59] C. Allton *et al.* (RBC and UKQCD), Phys. Rev. **D76**, 014504 (2007), hep-lat/0701013.

[60] C. Allton *et al.* (RBC-UKQCD), Phys. Rev. **D78**, 114509 (2008), 0804.0473.

[61] L. Giusti, C. Hoelbling, M. Luscher, and H. Wittig, Comput.Phys.Commun. **153**, 31 (2003), hep-lat/0212012.

[62] M. Lightman (RBC), PoS **LATTICE2008**, 273 (2008), 0906.1847.

[63] J. I. Noaki *et al.* (CP-PACS), Phys. Rev. **D68**, 014501 (2003), hep-lat/0108013.

[64] T. Yamazaki (RBC and UKQCD Collaborations), Phys. Rev. D **79**, 094506 (2009).

[65] E. J. Goode and M. Lightman, PoS **LATTICE2010**, 313 (2010), 1101.2473.

[66] C.-h. Kim and N. H. Christ, Nucl. Phys. Proc. Suppl. **119**, 365 (2003), hep-lat/0210003.

[67] C. Kim and N. H. Christ, PoS **LAT2009**, 255 (2009), 0912.2936.

Tables

parameter	value
V_{ud}	0.97425
V_{us}	0.2252
$\tau = -\frac{V_{ts}^* V_{td}}{V_{ud} V_{us}^*}$	$0.0014148 - i0.0005558$
G_F	$1.16637 \times 10^{-5} GeV$
$\hbar c$	0.1973269631 GeV·fm
$\alpha_s(M_z)$	0.1184
M_Z	91.1876 GeV
M_W	80.399 GeV
$\sin^2 \theta_W$	0.23116
M_t	170.0 GeV
$m_b(m_b)$	4.19 GeV
$m_c(m_c)$	1.27 GeV
α	1/128.0

Table 1: Physical Constants that we used in this thesis. All values are from 2010 PDG book.

Meson	mass
K^+	0.493677(16) GeV
K^0	0.497614(24) GeV
$\pi^\pm$	0.13957018(35) GeV
π^0	0.1349766(6) GeV
Life time	value
K^+, τ_{K^+}	$1.2380(21) \times 10^{-8}$ s
K_S, τ_{K_S}	$0.8953(5) \times 10^{-10}$ s
Decay modes Fraction	value
$K^+ \to \pi^+\pi^0$	20.66(8)%
$K_S \to \pi^0\pi^0$	30.69(5)%
$K_S \to \pi^+\pi^-$	69.20(5)%

Table 2: Experimental value for the parameters used in the calculation of $\mathrm{Re}(A_0)$ and $\mathrm{Re}(A_2)$. All values are from 2010 PDG book.

Lattice	m_π	CG	$N_{low}(N_{prop})$	Memory	EigCG	speedup
$16^3 \times 32 \times 16$	421 MeV	1560	120(1)	12 GB	320	4.9
$16^3 \times 32 \times 16$	204* MeV	3000	120(1)	12 GB	350	8.6
$24^3 \times 64 \times 16$	330 MeV	2900	400(4)	272 GB	530	5.5
$32^3 \times 64 \times 32$	180 MeV	10400	600(5)	2 TB	1480	7.0

Table 3: The speedup from EigCG algorithm on different lattices. N_{prop} stands for the number of propagator solves to get the required number of low modes N_{low}. While the EigCG is accumulating the low modes informaiton, each CG iteration becomes roughly 60% harder supposing the EigCG part runs at the same speed(efficiency) as the normal CG part (application of the dirac operator). The symbol $*$ means that it is a quenched calculation.

i	$y_i^{\overline{MS}}(\mu)$	$z_i^{\overline{MS}}(\mu)$
1	0	-0.29829
2	0	1.14439
3	0.024141	-0.00243827
4	-0.058121	0.00995157
5	0.0102484	-0.00110544
6	-0.069971	0.00657457
7	-0.000211182	0.0000701587
8	0.000779244	-0.0000899541
9	-0.0106787	0.0000150176
10	0.0029815	0.0000656482

Table 4: Wilson Coefficients in the $\overline{MS}$ scheme, at energy scale $\mu = 2.15$GeV.

L	$m_\pi L$	δ_1	δ_2	δ	err(%)
128	25.1	-0.046328	-0.0451707	-0.0450021	0.37
96	18.8	-0.070813	-0.0690452	-0.0677210	1.91
64	12.5	-0.124959	-0.121848	-0.1105385	9.28
48	9.4	-0.18029	-0.175822	-0.1413469	19.6
32	6.3	-0.28312	-0.276195	-0.1676799	39.2
128	70.3	-0.0098427	-0.0095966	-0.00955435	0.44
96	52.7	-0.0151625	-0.0147834	-0.01471830	0.44
64	35.1	-0.0278803	-0.0271834	-0.02705633	0.47
48	26.4	-0.0429078	-0.0418357	-0.04153803	0.71
32	17.6	-0.0779429	-0.0759975	-0.07366346	3.07

Table 5: Checking Lüscher's formula Eq. 4.9 for the scattering length. The Yukawa interaction coupling strength is set to 0.05. The upper half table is the result with m_π=142.7 MeV, and the lower half table is the result with m_π=400 MeV. δ_1 is the result from the first order Born approximation, and δ_2 is the result up to the second order Born approximation. δ is calculated based on Lüscher's formula 4.9. The relative error is calculated as $100 \times (\delta - \delta_2)/\delta_2$.

	1	2	3	4	5	6	7
1	1.20651(78)	0	0	0	0	0.00275(18)	-0.000387(86)
2	0	1.170(35)	0.151(30)	0.016(15)	0.0169(93)	-0.0014(26)	0.0006(23)
3	0	0.111(10)	1.0736(97)	0.0130(48)	-0.0120(48)	-0.00167(99)	-0.0003(10)
4	0	0.258(99)	0.123(86)	1.117(43)	0.258(28)	-0.0005(94)	-0.0048(79)
5	0	0.059(45)	-0.071(50)	0.118(21)	1.427(22)	0.0033(78)	-0.009(11)
6	0.000359(23)	-0.0037(33)	-0.0036(33)	-0.0005(13)	-0.0012(17)	1.07044(91)	0.2388(20)
7	0.000084(20)	0.0070(55)	0.0073(57)	-0.0011(29)	-0.0012(50)	0.0923(15)	1.4868(51)
1	1.20651(78)	0	0	0	0	0	0
2	0	1.192(32)	0.163(27)	0.016(14)	0.009(10)	0	0
3	0	0.118(10)	1.076(11)	0.0155(46)	-0.0148(51)	0	0
4	0	0.315(94)	0.154(79)	1.124(42)	0.226(30)	0	0
5	0	0.102(44)	-0.051(45)	0.128(19)	1.399(22)	0	0
6	0	0	0	0	0	1.07035(59)	0.23623(65)
7	0	0	0	0	0	0.09358(34)	1.4827(16)
1	1.20651(78)	0	0	0	0	0.00275(18)	-0.000387(86)
2	0	1.170(35)	0.151(30)	0.016(15)	0.0170(93)	-0.0014(26)	0.0006(23)
3	0	0.115(10)	1.0819(98)	0.0125(48)	-0.0086(49)	-0.00168(100)	-0.0003(10)
4	0	0.261(99)	0.129(85)	1.116(43)	0.261(28)	-0.0006(93)	-0.0050(80)
5	0	0.076(45)	-0.039(50)	0.116(21)	1.443(22)	0.0029(78)	-0.009(11)
6	0.000359(23)	-0.0038(32)	-0.0038(34)	-0.0005(13)	-0.0017(17)	1.07049(85)	0.2388(20)
7	0.000084(20)	0.0067(52)	0.0066(59)	-0.0010(30)	-0.0027(50)	0.0925(15)	1.4871(50)
1	1.20651(78)	0	0	0	0	0	0
2	0	1.192(32)	0.163(27)	0.016(14)	0.009(10)	0	0
3	0	0.123(10)	1.084(11)	0.0150(46)	-0.0114(52)	0	0
4	0	0.318(93)	0.160(79)	1.124(42)	0.228(30)	0	0
5	0	0.118(44)	-0.020(45)	0.126(19)	1.412(21)	0	0
6	0	0	0	0	0	1.07035(59)	0.23623(65)
7	0	0	0	0	0	0.09358(34)	1.4827(16)

Table 6: The matrix MF^{-1} calculated with $(ap)^2 = 1.542$, or $\mu = 2.15$ GeV, on the $m_l = 0.01$ lattice (25 configurations) . There are four tables: the upper two tables (parity-even and parity-odd) do not include subtraction, and the lower two(parity-even and odd) include the subtraction of operators B_1, B_2 and B_3. Notice that the matrix elements that are less than 10^{-6} are shown as 0.

	1	2	3	4	5	6	7
1	1.18039(90)	0	0	0	0	0.00412(32)	-0.00080(11)
2	0	1.019(57)	0.068(50)	-0.024(19)	0.027(11)	0.0043(30)	-0.0002(28)
3	0	0.052(21)	1.028(24)	-0.0009(66)	-0.0205(62)	-0.0003(22)	0.0004(20)
4	0	-0.16(19)	-0.07(17)	1.010(55)	0.288(38)	-0.0048(90)	0.0093(93)
5	0	-0.11(11)	-0.18(12)	0.087(31)	1.460(30)	-0.0008(77)	0.013(15)
6	0.000530(37)	0.0044(47)	0.0046(62)	-0.0047(19)	0.0014(25)	1.0574(14)	0.2562(21)
7	0.000129(36)	0.0144(71)	0.0145(96)	0.0002(36)	0.0075(65)	0.0777(21)	1.5731(52)
1	1.18040(90)	0	0	0	0	0	0
2	0	1.026(54)	0.081(48)	-0.022(18)	0.038(12)	0	0
3	0	0.049(20)	1.039(23)	-0.0054(68)	-0.0119(66)	0	0
4	0	-0.16(18)	-0.04(16)	0.993(54)	0.340(37)	0	0
5	0	-0.087(95)	-0.13(11)	0.083(23)	1.515(26)	0	0
6	0	0	0	0	0	1.05517(73)	0.25815(76)
7	0	0	0	0	0	0.07733(43)	1.5773(20)
1	1.18039(90)	0	0	0	0	0.00412(32)	-0.00080(11)
2	0	1.019(57)	0.068(50)	-0.024(19)	0.027(11)	0.0043(30)	-0.0002(28)
3	0	0.057(21)	1.039(24)	-0.0015(66)	-0.0170(62)	-0.0004(22)	0.0005(20)
4	0	-0.16(19)	-0.05(17)	1.009(54)	0.293(38)	-0.0052(89)	0.0086(91)
5	0	-0.09(11)	-0.13(12)	0.085(30)	1.480(30)	-0.0022(76)	0.011(14)
6	0.000530(37)	0.0031(48)	0.0029(60)	-0.0048(19)	0.0003(25)	1.0576(14)	0.2566(21)
7	0.000129(36)	0.0104(71)	0.0097(91)	0.0000(35)	0.0041(65)	0.0783(20)	1.5743(52)
1	1.18040(90)	0	0	0	0	0	0
2	0	1.026(54)	0.081(48)	-0.022(18)	0.038(12)	0	0
3	0	0.054(20)	1.049(23)	-0.0061(68)	-0.0081(65)	0	0
4	0	-0.16(18)	-0.03(16)	0.993(54)	0.343(37)	0	0
5	0	-0.067(94)	-0.09(11)	0.080(23)	1.529(25)	0	0
6	0	0	0	0	0	1.05517(73)	0.25815(76)
7	0	0	0	0	0	0.07733(43)	1.5773(20)

Table 7: The same setup as the previous table 6 except that $(ap)^2 = 1.234$ or $\mu = 1.92$ GeV.

	1	2	3	4	5	6	7
1	1.20648(63)	0	0	0	0	0.00512(16)	-0.000435(50)
2	0	1.053(40)	0.080(31)	-0.012(13)	0.0052(81)	0.0016(15)	0.0037(15)
3	0	0.076(15)	1.055(13)	-0.0023(45)	-0.0172(28)	-0.00051(57)	0.00110(72)
4	0	-0.07(13)	-0.05(11)	1.001(38)	0.231(23)	0.0030(37)	0.0202(59)
5	0	-0.069(56)	-0.108(53)	0.082(16)	1.402(16)	0.0041(32)	0.0263(66)
6	0.000644(20)	0.0026(18)	0.0020(21)	0.00038(73)	0.00322(93)	1.07118(69)	0.2305(11)
7	0.000185(12)	0.0032(36)	0.0016(44)	0.0021(16)	0.0092(27)	0.09347(94)	1.4670(28)
1	1.20647(63)	0	0	0	0	0	0
2	0	1.054(40)	0.079(31)	-0.014(13)	0.0093(76)	0	0
3	0	0.076(14)	1.054(12)	-0.0035(44)	-0.0150(27)	0	0
4	0	-0.07(13)	-0.05(11)	0.999(36)	0.252(21)	0	0
5	0	-0.072(53)	-0.121(47)	0.091(14)	1.420(12)	0	0
6	0	0	0	0	0	1.07073(47)	0.23473(50)
7	0	0	0	0	0	0.09391(37)	1.4789(13)

Table 8: The matrix MF^{-1} calculated with $(ap)^2 = 1.542$, or $\mu = 2.15$ GeV, on the $m_l = 0.02$ lattice (25 configurations). It includes the subtraction of operators B_1, B_2 and B_3. It includes two sub-tables. The top table is from the parity-even part (VV,AA terms). The bottom table is from the parity-odd part (VA, AV, terms). Notice that the matrix elements that are less than 10^{-6} are shown as 0.

	1	2	3	4	5	6	7
1	0.825(7)	0.	0.	0.	0.	0.	0.
2	0.	0.882(38)	-0.111(41)	-0.009(12)	0.010(10)	0.	0.
3	0.	-0.029(69)	0.962(92)	0.013(22)	-0.011(25)	0.	0.
4	0.	-0.04(12)	-0.01(13)	0.924(42)	-0.149(35)	0.	0.
5	0.	0.17(18)	0.08(23)	-0.042(55)	0.649(63)	0.	0.
6	0.	0.	0.	0.	0.	0.943(8)	-0.154(9)
7	0.	0.	0.	0.	0.	-0.0636(53)	0.680(11)

Table 9: The renormalization matrix $Z^{\mathrm{lat}\to\mathrm{RI}}/Z_q^2$ in the seven operator chiral basis at the energy scale $\mu = 2.15$ GeV. These values were obtained from Ref. [1] by performing an error weighted average of the values given in Tabs. 40, 41 and 42 (corresponding to bare quark masses of 0.01, 0.02 and 0.03) and inverting the resulting matrix with an uncorrelated propagation of the errors. Since the results given in these three tables are equal within errors, we chose to combine them to reduce their statistical errors rather than to perform a chiral extrapolation.

m_π	$E_0^{\pi\pi}$	$E_0^{\pi\pi\prime}$	$E_2^{\pi\pi}$	$m_K^{(0)}$	$m_K^{(1)}$	$m_K^{(2)}$
0.24373(47)	0.443(13)	0.4393(41)	0.5066(11)	0.42599(42)	0.50729(44)	0.64540(49)

Table 10: Masses of pion and kaons and energies of the two-pion states from the $16^3 \times 32$ lattice. Here the subscript $I = 0$ or 2 on the $\pi - \pi$ energy, $E_I^{\pi\pi}$, labels the isospin of the state and $E_0^{\pi\pi\prime}$ represents the isospin zero, two-pion energy obtained when the disconnected graph V is ignored. The superscript (0), (1) or (2) on the kaon mass distinguishes our three choices of valence strange quark mass, $m_s = 0.066$, 0.099 and 0.165 respectively.

i	$M_i^{3/2,\mathrm{lat}}(\times 10^{-2})$	Re(A_2)(GeV)	Im(A_2)(GeV)
1	0.4892(16)	-1.737(11)e-08	0
2	$= M_1$	6.665(42)e-08	0
7	6.080(18)	2.422(16)e-11	4.070(26)e-14
8	21.26(6)	-1.979(13)e-10	-9.646(61)e-13
9	$=1.5M_1$	-7.917(50)e-15	5.185(24)e-13
10	$=1.5M_1$	6.103(38)e-12	-1.448(9)e-13
Total	-	4.911(31)e-08	-5.502(40)e-13

Table 11: Results for the lattice $\Delta I = 3/2$, $K \to \pi\pi$ transition amplitudes obtained from fitting the 3-point correlation functions to the functional form given in Eq. 4.37 for the six operators with $\Delta I = 3/2$ components on the $16^3 \times 32$ lattice ensemble. The second column gives the lattice matrix elements $M_i^{3/2,\mathrm{lat}}(\times 10^{-2})$ while the third and fourth column give their contributions to the real and imaginary parts of A_2.

p	$q\frac{\partial\phi(q)}{\partial q}$	$p\frac{\partial\delta(p)}{\partial p}$	F
0.0690(13)	0.221(10)	-0.0849(43)	26.01(18)

Table 12: The calculated quantities which appear in the Lellouch-Lüscher factor F for $I = 2$. The corresponding factor for the case of non-interacting particles is $F_{\mathrm{free}} = 31.42$. The difference reflects the final two-pion scattering in a box. These results are from the $16^3 \times 32$ lattice ensemble.

m_K	$\mathrm{Re}(A_2)(\times 10^{-8})$	$\mathrm{Im}(A_2)(\times 10^{-12})$
$m_K^{(0)}$	4.308(28)	-0.5596(40)
$m_K^{(1)}$	4.911(31)	-0.5502(40)
$m_K^{(2)}$	5.916(38)	-0.5316(39)

Table 13: The complex, $K^0 \to \pi\pi$, $\Delta I = 3/2$ decay amplitudes in units of GeV. These results are from the $16^3 \times 32$ lattice ensemble.

i	$M_i^{1/2,\mathrm{lat}}(\times 10^{-2})$	$M_i'^{1/2,\mathrm{lat}}(\times 10^{-2})$	$\mathrm{Re}(A_0)(\mathrm{GeV})$	$\mathrm{Im}(A_0)(\mathrm{GeV})$
1	-1.6(16)	-1.10(37)	7.6(64)e-08	0
2	1.52(61)	1.92(15)	2.86(97)e-07	0
3	-0.3(41)	0.3(10)	2.1(136)e-10	1.1(76)e-12
4	2.7(33)	3.32(78)	4.2(44)e-09	1.4(14)e-11
5	-3.3(38)	-6.81(86)	3.1(53)e-10	1.6(28)e-12
6	-7.8(48)	-19.6(9)	-5.6(33)e-09	-3.3(20)e-11
7	10.9(14)	15.20(42)	5.2(12)e-11	8.8(20)e-14
8	35.7(28)	47.2(10)	-3.66(28)e-10	-1.79(14)e-12
9	-2.2(12)	-1.79(29)	3.1(15)e-14	-2.01(96)e-12
10	0.9(12)	1.24(29)	1.2(11)e-11	-2.7(27)e-13
Total	-	-	3.46(78)e-07	-2.4(23)e-11

Table 14: Fitted results for the weak, $\Delta I = 1/2$ kaon decay matrix elements using the kaon mass $m_K^{(0)}$ from the $16^3 \times 32$ lattice ensemble. The column M_i^{lat} shows the complete result from each operator. The column $M_i'^{\mathrm{lat}}$ shows the result when the disconnected graphs are omitted while the 4th and 5th columns show the contributions of each operator to the real and imaginary parts of the physical decay amplitude A_0. These results are obtained using a source-sink separation $\Delta = 16$, and a fit range $5 \leq t \leq 11$.

m_K	$\mathrm{Re}(A_0)(\times 10^{-8})$	$\mathrm{Re}(A_0')(\times 10^{-8})$	$\mathrm{Im}(A_0)(\times 10^{-12})$	$\mathrm{Im}(A_0')(\times 10^{-12})$
$m_K(0)$	36.1(78)	42.3(20)	-21(21)	-66.1(43)
$m_K(1)$	45(10)	48.8(24)	-41(26)	-74.6(47)
$m_K(2)$	65(15)	58.6(32)	-69(39)	-89.6(63)
-	38.0(82)	43.4(21)	-25(22)	-67.5(44)

Table 15: Amplitudes for $\Delta I = 1/2$ $K^0 \to \pi\pi$ decay in units of GeV. The last row is the energy conserving amplitudes that are obtained by a simple linear interpolation between $m_K^{(0)}$=0.42599 and $m_K^{(1)}$=0.50729 to the energy of two-pion state. As in the previous tables, the $'$ indicates results from which the disconnected graphs have been omitted. These results are from the $16^3 \times 32$ lattice ensemble.

m_π	$E_0^{\pi\pi}$	$E_0^{\pi\pi\prime}$	$E_2^{\pi\pi}$	m_K
0.19043(36)	0.3637(55)	0.3604(10)	0.38597(75)	0.38255(37)

Table 16: Masses of pion and kaons and energies of the two-pion states from the $24^3 \times 64$ lattice. Here the subscript $I = 0$ or 2 on the $\pi - \pi$ energy, $E_I^{\pi\pi}$, labels the isospin of the state and $E_0^{\pi\pi\prime}$ represents the isospin zero, two-pion energy obtained when the disconnected graph V is ignored. All the $\pi - \pi$ energies are calculated with $\pi - \pi$ separation of $\delta = 4$.

δ	$E_0^{\pi\pi}$	$E_0^{\pi\pi\prime}$	$E_2^{\pi\pi}$
0	0.3922(126)	0.3619(32)	0.3863(8)
2	0.3720(62)	0.3600(10)	0.3861(8)
4	0.3637(55)	0.3604(10)	0.3860(8)

Table 17: Fitted $\pi - \pi$ energy with a separation of the two pion sources $\delta = 0$, 2, and 4.

i	$M_i^{3/2,\mathrm{lat}}(\times 10^{-2})$	Re(A_2)(GeV)	Im(A_2)(GeV)
1	0.1960(7)	-9.461(49)e-09	0
2	$= M_1$	3.630(19)e-08	0
7	4.299(13)	2.433(12)e-11	4.089(21)e-14
8	14.54(5)	-1.937(9)e-10	-8.954(44)e-13
9	$=1.5M_1$	-4.311(22)e-15	2.824(15)e-13
10	$=1.5M_1$	3.324(17)e-12	-7.884(41)e-14
Total	-	2.668(14)e-08	-6.509(34)e-13

Table 18: Results for the lattice $\Delta I = 3/2$, $K \to \pi\pi$ transition amplitudes obtained from fitting the 3-point correlation functions to the functional form given in Eq. 4.37 for the six operators with $\Delta I = 3/2$ components from the $24^3 \times 64$ lattice. The second column gives the lattice matrix elements $M_i^{3/2,\mathrm{lat}}(\times 10^{-2})$ while the third and fourth column give their contributions to the real and imaginary parts of A_2. These results are fitted from the correlation function with $\Delta = 20$, $\delta = 4$.

p	$q\frac{\partial\phi(q)}{\partial q}$	$p\frac{\partial\delta(p)}{\partial p}$	F
0.03128(54)	0.0834(38)	-0.0299(14)	35.36(13)

Table 19: The calculated quantities which appear in the Lellouch-Lüscher factor F for $I = 2$. The corresponding factor for the case of non-interacting particles is $F_{\mathrm{free}} = 39.17$. The difference reflects the final two-pion scattering in a box. These results are from the $24^3 \times 64$ lattice ensemble.

i	$M_i^{1/2,\mathrm{lat}}(\times 10^{-2})$	$M_i'^{1/2,\mathrm{lat}}(\times 10^{-2})$	Re(A_0)(GeV)	Im(A_0)(GeV)
1	-0.02(87)	-0.82(14)	1.3(48)e-08	0
2	1.43(33)	1.085(60)	3.35(75)e-07	0
3	2.1(24)	-0.3(4)	-8.2(106)e-10	-4.6(59)e-12
4	3.5(19)	1.60((29)	6.7(35)e-09	2.2(12)e-11
5	-0.9(22)	-2.87(34)	0(4)e-10	0(2)e-12
6	-5.2(30)	-7.69(36)	-5.3(30)e-09	-3.2(17)e-11
7	9.48(75)	9.12(24)	6.69(85)e-11	1.12(14)e-13
8	28.9(14)	28.64(74)	-4.02(19)e-10	-1.96(9)e-12
9	-1.11(69)	-1.09(10)	2.1(12)e-14	-1.40(77)e-12
10	0.37(71)	0.80(10)	7.0(88)e-12	-1.7(21)e-13
Total	-	-	3.49(64)e-07	-1.8(19)e-11
Results without disconnected graph:			3.10(12)e-07	-3.75(23)e-11

Table 20: Fitted results for the weak, $\Delta I = 1/2$ kaon decay matrix elements from the $24^3 \times 64$ lattice ensemble. The column M_i^{lat} shows the complete result from each operator. The column $M_i'^{\mathrm{lat}}$ shows the result when the disconnected graphs are omitted while the 4th and 5th columns show the contributions of each operator the real and imaginary parts of the physical decay amplitude A_0. These results are obtained using a source-sink separation $\Delta = 16$, $\pi - \pi$ separation of $\delta = 4$, and a fit range $5 \leq t \leq 11$.

i	$M_i^{1/2,\mathrm{lat}}(\times 10^{-2})$	$M_i'^{1/2,\mathrm{lat}}(\times 10^{-2})$	Re(A_0)(GeV)	Im(A_0)(GeV)
1	-1.00(57)	-0.83(11)	6.6(31)e-08	0
2	1.09(24)	0.952(43)	2.59(53)e-07	0
3	-0.9(14)	-0.55(27)	5.4(66)e-10	3.0(37)e-12
4	1.2(12)	1.24((21)	2.3(21)e-09	7.7(69)e-12
5	-3.1(14)	-2.95(24)	4.0(26)e-10	2.1(14)e-12
6	-6.8(24)	-7.29(24)	-7.0(24)e-09	-4.2(15)e-11
7	9.00(48)	8.70(16)	6.29(54)e-11	1.056(90)e-13
8	27.67(92)	27.32(45)	-3.85(13)e-10	-1.877(62)e-12
9	-1.05(36)	-0.985(77)	1.98(62)e-14	-1.30(40)e-12
10	1.08(42)	0.806(74)	1.60(54)e-12	-3.8(13)e-13
Total	-	-	3.21(45)e-07	-3.3(15)e-11
Results without disconnected graph:			2.781(78)e-07	-3.63(16)e-11

Table 21: Fitted results for the weak, $\Delta I = 1/2$ kaon decay matrix elements from the $24^3 \times 64$ lattice ensemble, with the same setup as Tab.20 except that $\Delta = 12$,and a fit range $4 \leq t \leq 8$.

Figures

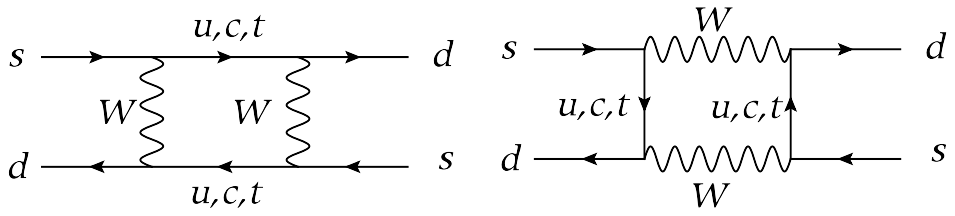

Figure 1: $K^0 - \overline{K}^0$ mixing in the standard model through the box diagrams.

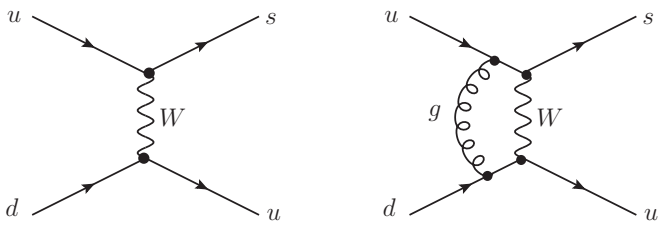

(a) current-current

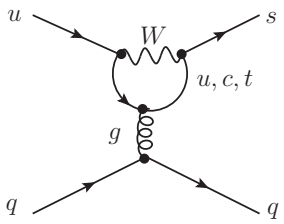

(b) QCD penguin

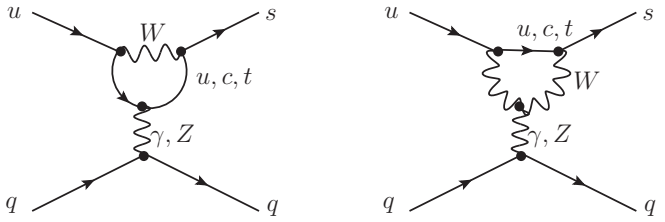

(c) Electro-Weak penguin

Figure 2: Diagrams in the full theory which the current-current operators, QCD penguin operators, and Electro-Weak penguin operator originate.

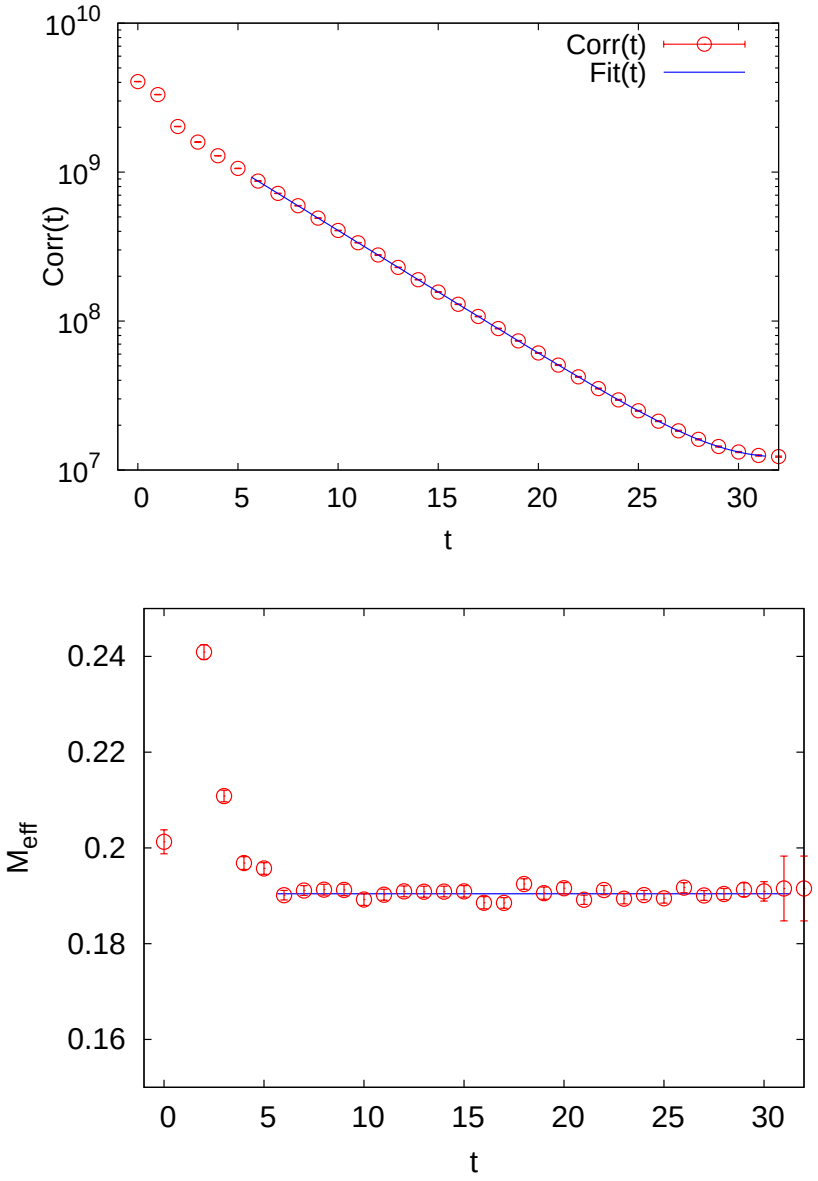

Figure 3: Top: Correlation function for the pion. Bottom: The corresponding effective mass plot. It is calculated from the $24^3 \times 64$ lattice with $m_l = 0.005$, Coulomb gauge fixed wall source and sink, on 138 configurations. The fitted value is $m_\pi = 0.19043(36)$.

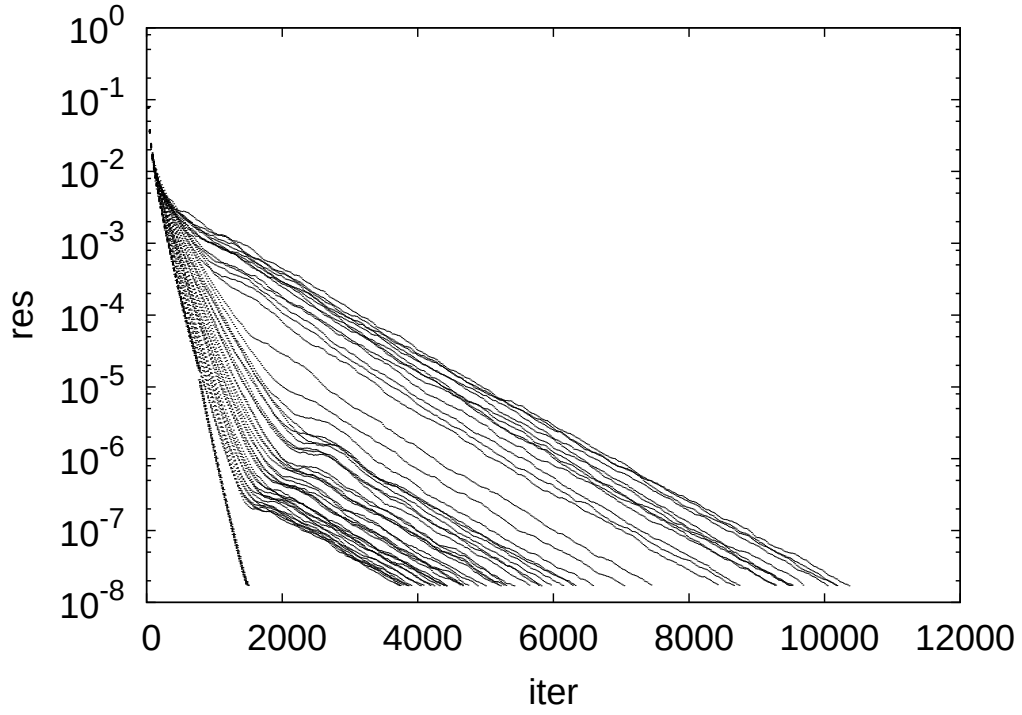

Figure 4: Relative residual versus number of iterations using EigCG on a $32^3 \times 64 \times 32$ DSDR lattice. From the first 5 propagator solves (60 Dirac solves), the incremental EigCG algorithm accumulate more and more low modes and the CG converges faster and faster. After that, we stop accumulating more low modes. All new solves converge to 10^{-8} in roughtly 1500 iterations by using one restart at 10^{-5} to achieve further speed up.

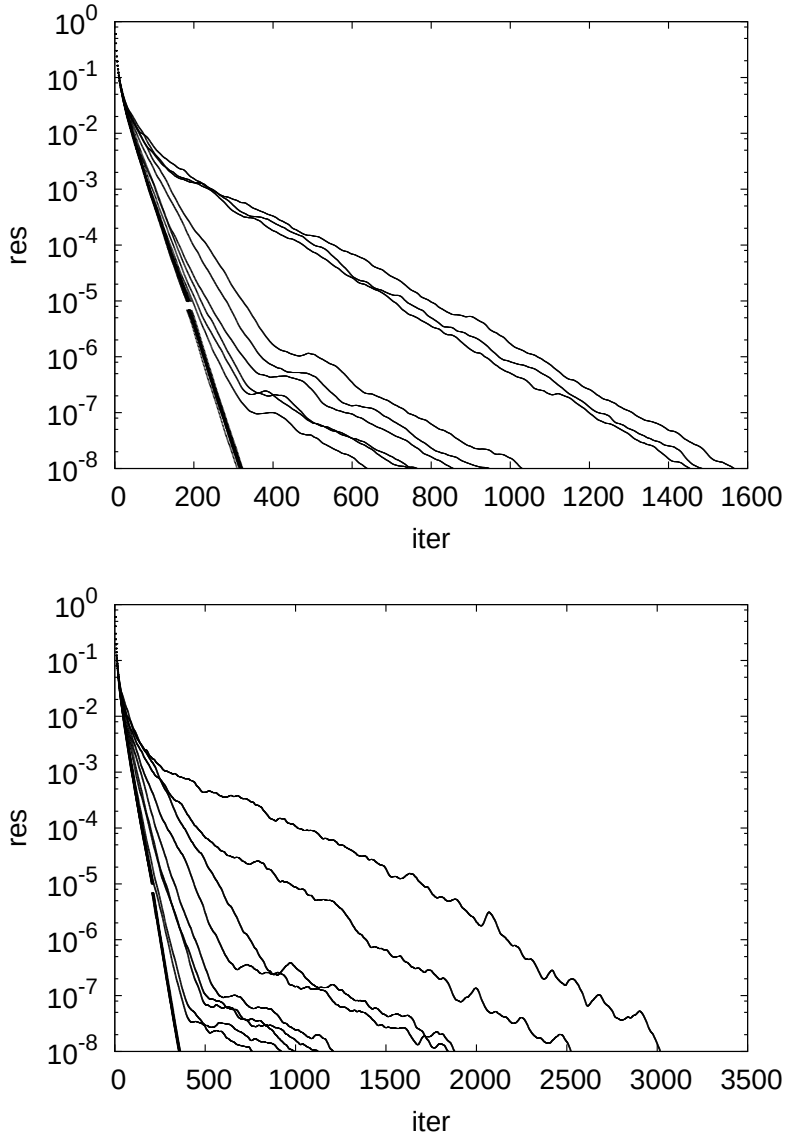

Figure 5: Relative residual versus number of iterations using EigCG on a $16^3 \times 32 \times 16$ lattice. The top graph has the quark mass $m_l = 0.01$ ($m_\pi = 421$ MeV). The bottom graph has the quark mass $m_l = 0.001$ ($m_\pi = 204$ MeV). This comparison shows that the EigCG algorithm is not sensitive to the underlying quark mass.

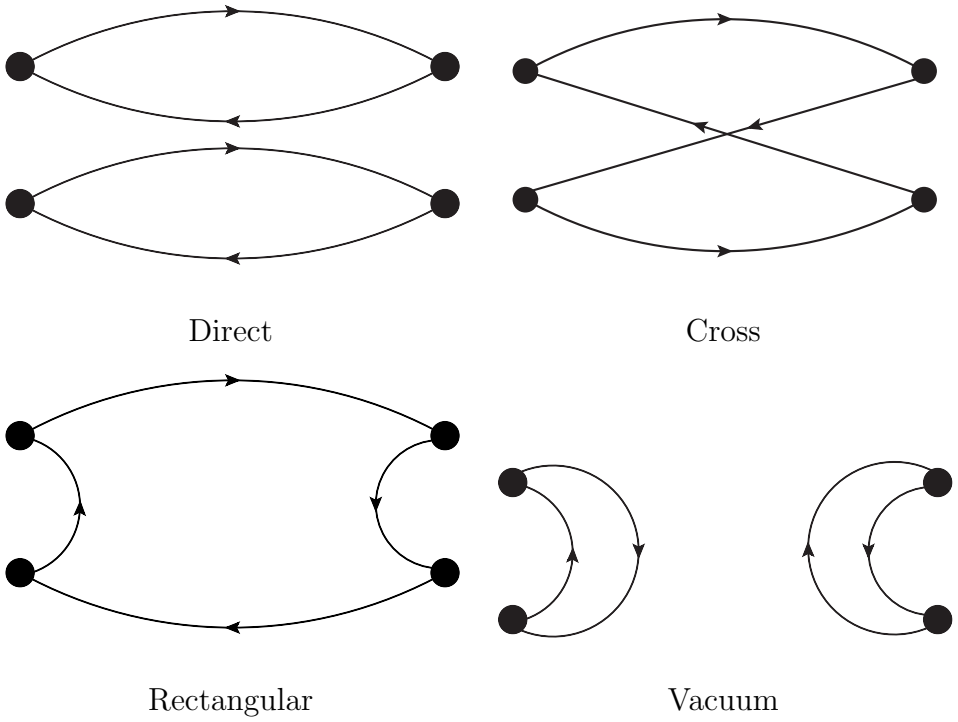

Figure 6: The Direct(D), Cross(C), Rectangular(R), and Vacuum(V) diagrams that contributes to $\pi - \pi$ scattering.

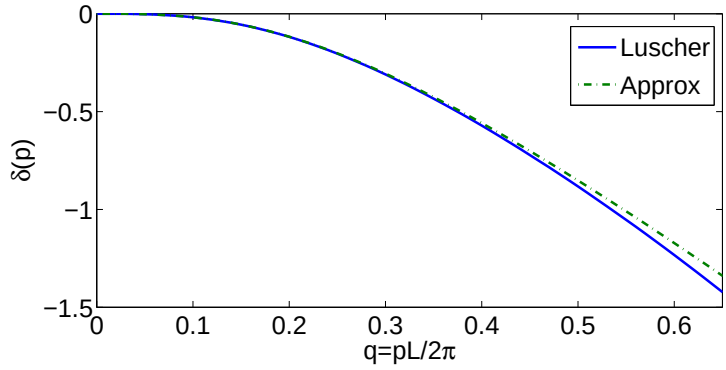

Figure 7: The comparison of the approximate solution (Eq. 4.20) to Lüscher's formula (Eq. 4.9) for the scattering phase shift at the quantized momentum $q = qL/2\pi$ for two particles in a box.

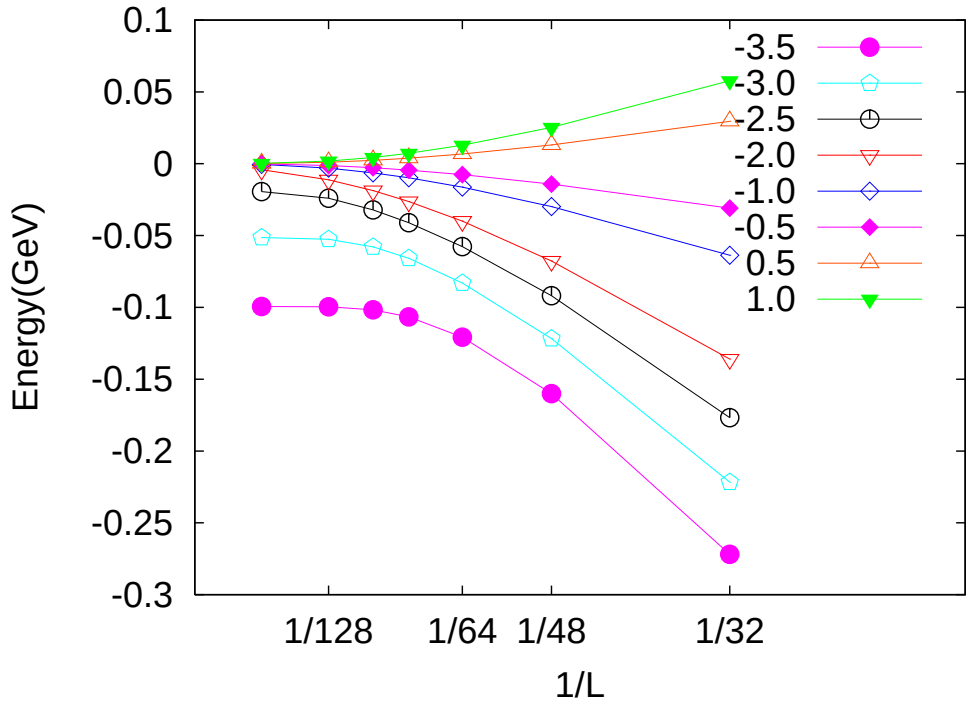

Figure 8: The energy shift of two particles in a box with size L and periodic boundary conditions. The lattice spacing a=0.1fm, $m_\pi = 0.14$ GeV, $m_N = m_\pi$.

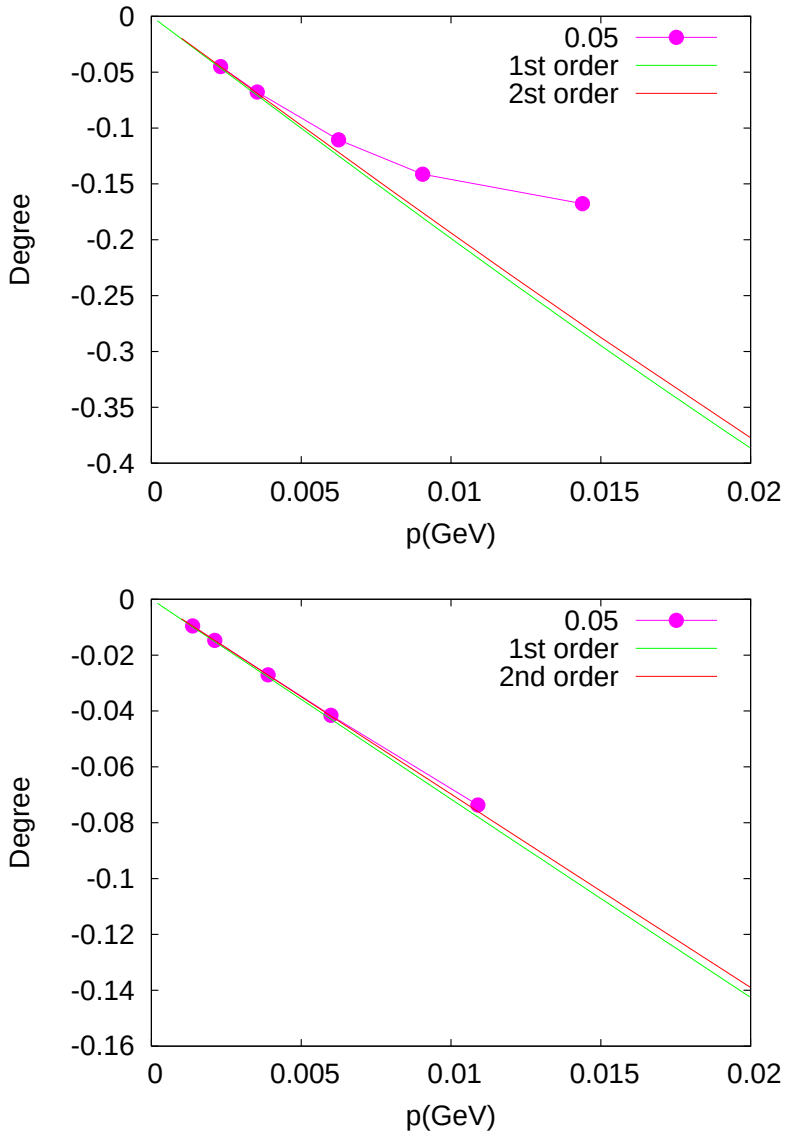

Figure 9: Checking Lüscher's formula for the scattering length. The Yukawa interaction coupling strength is set to 0.05. The box size L is chosen to be 32,48,64,96,128. The pion mass is 142.7 MeV for the top graph and 400 MeV for the bottom graph. Lattice spacing is set to 0.1437fm (1.373GeV^{-1}).

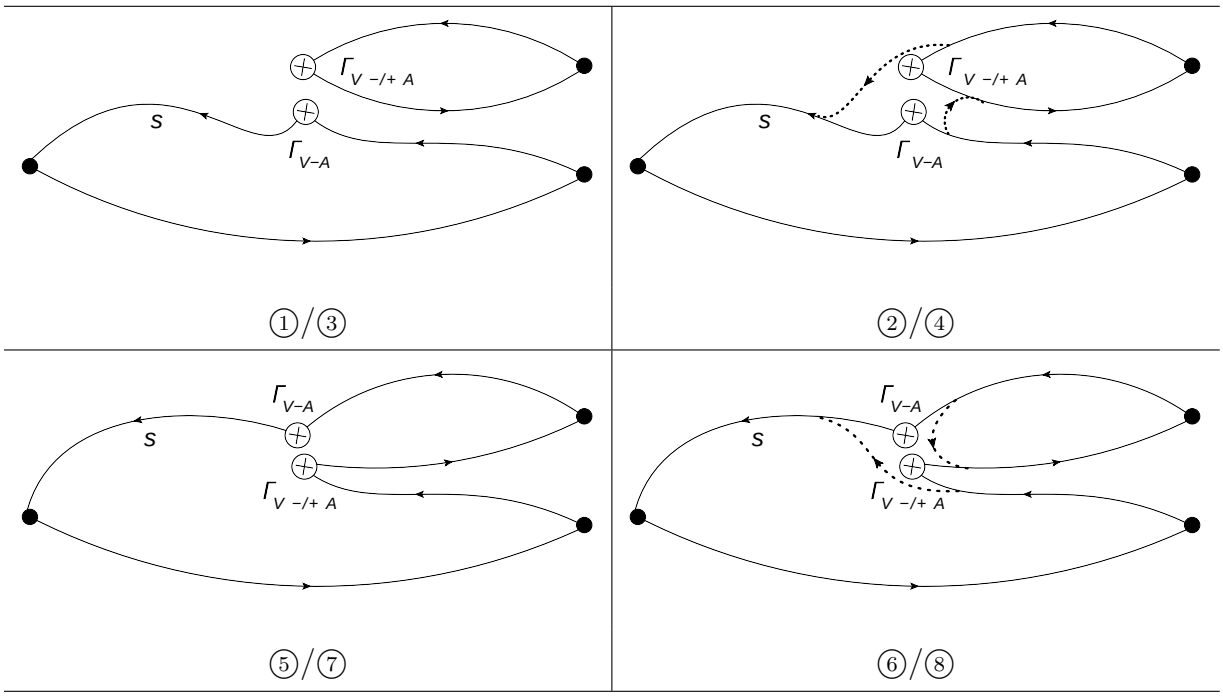

Figure 10: Diagrams representing the eight $K^0 \to \pi\pi$ contractions of *type*1, where $\Gamma_{V\pm A} = \gamma_\mu(1 \pm \gamma_5)$. The black dot indicates a γ_5 matrix, which is present in each operator creating or destroying a pseudoscalar meson.

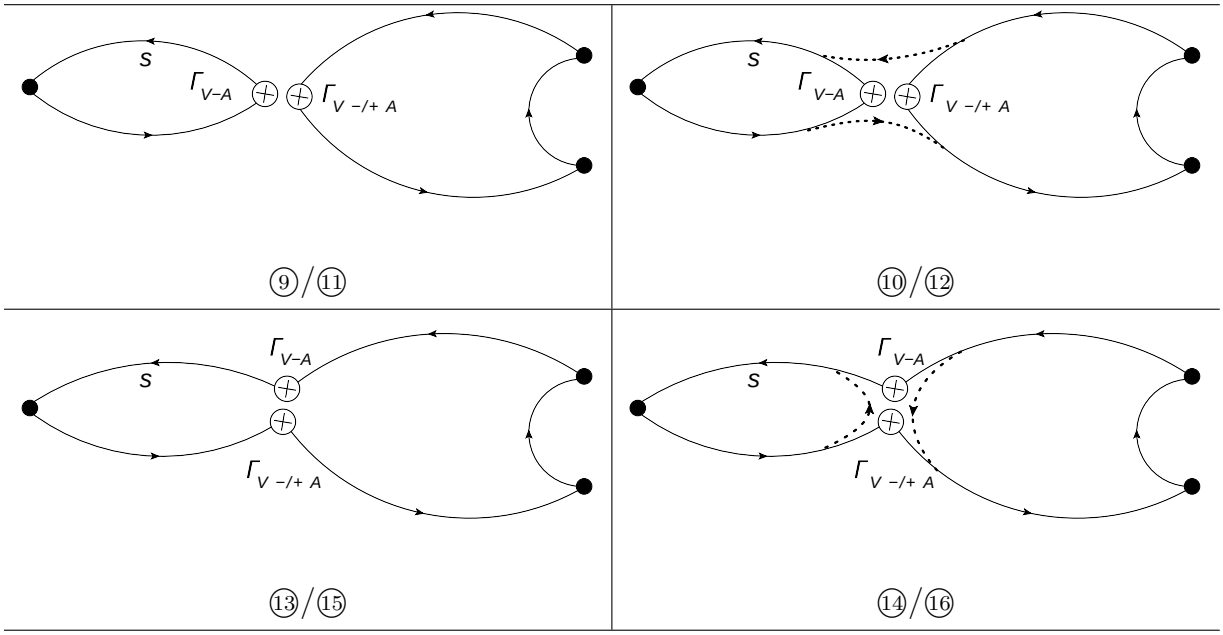

Figure 11: Diagrams for the eight *type*2 $K^0 \to \pi\pi$ contractions.

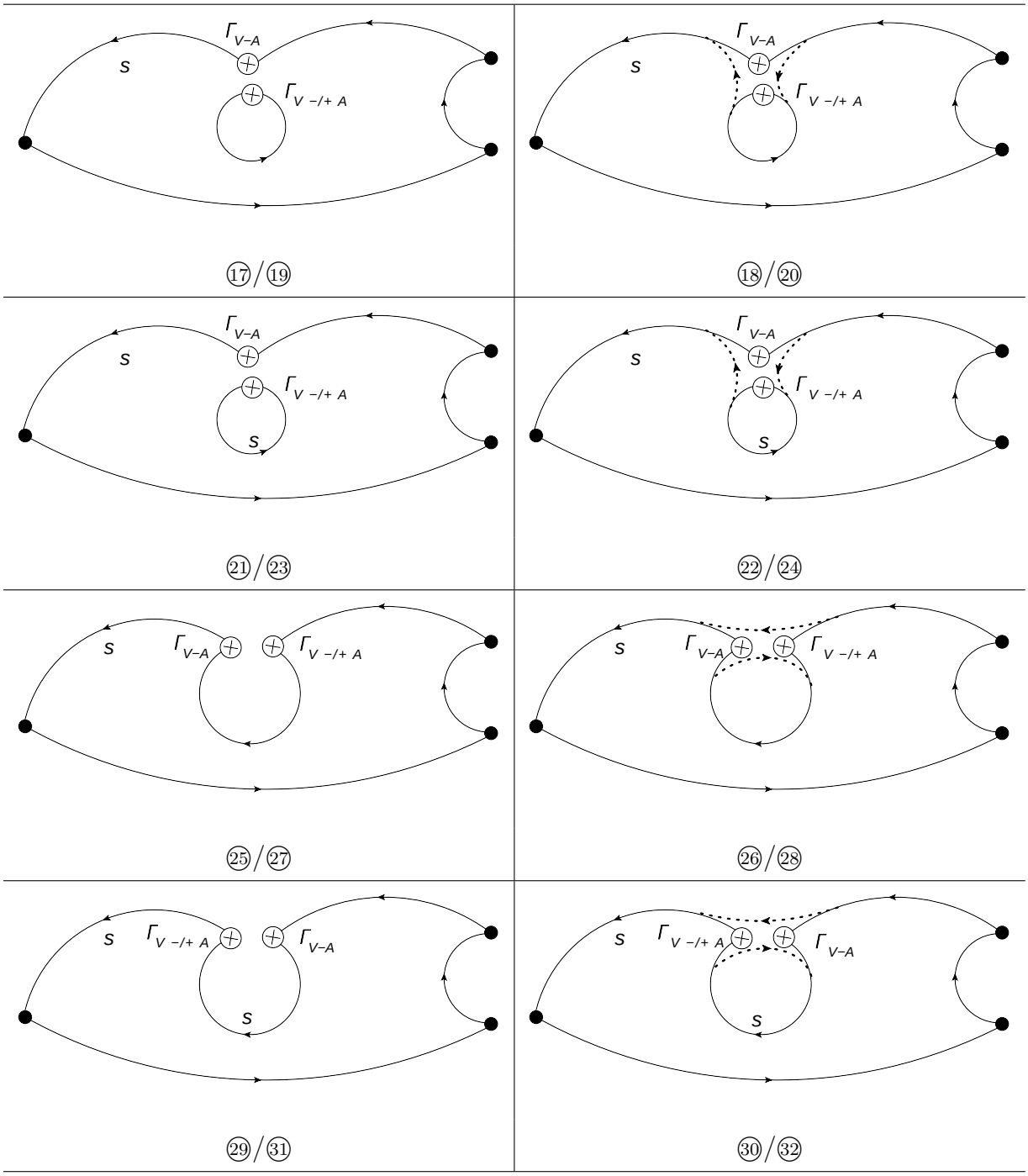

Figure 12: Diagrams for the 16 *type*3 $K^0 \to \pi\pi$ contractions.

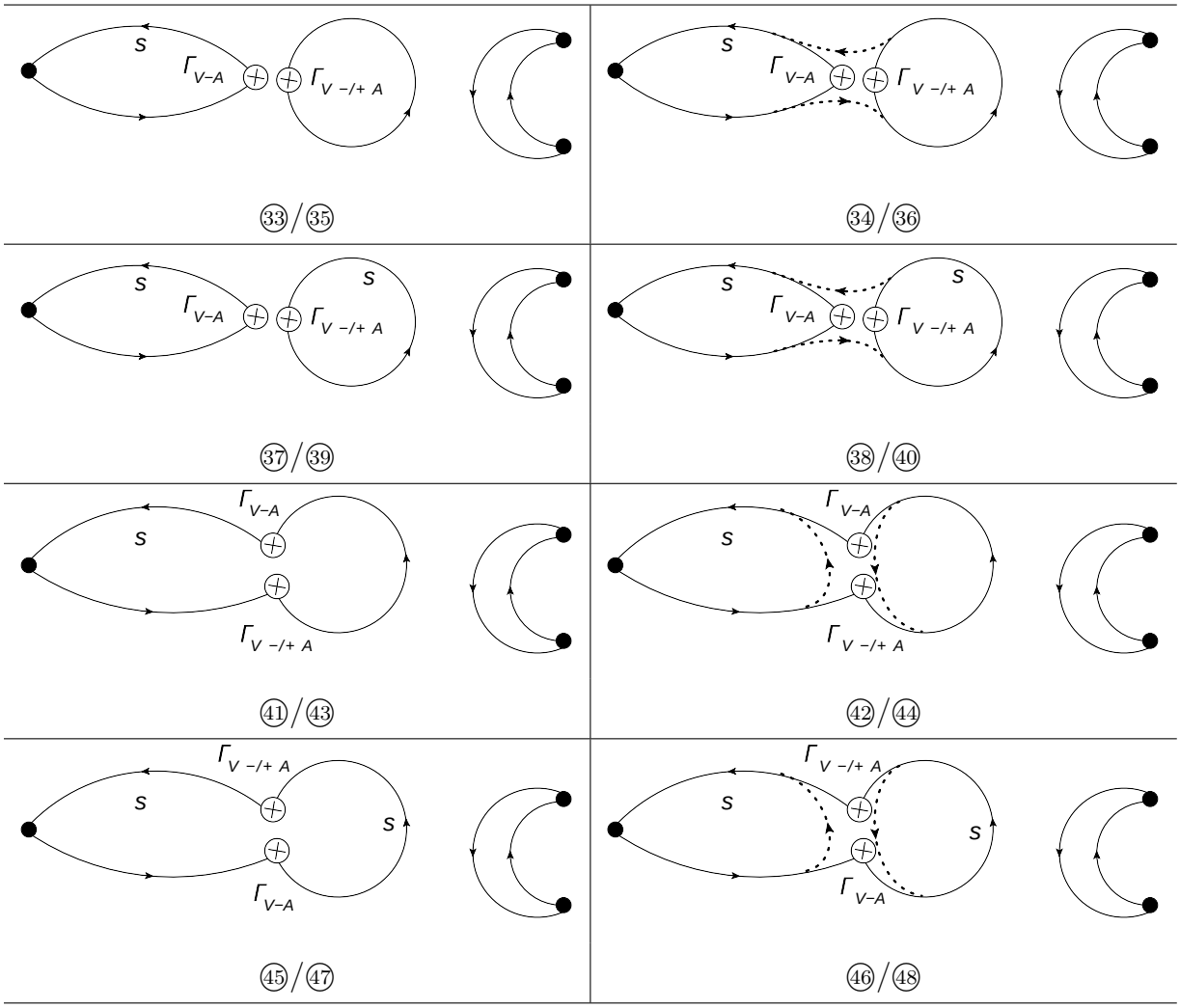

Figure 13: Diagrams for the sixteen *type*4 $K^0 \to \pi\pi$ contractions.

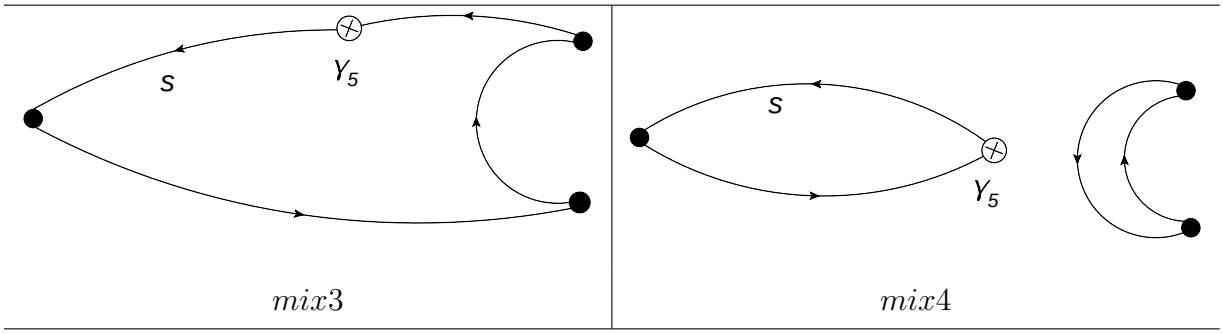

Figure 14: Diagrams showing the contractions needed to evaluate the subtraction terms. These are labeled $mix3$ and $mix4$ and constructed from the $type3$ and $type4$ contractions by replacing the operator Q_i and fermion loop with the vertex $\overline{s}\gamma_5 d$.

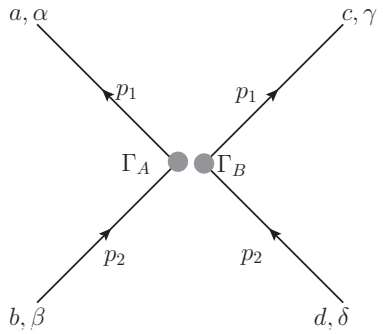

(a) $F_{\Gamma_A\Gamma_B}$

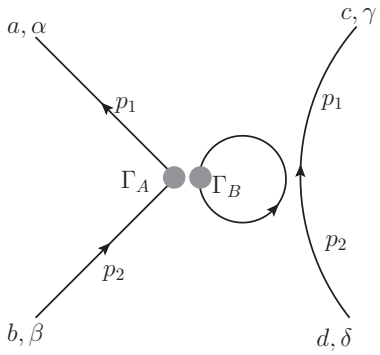

(b).$F_{\Gamma_A\Gamma_B D_1}$

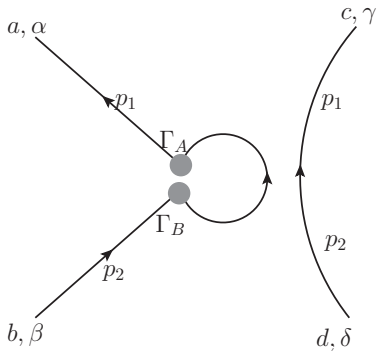

(c) $F_{\Gamma_A\Gamma_B D_2}$

Figure 15: The three spin structures in NPR calculation of $K \to \pi\pi$ operators.

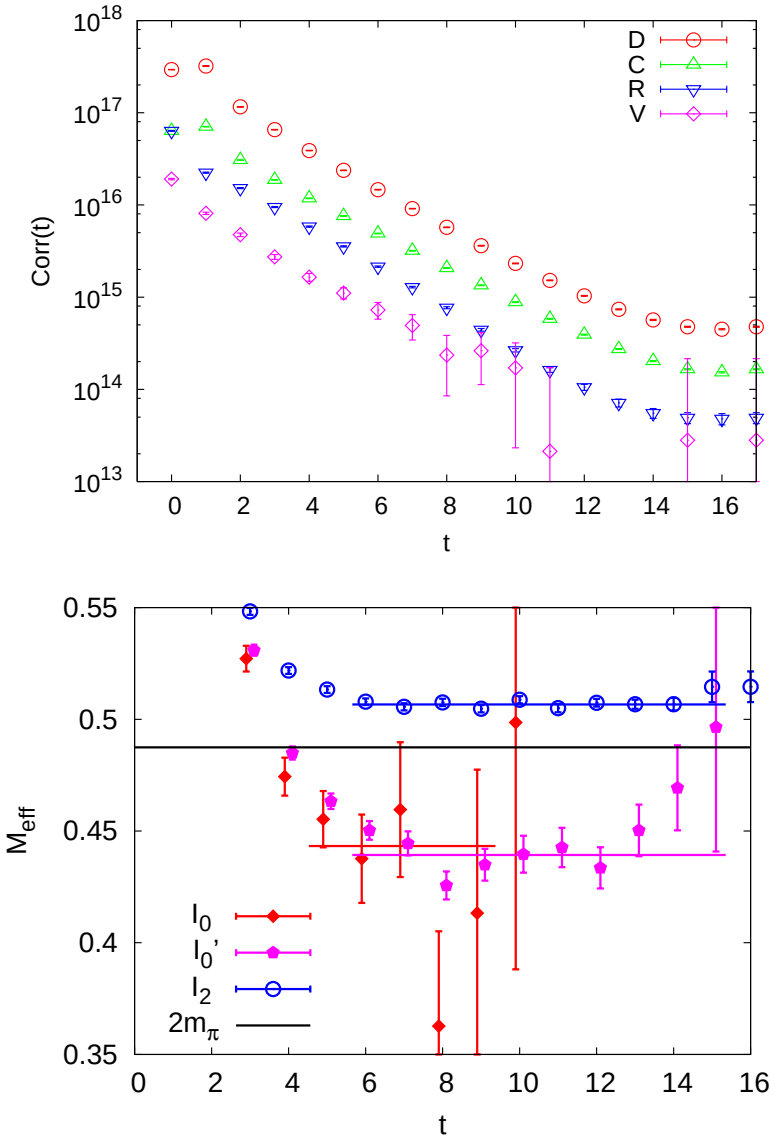

Figure 16: Top: Results for the four types of contractions, direct (D), cross (C), rectangle (R), and vacuum(V) represented by the graphs in Fig. 6. Bottom: Effective mass plots for correlation functions for states with isospin two (I_2), isospin zero (I_0), isospin zero without the disconnected graph (I_0') and twice the pion effective mass ($2m_\pi$).

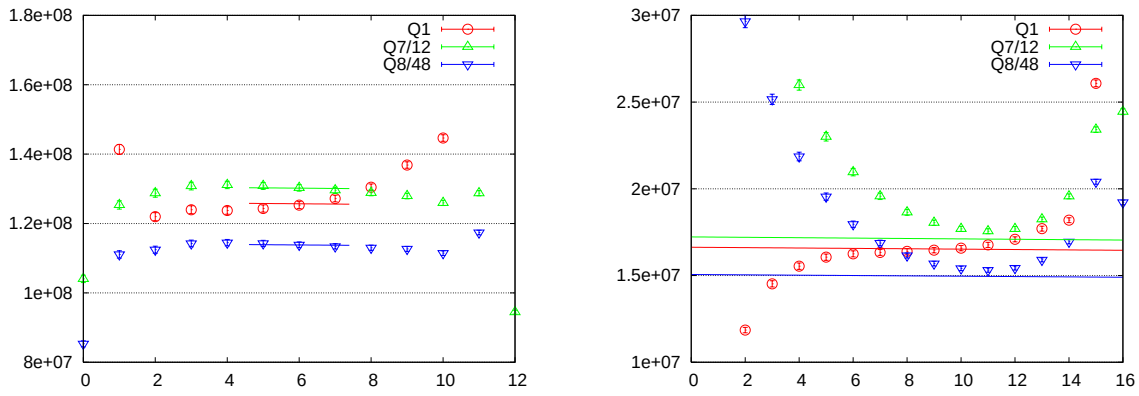

$\Delta = 12$ $\Delta = 16$

Figure 17: Plots of the $\Delta I = 3/2$ $K^0 \to \pi - \pi$ correlation functions for kaon source and $\pi - \pi$ sink separations of $\Delta = 12$ (left panel) and 16 (right panel). The x-axis gives the time t specifying the time slice over which the operator, $Q_i(\vec{x}, t)$, $i = 1$, 7, 8, is averaged. The results for the operator Q_7 are divided by 12, and those for Q_8 by 48 to allow the results to be shown in the same graph. The correlators $C_{2,i}(\Delta, t)$ are fit using the $\Delta = 12$ data with a fitting range $5 \leq t \leq 7$. The resulting constants are shown as horizontal lines in both the $\Delta = 12$ and 16 graphs. We can see that the $\Delta = 16$ data are consistent with those from $\Delta = 12$, but receive large contributions from the around-the-world paths.

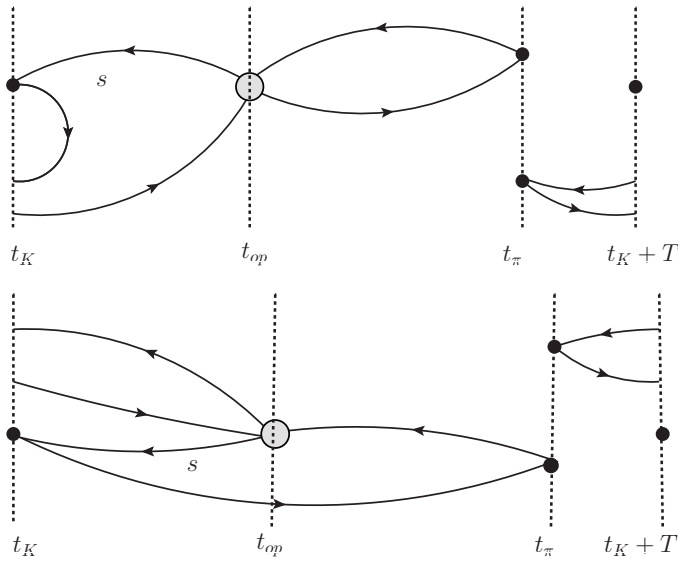

Figure 18: Diagrams showing the dominant around-the-world paths contributing to graphs of *type*1. The space-time region between the kaon wall source at t_K and its periodic recurrence at $t_K + T$ is shown, where T is the extent of the periodic lattice in the time direction. For this around-the-world path, one pion travels directly from the pion wall source at t_π to the weak operator, represented by the grey dot at $t_{\rm op}$. However, the second pion propagates in the other direction in time, passes through the periodic boundary and combines with the kaon before reaching the weak operator at $t_{\rm op}$.

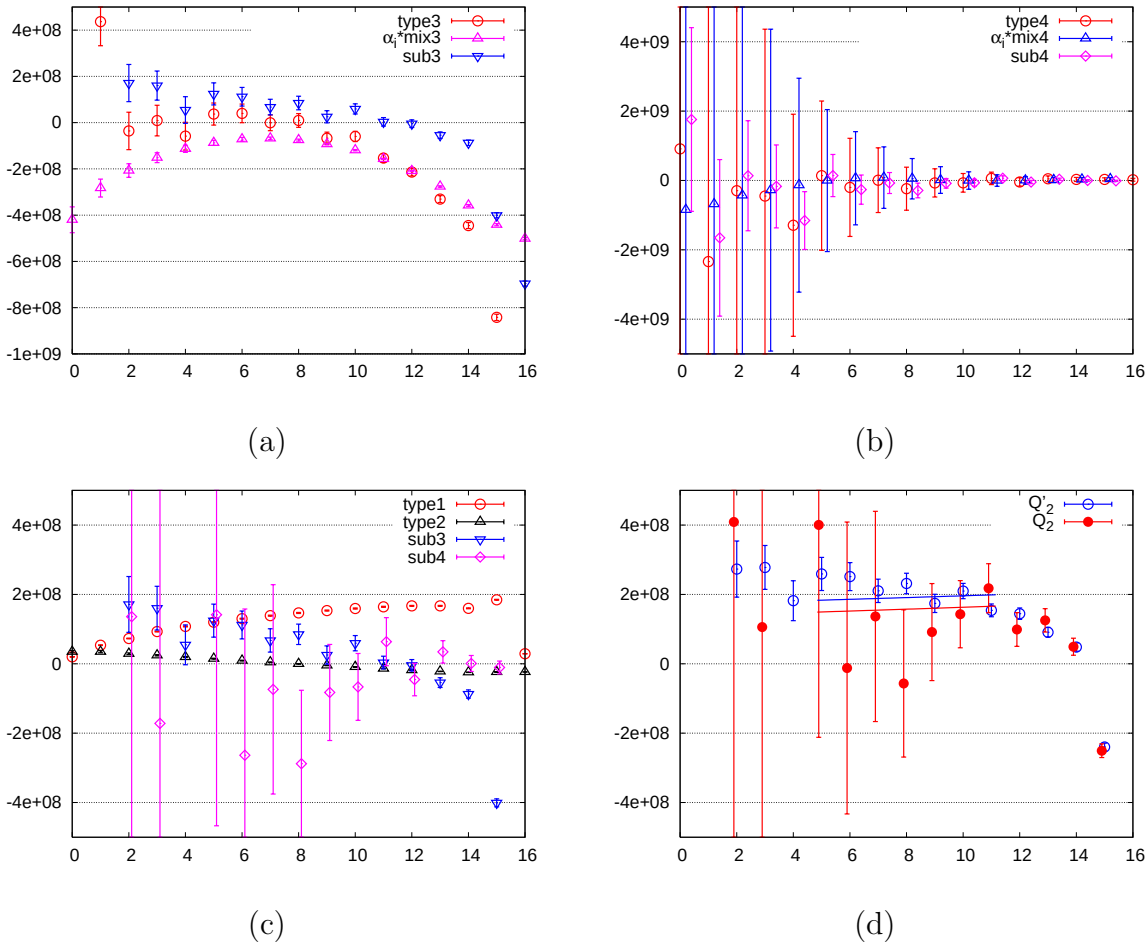

Figure 19: Plots showing the t dependence of the various contractions which contribute to the $\Delta I = 1/2$ correlation function $C_{0,2}(\Delta = 16, t)$ for the operator Q_2. (a) Contractions of *type*3, the divergent mixing term *mix*3 that will be subtracted and the result after subtraction, *sub*3. (b) Contractions of *type*4, the divergent mixing term *mix*4 that will be subtracted and the result after subtraction, *sub*4. (c) Results for each of the four types of contraction after the needed subtractions have been performed. (d) See caption Fig. 20.

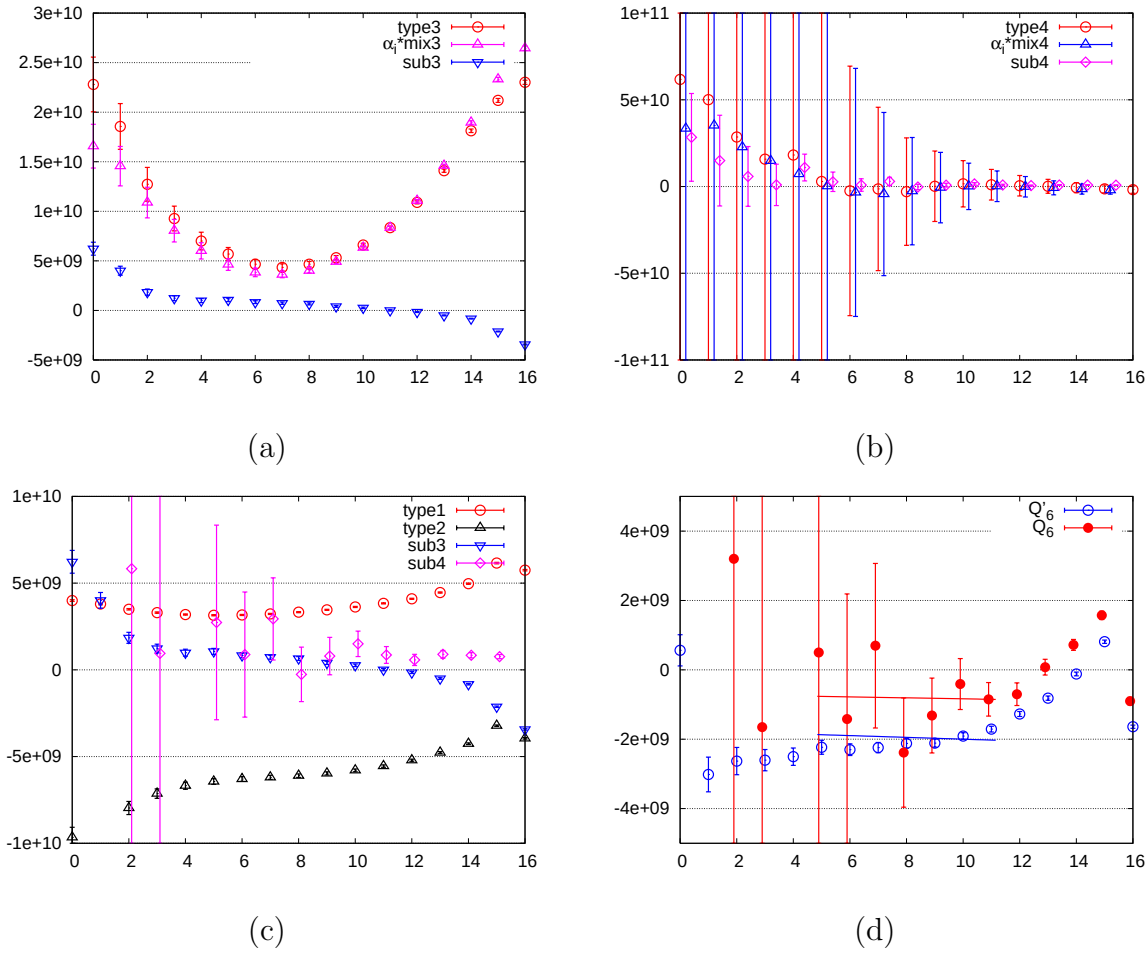

(a) (b) (c) (d)

Figure 20: The result for each type of contraction contributing to the 3-point correlation function $C_{0,6}(\Delta = 16, t)$ for the operator Q_6 following the same conventions as in Fig. 19. The description of (a), (b), and (c) is the same as Fig. 19. (d): Results for the complete Q_6 correlation function $C_{0,6}(\Delta = 16, t)$ obtained by combining these four types of contractions. The solid points labeled Q_6 are the physical result while the open points labeled Q_6' are obtained by omitting all the vacuum graphs, *sub*4. The solid and dotted horizontal lines indicate the corresponding fitting results and the time interval, $5 \leq t \leq 11$ over which the fits are performed.

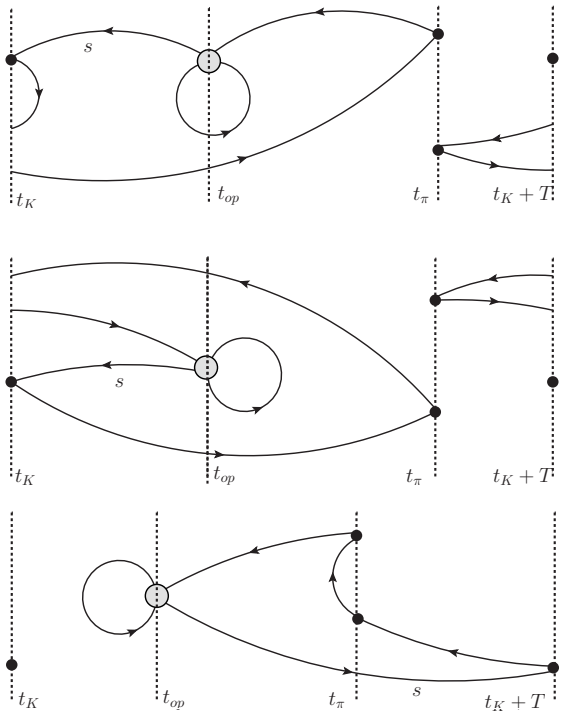

Figure 21: The dominant around-the-world paths contributing to graphs of *type*3. As in Fig. 18 we show the space-time region between the kaon source at $t = t_K$ and its periodic recurrence at $t = t_K + T$. The gray circle represents the four quark operator Q_i. For the first two graphs, one of the two pions created at the $t = t_\pi$ source travels directly to the operator Q_i while the second pion travels in the other direction in time and reaches the kaon and weak operator by passing through the periodic lattice boundary. In the third diagram it is the kaon which travels in the opposite to the expected time direction.

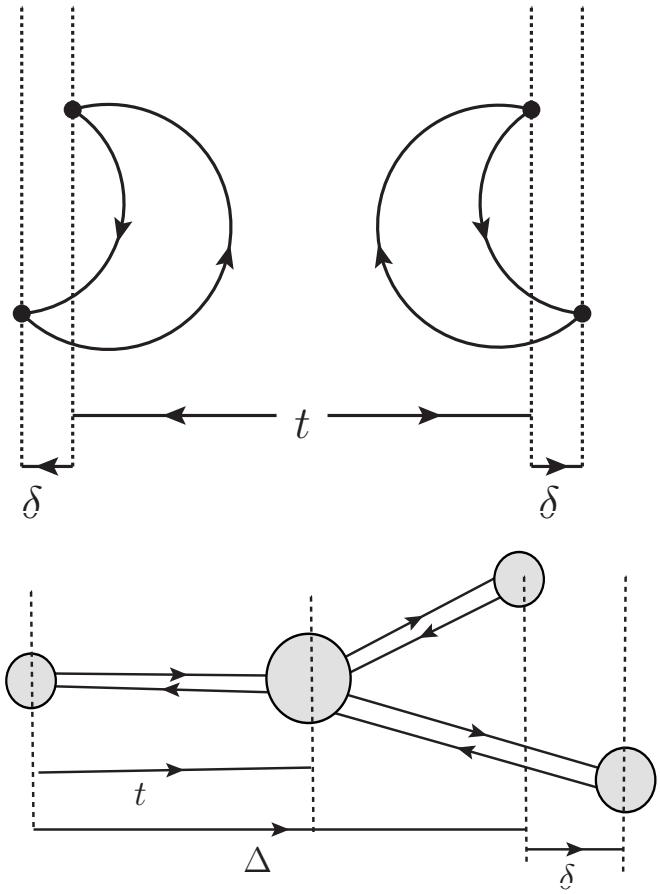

Figure 22: Separating the two pion sources in the time direction. The top panel shows the setup for the $\pi - \pi$ scattering calculation, and the bottom panel shows the setup for the $k \to \pi\pi$ decay calculation.

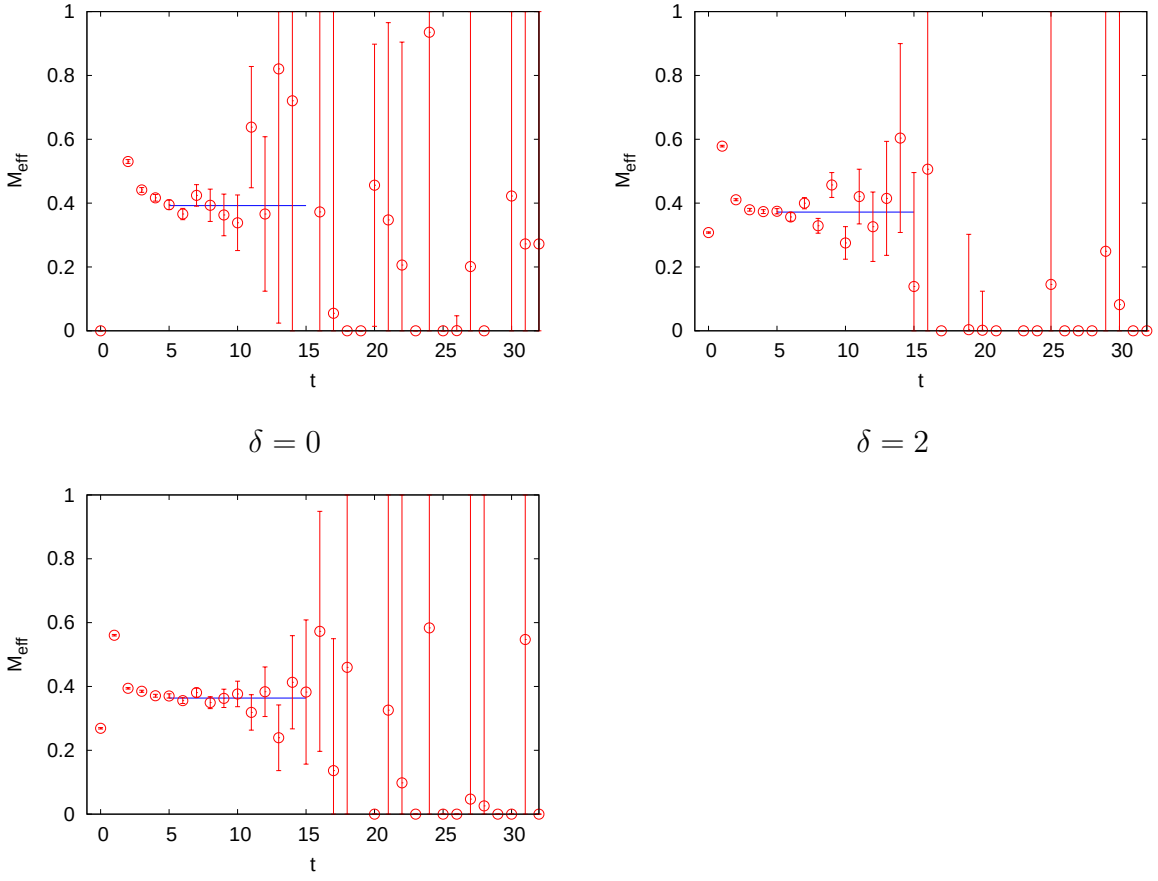

$\delta = 0$ $\delta = 2$

$\delta = 4$

Figure 23: Effective mass plot for the two pions in the isospin zero channel using $\pi - \pi$ separation of 0, 2 and 4. The energies calculated from these three setups are 0.3922(126), 0.3720(62) and 0.3639(55) respectively. The result from the $\delta = 0$ calculation has a very poor plateau. Note, the time separation t which is plotted ueses the conservative smallest time separation between the field defining the source and sink operators, as shown in Fig. 22.

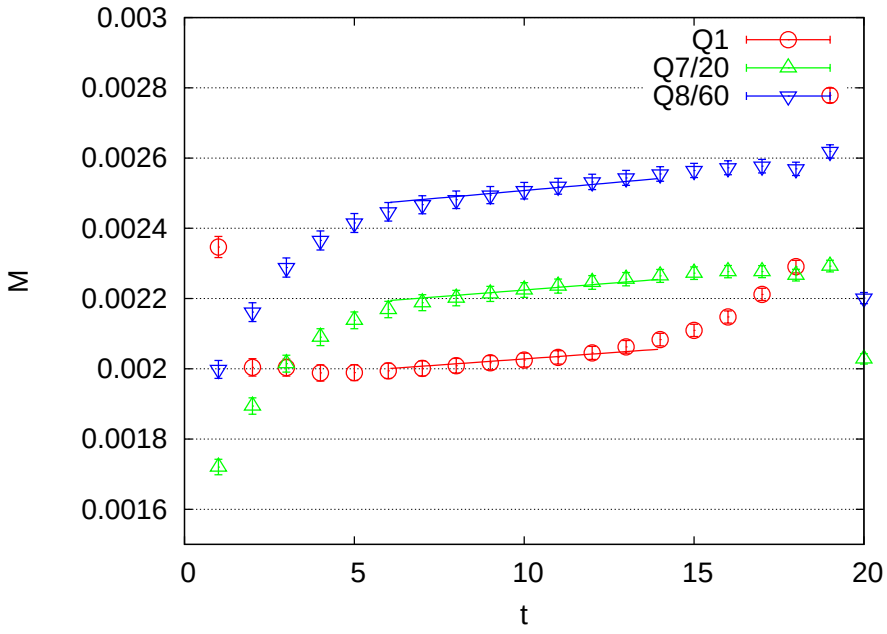

Figure 24: The weak matrix element for $\langle \pi\pi_{I=2}|Q_1|K^0\rangle$, $\langle \pi\pi_{I=2}|Q_7|K^0\rangle$ and $\langle \pi\pi_{I=2}|Q_8|K^0\rangle$. To make them fit in a single graph, the result for Q_7 is devided by 20, and that for Q_8 is devided by 60. The x-axis represents the position of the operator relative the kaon, and y-axis is the amplitude defined in Eq. 4.37. We used $\Delta = 20$, and $\delta = 4$ here.

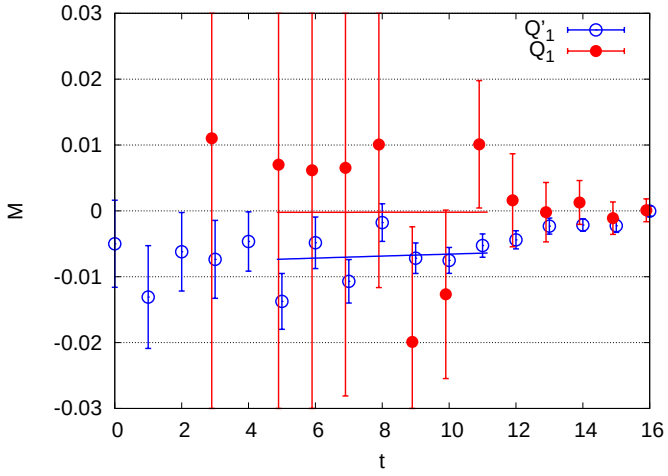

Figure 25: The weak matrix element for $\langle \pi\pi_{I=0}|Q_1|K^0\rangle$. The x-axis represents the position of the operator relative the the kaon, and y-axis is the amplitude defined in Eq. 4.37. The $'$ symbol represents the result without the disconnected graph. We used $\Delta = 16$, and $\delta = 4$ here.

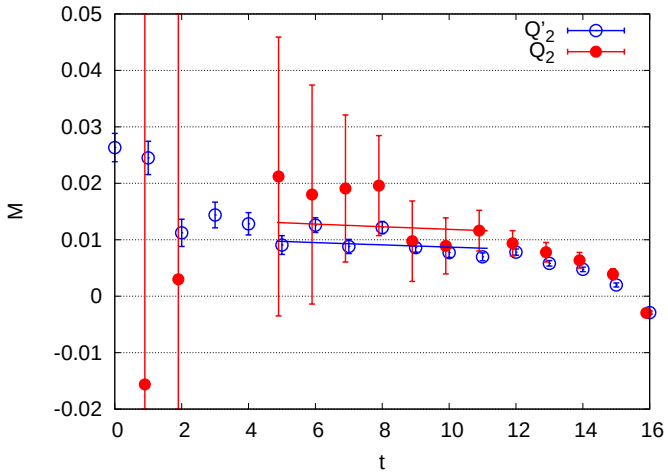

Figure 26: The weak matrix element for $\langle \pi\pi_{I=0}|Q_2|K^0\rangle$ with the same setup as Fig.25.

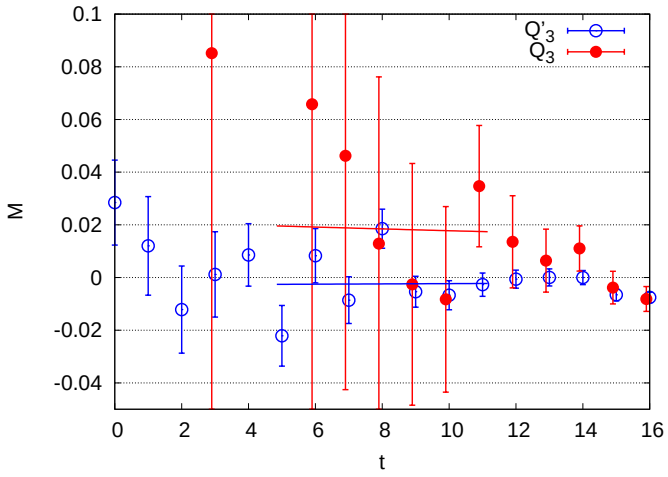

Figure 27: The weak matrix element for $\langle \pi\pi_{I=0}|Q_3|K^0\rangle$ with the same setup as Fig.25.

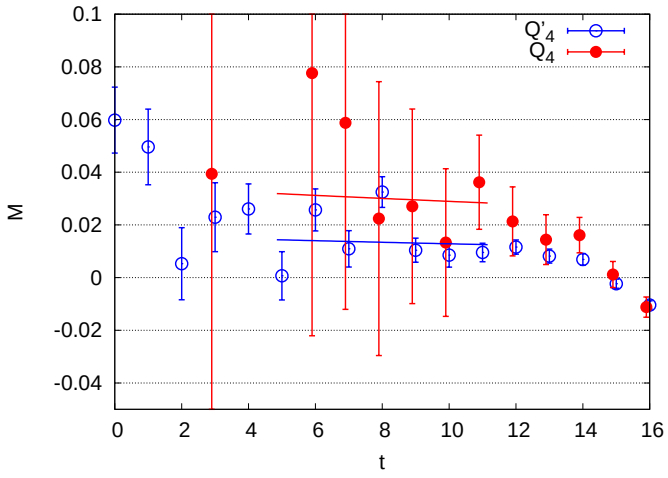

Figure 28: The weak matrix element for $\langle \pi\pi_{I=0}|Q_4|K^0\rangle$ with the same setup as Fig.25.

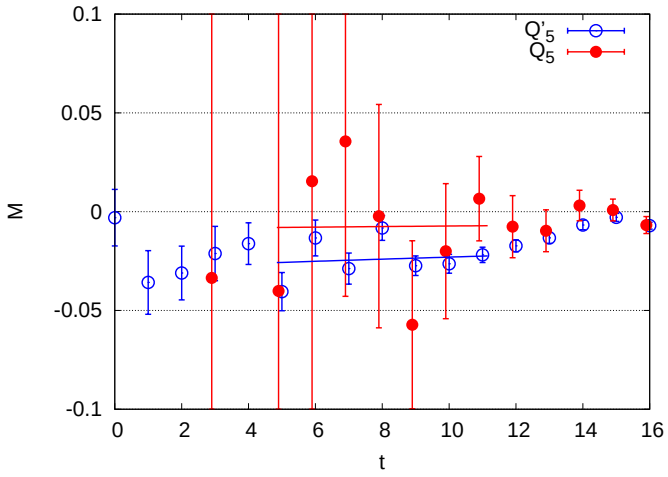

Figure 29: The weak matrix element for $\langle \pi\pi_{I=0}|Q_5|K^0\rangle$ with the same setup as Fig.25.

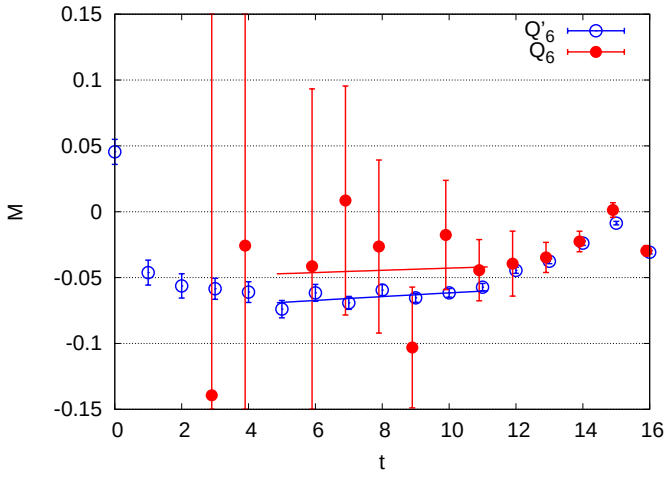

Figure 30: The weak matrix element for $\langle \pi\pi_{I=0}|Q_6|K^0\rangle$ with the same setup as Fig.25.

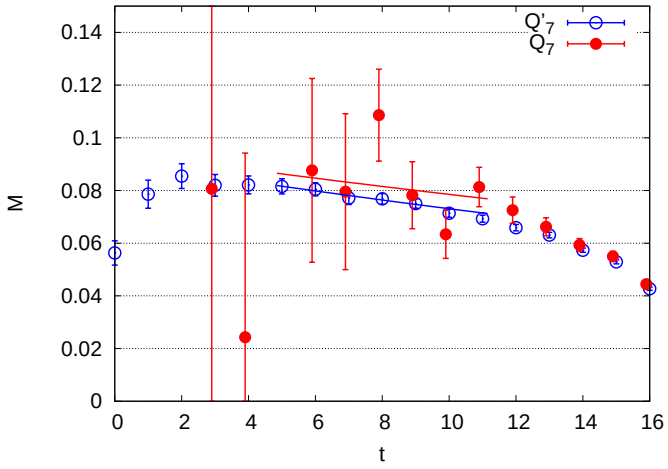

Figure 31: The weak matrix element for $\langle \pi\pi_{I=0}|Q_7|K^0\rangle$ with the same setup as Fig.25.

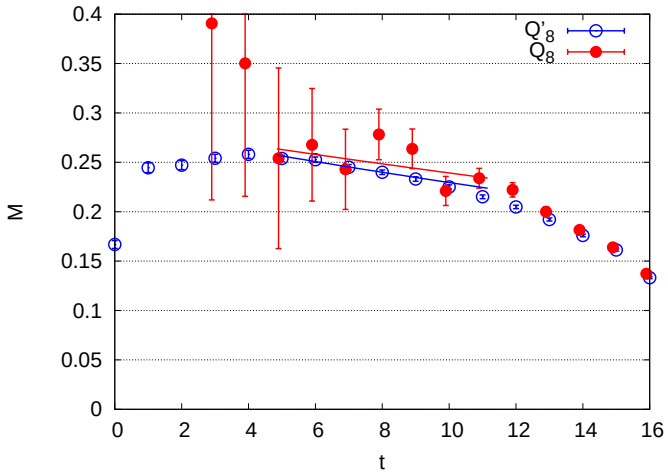

Figure 32: The weak matrix element for $\langle \pi\pi_{I=0}|Q_8|K^0\rangle$ with the same setup as Fig.25.

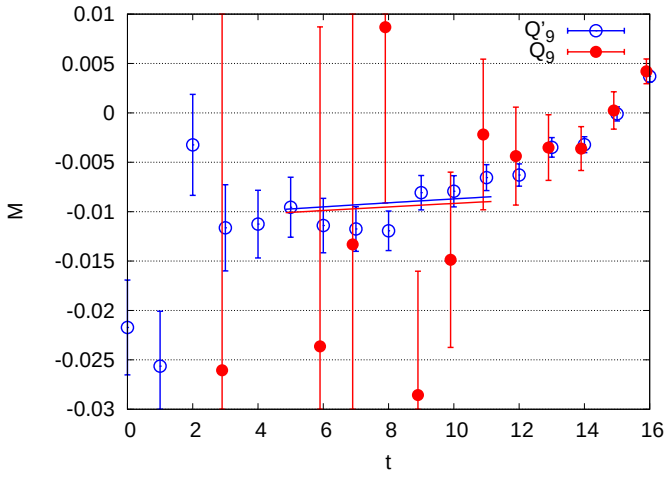

Figure 33: The weak matrix element for $\langle \pi\pi_{I=0}|Q_9|K^0\rangle$ with the same setup as Fig.25.

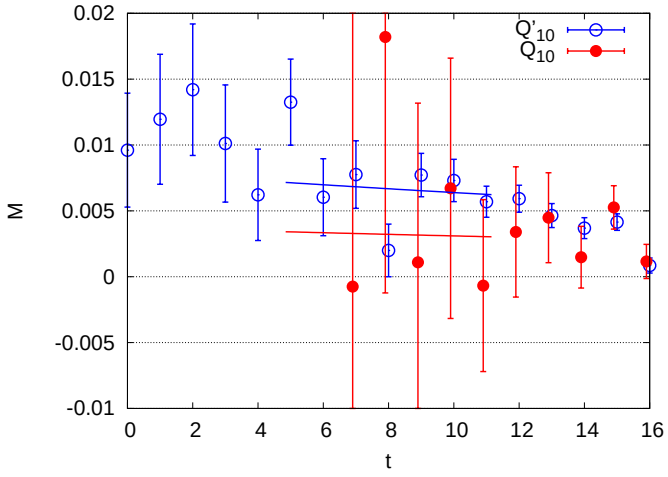

Figure 34: The weak matrix element for $\langle \pi\pi_{I=0}|Q_{10}|K^0\rangle$ with the same setup as Fig.25.

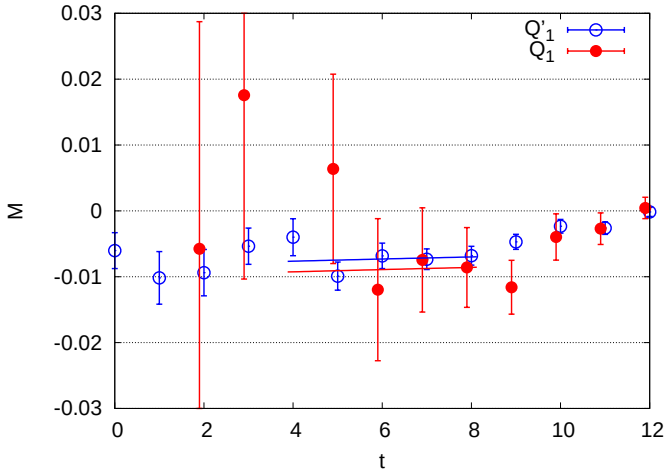

Figure 35: The weak matrix element for $\langle \pi\pi_{I=0}|Q_1|K^0\rangle$. The x-axis represents the position of the operator relative the the kaon, and y-axis is the amplitude defined in Eq. 4.37. The $'$ symbol represents the result without the disconnected graph. We used $\Delta = 12$, and $\delta = 4$ here.

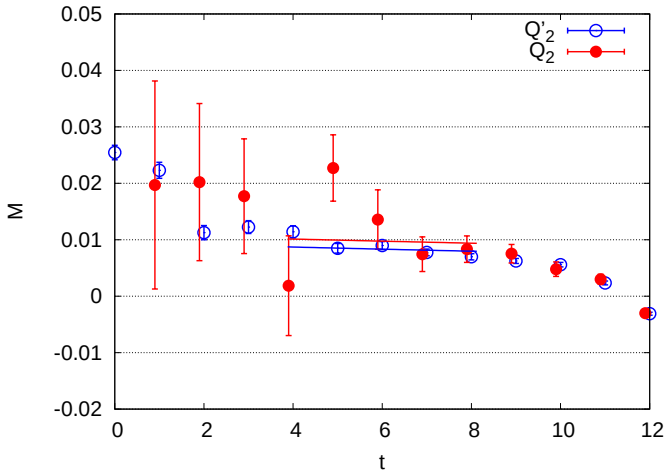

Figure 36: The weak matrix element for $\langle \pi\pi_{I=0}|Q_2|K^0\rangle$ with the same setup as Fig.35.

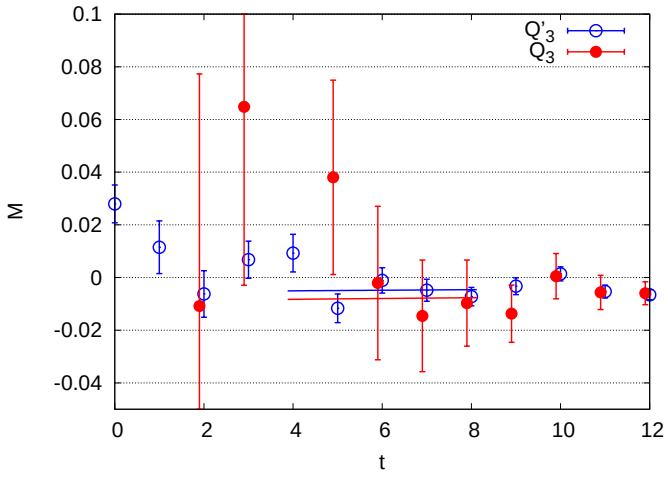

Figure 37: The weak matrix element for $\langle \pi\pi_{I=0}|Q_3|K^0\rangle$ with the same setup as Fig.35.

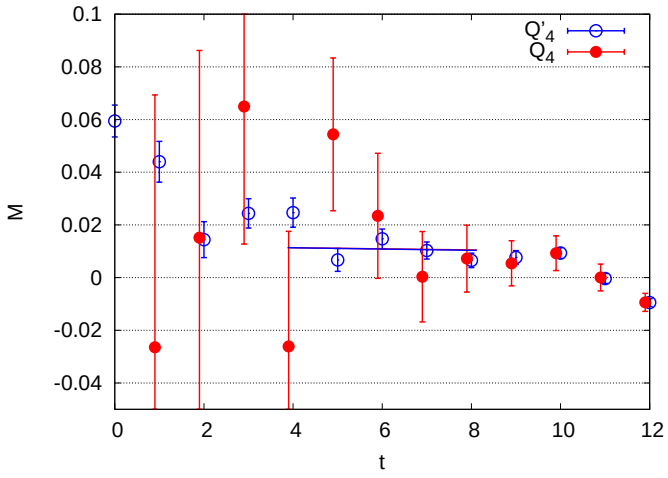

Figure 38: The weak matrix element for $\langle \pi\pi_{I=0}|Q_4|K^0\rangle$ with the same setup as Fig.35.

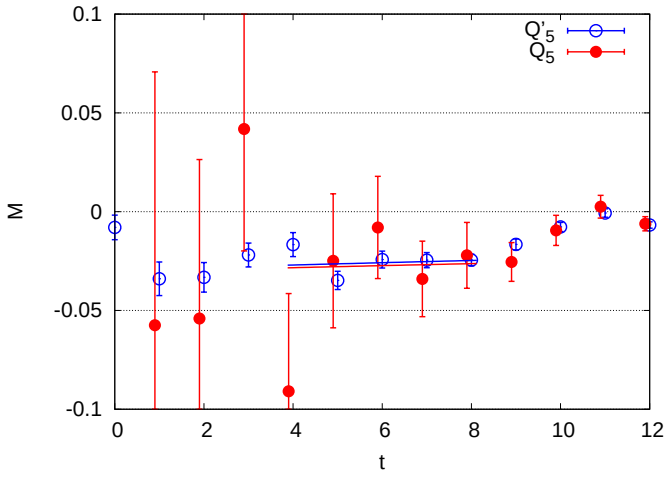

Figure 39: The weak matrix element for $\langle \pi\pi_{I=0}|Q_5|K^0\rangle$ with the same setup as Fig.35.

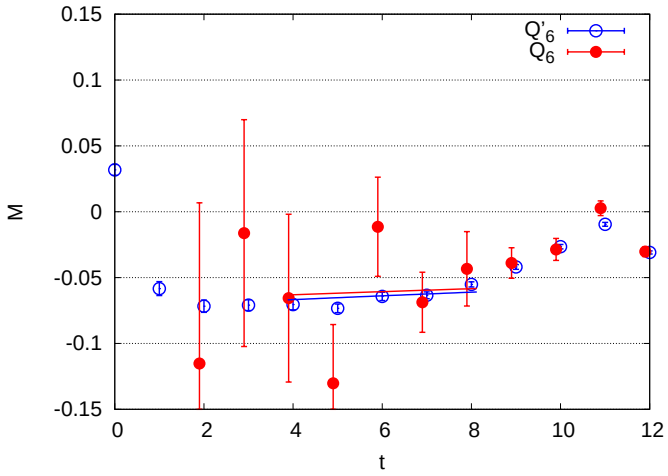

Figure 40: The weak matrix element for $\langle \pi\pi_{I=0}|Q_6|K^0\rangle$ with the same setup as Fig.35.

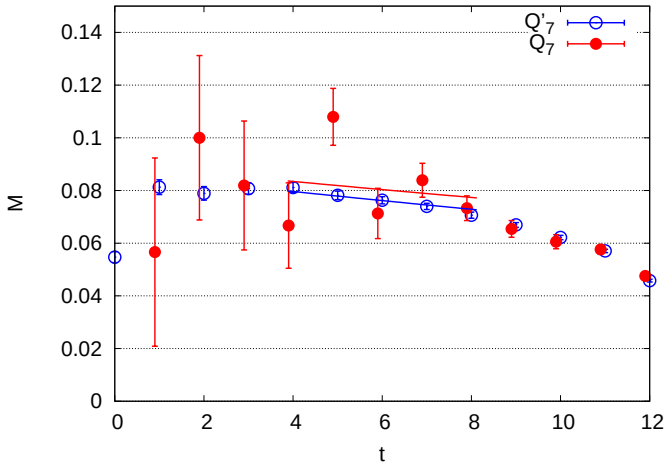

Figure 41: The weak matrix element for $\langle \pi\pi_{I=0}|Q_7|K^0\rangle$ with the same setup as Fig.35.

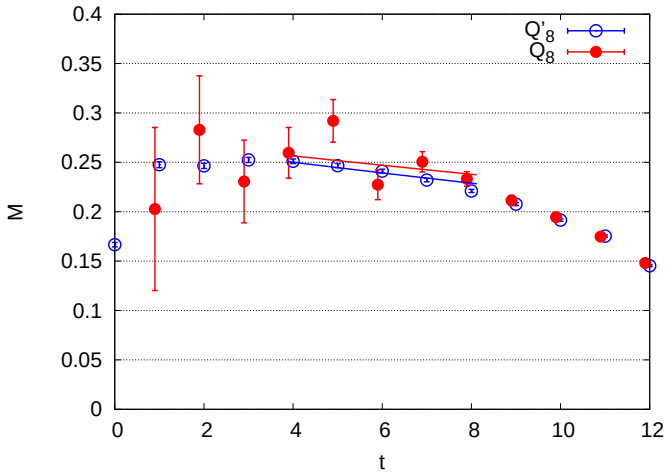

Figure 42: The weak matrix element for $\langle \pi\pi_{I=0}|Q_8|K^0\rangle$ with the same setup as Fig.35.

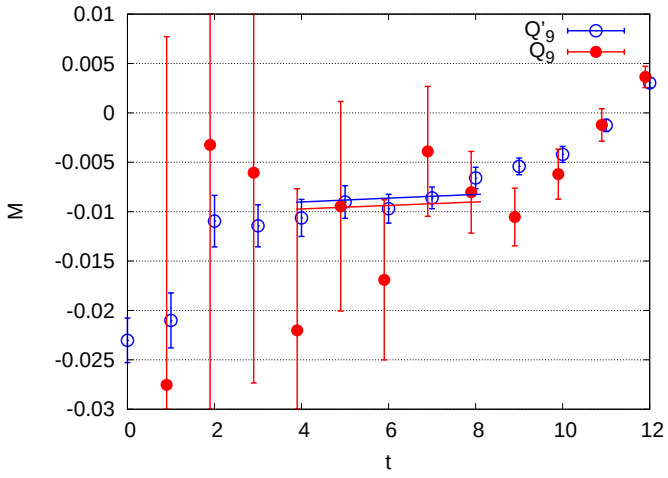

Figure 43: The weak matrix element for $\langle \pi\pi_{I=0}|Q_9|K^0\rangle$ with the same setup as Fig.35.

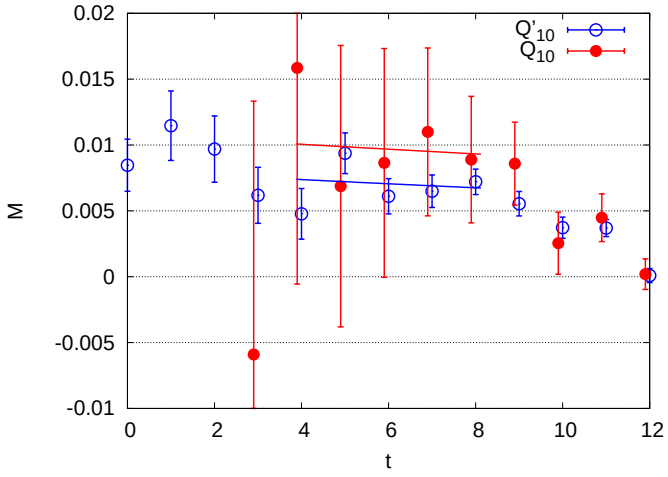

Figure 44: The weak matrix element for $\langle \pi\pi_{I=0}|Q_{10}|K^0\rangle$ with the same setup as Fig.35.

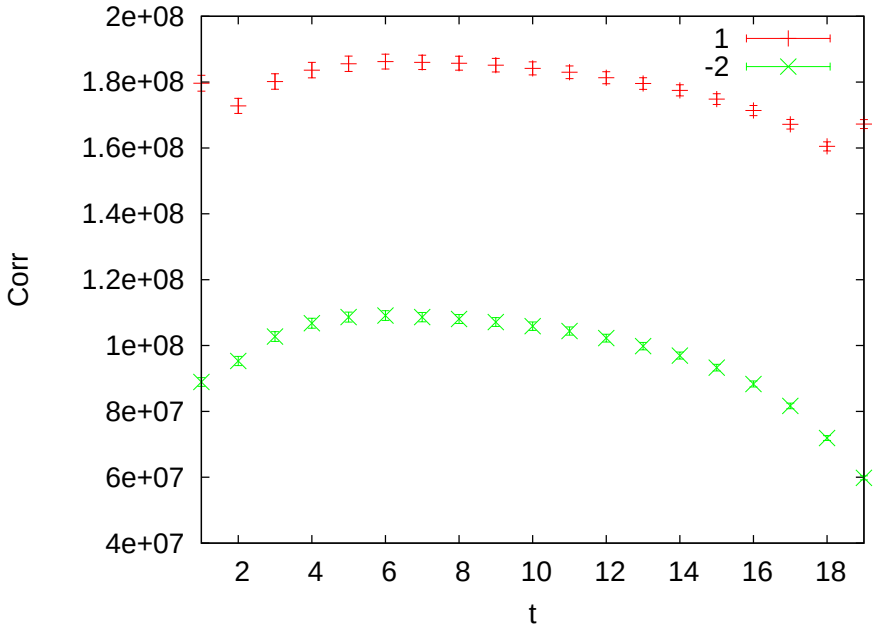

Figure 45: The correlation function for the contraction ① and ②. We take a minus sign on ② so it fits in the graph nicely. This result is from the $24^3 \times 64$ lattice, with $\Delta = 20$ and $\delta = 4$.

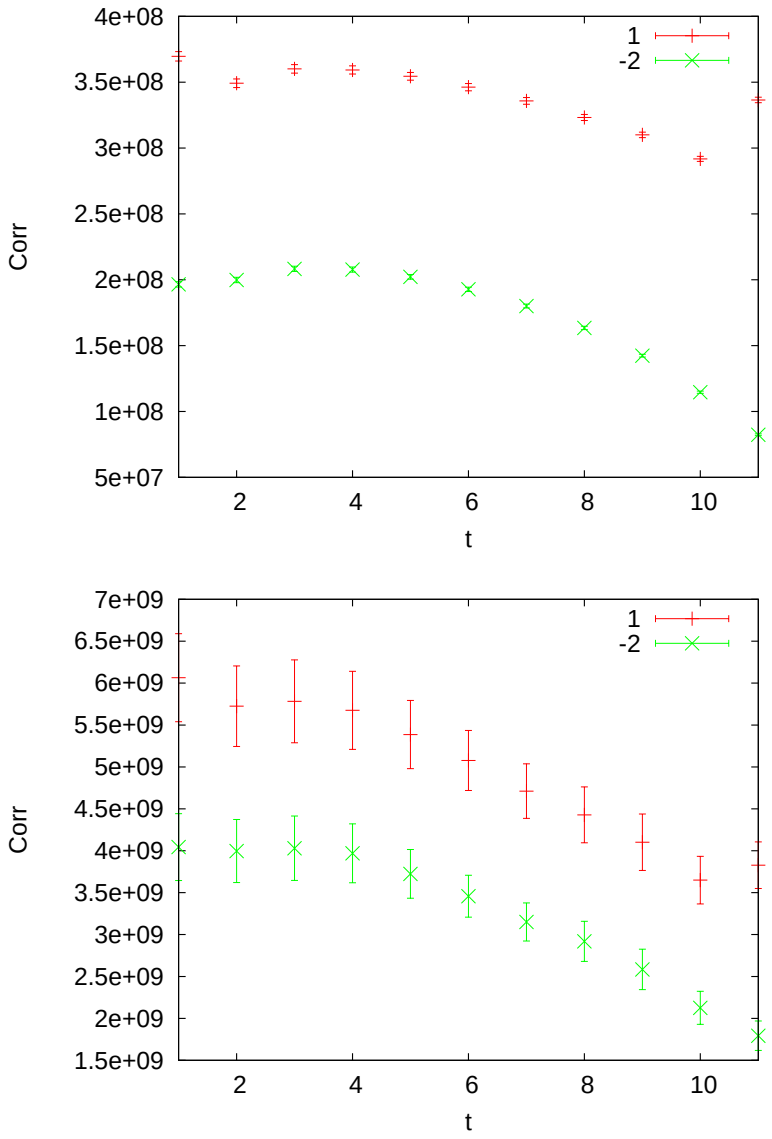

Figure 46: The correlation function for the contraction ① and ②. These results are from the $16^3 \times 32$ lattice with $\Delta = 12$. The top graph shows the result with $m_l = 0.01$ (422 MeV pion mass, 877 MeV kaon mass) from 800 configurations. The bottom graph is the $m_l = 0.001$(247 MeV pion mass, 605 MeV kaon mass), partially quenched result from 50 configurations.